Bi-stable Meta-rod Structures with Designable Shape Transformation for Catheter-based Medical Devices

Atharva Dattatraya Pande

A Thesis in The Department of Mechanical, Industrial and Aerospace Engineering

Presented in Partial Fulfillment

Of

The Requirements

For the Degree of

Master of Applied Science (Mechanical Engineering)

at

Concordia University, Montreal, Quebec, Canada.

August 2025

CONCORDIA UNIVERSITY

SCHOOL OF GRADUATE STUDIES

This is to certify that the thesis prepared

By: **Atharva Dattatraya Pande**

Entitled: **Bi-stable Meta-rod Structures with Designable Shape Transformation for Catheter-based Medical Devices**

and submitted in partial fulfillment of the requirements for the degree of

Master of Applied Science (Mechanical Engineering)

comply with the regulations of the University and meet the accepted standards with respect to originality and quality.

Signed by the final Examining Committee:

Dr. Christopher Yee Wong

_____ Chair

Dr. Tsz Ho Kwok

_____ Examiner

Dr. Hang Xu

_____ Thesis Supervisor

Dr. Lyes Kadem

_____ Thesis Supervisor

Approved by

_____

Dr. Muthukumaran Packirisamy, Chair

Department of Mechanical, Industrial and Aerospace Engineering

August 2025

_____

Dr. Mourad Debbabi, Dean

Gina Cody School of Engineering and Computer Science

Abstract

Bi-stable Meta-rod Structures with Designable Shape Transformation for Catheter-based Medical Devices

Atharva Dattatraya Pande

From large space antennas to medical balloon catheters, we rely on the deployability of rod-shaped structures. Deployable rod structures enable designs that can be compactly assembled into a cylindrical form for transport and then rapidly deployed to achieve the desired shape transformation. For example, in robotic-assisted surgeries, concentric tube continuum robots are designed to provide precise shape transformations, which make it possible to perform intricate maneuvers and complex procedures with greater accuracy. However, the deformations achieved by currently existing compliant mechanisms are highly susceptible to environmental disturbances, particularly in fluid-filled confined spaces. Attaining and maintaining a desired shape requires a triggering mechanism, which takes space, and a constant force, which consumes energy under real-time control. Current rod concepts are less suitable for complex tasks like soft robot motions.

Recent efforts have produced Bi-stable meta-structures with morphing functionalities by mimicking the snap-through mechanism of the Venus Flytrap in nature. This work presents a new class of Bi-stable metastructures named "Meta-rod." Meta-rod structures can transform their shapes from a rod-shaped stable stage to a desired deployed stable stage, realizing linear, bending, twisting, radial, and volumetric changes, or combinations of them. The desired deformation can be programmed into the layout of the Bi-stable structures. Designing different deformation modes, like translation and twisting, involves studying how building block symmetry relates to possible deformations. The Bi-stable concept enables accurate programmed motion and deployment at the second stable stage, freeing space and energy for shape locking.

Via a combination of numerical simulations and physical experiments, this study developed prototypes that demonstrated effective deformation in a range of shape-reconfigurations. The proposed Meta-rod can achieve linear deformation of 60% of its original length, 45° in bending, and 18° of twisting via one unit cell. An umbrella-like areal model and a balloon-like volumetric structure, both stabilized by a locking mechanism, were developed and tested. Their stability and adaptability were validated through static and dynamic loading, including a left ventricle duplicator that mimics physiological conditions.

Acknowledgments

This thesis represents a transformative period in my academic and research journey, centred on the development of Bi-stable metamaterial structures for medical device applications. Over the past several years, I have dedicated myself to exploring advanced mechanical systems and smart materials with the vision of improving minimally invasive healthcare. By integrating principles of compliant mechanisms and biomedical engineering, this work aims to contribute toward safer, more efficient, and energy-independent medical tools. It is my sincere hope that, as innovation continues to reshape medical technologies, this research will play a part, however small, in enabling more precise interventions and enhancing the quality of care for patients around the world.

I sincerely thank my supervisor, Dr. Hang Xu, for his invaluable guidance, steadfast support, and insightful feedback throughout my research. His expertise and encouragement have significantly shaped the direction and depth of my work. Thank you for giving me the freedom to manage my own research workload and to tackle challenges independently, which has helped me become a better researcher. Your support in enhancing my writing skills has made me a more effective technical writer, a skill I would not have gained elsewhere. I also appreciate the opportunity to supervise multiple undergraduate students and contribute to their projects. Thank you for trusting me and allowing me to establish our lab, which I will miss the most since I have spent three quarters of my time here.

I want to thank my Co-supervisor, Dr. Lyes Kadem, for giving me the opportunity to start my research career. Your guidance and encouragement through this journey have been very helpful in completely all the tasks.

A special thanks to my seniors, Kianoosh and Alexandra, for being there as a support pillar on this wonderful journey. I'll miss our coffee chit-chat after the Friday meetings. I hope, I have been helpful to both of you in your PhD journey.

One more special thanks to my master's journey partner in crime, Justin. We both started this together and completed the program together. Thank you for teaching me the simulation programming which help me develop the complete structure for future students. And also, in the simple stuff which I was lazy to learn on my own.

I want to thank all my TAs professor, who gave me the opportunity to teach and learn during the sessions.

I also want to thank all the undergraduate students who have been involved in this research group under Dr. Xu. It was fun and a big learning experience for me in mentoring you all.

I want to thank all my office colleagues, especially Lorenz and Ali, you both are like big brothers to me. Thank you for guiding me and answering all the stupid question I have asked till now.

A special thank you note to my friend, colleague and brother, Himanshu Sharma, for being the person whom I can rant to. Also, to Mehul, Nitin, Sristi and Harshita for supporting me and being there during this journey.

Finally, to my Mom and Dad, for allowing me to switch from a course-based to a research-based master's program, even though I had completed 60% of it. Thank you, Mom, for listening and tolerating me during those night calls and understanding when I didn't pick up because I was tired. Thank you, Dad, for being there and guiding me during the most important decisions. Thank you to my brothers, Parag, Parimal, and Piyush, for hosting me at your house during the winter breaks. Now, your house is my second home on this continent.

Table of Contents

List of Figures

List of Tables

Nomenclature

Acronyms

Atrial Fibrillation	AFib
Bi-stable building block	BBB
Left atrium	LA
Minimally invasive surgery	MIS
Linear deformation	LD
Bending deformation	BD
Finite element analysis	FEA
Right superior pulmonary vein	RSPV
Right inferior pulmonary vein	RIPV
Left superior pulmonary vein	LSPV
Left inferior pulmonary vein	LIPV
Sequential Contact Mapping	SCM
Earliest sites of activity	ESA
Focal Impulse and Rotor Mapping	FIRM
Stochastic Trajectory Analysis of Ranked Signals	STAR
Transcatheter aortic valve replacement	TAVR
Additive Manufacturing	AM

Symbols

Representation of Linear model	${}^{L_1\text{-Left-side}}_{L_2\text{-Left-side}}L^{L_1\text{-Right-side}}_{L_2\text{-Right-side}}$
Representation of Bending model	${}^{L_1\text{-Left-side}}_{L_2\text{-Left-side}}B^{L_1\text{-Right-side}}_{L_2\text{-Right-side}}$
Representation of Twisting model	${}^{L_1\text{-Left-side}}_{L_2\text{-Left-side}}T^{L_1\text{-Right-side}}_{L_2\text{-Right-side}}$
Bending angle	θ_B
Twisting angle	θ_T

Parameters

Length of BBB	L (mm)
Thickness of BBB	T (mm)
Width of BBB	W (mm)
Location of Notch -1	L_1 (mm)
Location of Notch -2	L_2 (mm)
Thickness of notch	t, t_1, t_2 (mm)
Length of notch	l, a, b (mm)

Chapter 1: Introduction

1.1 Background

From large space antennas to medical balloon catheters, we rely on reconfiguring rod-shaped structures. Shape-reconfigurable rod structures enable designs that can be compactly assembled into a cylindrical form for convenient transport and then morphed or deployed to achieve the desired deformations. For example, medical interventions require rod-shaped balloon catheters at a diameter scale of several millimeters that can be deployed in treatment with desired expansion [1]. In robotic-assisted surgeries, concentric tube continuum robots are designed to provide precise shapeshifting, which makes it possible to perform intricate maneuvers and complex procedures [2], [3].

Engineers have developed rod structures that can yield reconfigurations of broad geometric diversity. For example, under 1) anatomical constraints and 2) tangled cardiovascular networks, guidewires and catheters can realize a combination of complex shapeshifting to overcome movements along tortuous paths. Taking atrial fibrillation (AFib) treatment as an example of deployment, the ablation catheters with guidewires linearly dislocate (move axially), bend, and twist to reach targeted locations [4], [5]. In contrast, mapping catheters expands radially or volumetrically from a rod assembly to planar or spherical structures. However, producing shape-reconfigurable rod structures with various deformations is challenging due to the limitations in build volume and available actuating power sources [6].

Shape-reconfigurations can be triggered through diverse mechanisms, such as pull-wire systems [6], screw mechanisms, sheath retraction, thermal actuators, and snap-fit designs [6], stimulated via environmental changes in pneumatic, hydraulic, thermal, or mechanical fields [7]. Mechanisms that facilitate these environmental changes can be used to sustain the deformed shapes. However, these mechanisms occupy valuable space inside the rod structures, preventing minimization that is crucial for engineering applications while also requiring constant applied external power sources that necessitate continuous high-fidelity control from operators [6], [7], [8]. For example, cable-driven shape-shifting triggering systems applied to achieve controlled navigation and deployment in catheters are space-consuming. Pull-wire mechanisms, as seen in Agilis™ and Sensei® X systems,

provide intuitive steering at the cost of occupying internal lumen space and require continuous mechanical input from operators [9]. Shape memory alloy (SMA)-based devices like NeoGuide servo system offer compact actuation but suffer from delayed thermal response and fatigue under cyclic loading [10]. Magnetic systems, such as the Stereotaxis Niobe®, allow remote guidance but require large external infrastructure and produce limited force output [11]. Pneumatic and hydraulic systems, often used in soft robotic prototypes, enable distributed motion but lack precision and stability under dynamic physiological conditions [12].

The previously reported catheter deformations are maintained by a space- and energy-consuming feedback system, which needs continuous and precise monitoring and adjustment. Maintaining the balloon catheter's expansion requires an external hydraulic system with sustained pressure under constant monitoring. Similarly, in pull-wire and cable-driven catheters (e.g., Agilis NxT [9] and TactiCath [9]), deformation is maintained manually by the operator through proximal handle inputs that translate continuously steered tension to the distal tip. The feedback systems are susceptible to non-linear disturbances, such as friction, cable slack, and anatomical resistance. The maintenance of high-fidelity deformation thus depends on the operator's expertise in tactile feedback. In robotically assisted systems like Hansen Medical's Sensei® X, catheter deformation is guided through programmable robotic segments, enabling more precise and repeatable tip manipulation, however, with penalization of its high cost spent on the complexity and space [8], [9]. Magnetically actuated catheters (e.g., Niobe®) shift control from internal mechanics to external field navigation; while highly accurate in controlled environments, the deformations depend on precise field calibration, stable anatomical positioning, and patient immobility for consistent performance [9], [13]. Actuators based on SMAs, pneumatic, or hydraulic systems rely on control of external energy inputs, causing temperature, hydraulic pressure, or fluidic pressure changes, to induce motion. However, their response is often large-nonlinear, delayed in terms of time, and influenced by environmental conditions such as temperature and fluid flow [14], [15], [16]. These systems are thus susceptible to drift, hysteresis, or inconsistent deformation during navigation or deployment.

Handling large deformations, such as multi-directional bending, twisting, or radial expansion, presents significant challenges. These complex shape transformations are crucial in procedures like atrial mapping and targeted ablation, where consistent contact and comprehensive spatial coverage are essential. However, current actuation systems struggle to reliably control such large deformations due to nonlinear mechanical behaviors, input backlash, material hysteresis, and

sensitivity to anatomical resistance. As the extent of deformation increases, small errors are amplified, leading to deviations from the desired shape, tip instability, and diminished targeting accuracy. This lack of deformation precision compromises both the safety and efficacy of the device, particularly within dynamic physiological environments.

A promising approach to achieving programmable deformation in deployable rod-shaped structures draws inspiration from nature, where architectural features enable remarkable shape transformations. For example, chiral deformation in sunflower stems and the auxetic behavior of cork are attributed to their internal geometries [17], [18]. Mimicking such biological systems, researchers have developed metamaterials and metastructures whose mechanical behavior arises from design rather than material composition [19], [20]. These engineered systems can undergo large nonlinear deformations in bending, twisting, and radial expansion, while maintaining control and structural integrity [21], [22] and making them suitable for compact environments like the human anatomy. Moreover, by incorporating bistability inspired by mechanisms such as the Venus Flytrap, recent studies have shown how structural instabilities can be used to lock deformations in place without continuous energy input, offering precise and reversible shape change [23], [24], [25].

1.2 Problem Statement

Existing deployable rod-shaped structures are limited in their ability to achieve diverse and programmable deformations, such as linear displacement, bending, twisting, and area and volume expansions via a single unified compact structural concept. This is primarily due to their dependence on complex external actuation systems and the lack of a unified singular geometrical design framework. Existing systems rely on continuous power and active control, leading to high energy consumption, loss of internal lumen space, and imprecise deformation, especially during large shape changes, and ultimately limiting their use in targeted therapy and minimally invasive procedures. As a result, there is no current solution that provides multifunctional deformation, self-locking stability, and energy-free maintenance in a miniaturized cylindrical device. This research addresses that gap by introducing the Meta-rod: a geometrically programmed metastructure capable of large, reversible deformations governed purely by internal architectural design. The developed Meta-rod will be integrated into medical robot elements for Atrial Fibrillation (AFib) treatments.

1.3 Thesis Layout

The research focuses on medical applications in the field of catheters and guidewires used for multiple interventional procedures. The introduction section covers general concepts of rod-shaped devices and their reconfigurable shapeshifting mechanisms, followed by applications in various fields, including aerospace, satellites, and medical devices. Chapter 2 presents a literature review on concepts and state-of-the-art medical devices, ranging from general deployable structures to specific medical problems addressed in this study. Chapter 3 provides the design routes and methodologies, from numerical analysis to prototyping and testing setups. Chapter 4 covers the simulation results, prototyping and required testing to confirm the Bi-stable concept in a metal wire and its proposed validation analysis in left atrium duplicator set-up. Chapter 5 concludes the outcomes and provides further structured data that can be utilized to formulate future solutions to new problems using the proposed concept in this research.

Chapter 2: Literature Review

Literature covered in this chapter consists of multiple key topics, starting from deformation classifications and application of rod shape to complex structure deformation in aerospace and medical fields. General examples of deformation in the medical field include perform intricate surgical operations, for example, 'Atrial Fibrillation (AFib)'. Treatment option requiring mapping and ablation of irregular signals via a mapping catheter and an ablation catheter is discussed, along with the different types of mapping catheters and their limitations. This chapter also covers the literature on metamaterials and Bi-stable mechanical metamaterials, as well as background related to the proposed solution.

2.1 Deformation

2.1.1 Definition of Deformation

Deformation, as referred to in engineering sectors, describes how a material or structure changes in size, shape, or volume in response to external forces such as mechanical loads, thermal expansion, or environmental factors [26], [27]. Tension, compression, bending, torsion, or shear forces are responsible for both elastic deformation (Fig. 2-1), in which the material returns to its original shape when the load is removed. While plastic deformation is a non-reversible change of shape in response to applied forces, in which the change is permanent [28], [29].

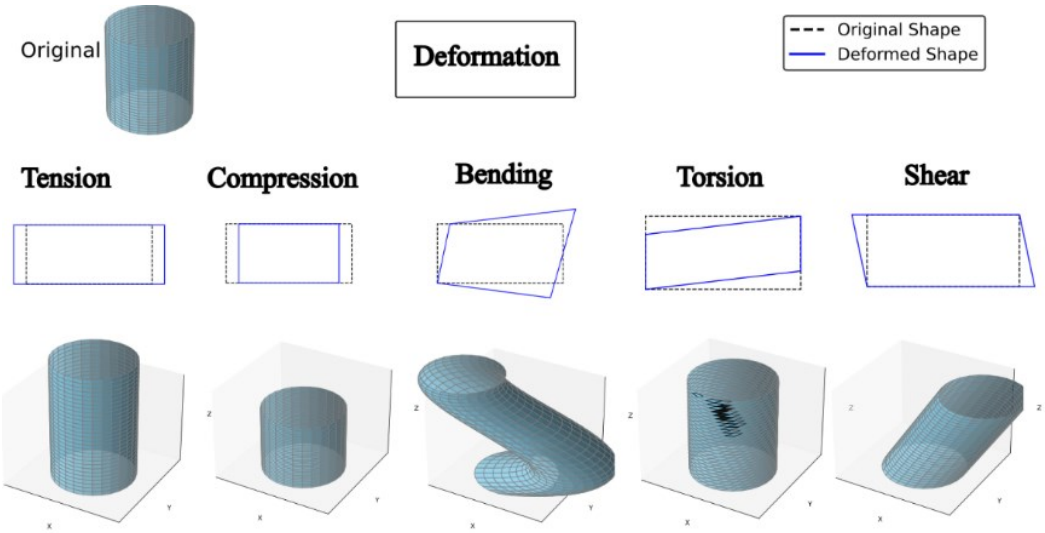

Fig. 2-1 Types of deformation via axial load

The application of deformations directly affects design, durability, performance, and deformation analysis, which is essential in many engineering domains, including mechanical, biomedical, aerospace, and structural engineering [30], [31], [32], [33]. Engineers have improved materials and structures to increase efficiency, dependability, and safety in practical applications by comprehending deformation behaviour according to the required application.

2.1.2 Deformation in Aerospace: Cylindrical Rod to Configured Shape

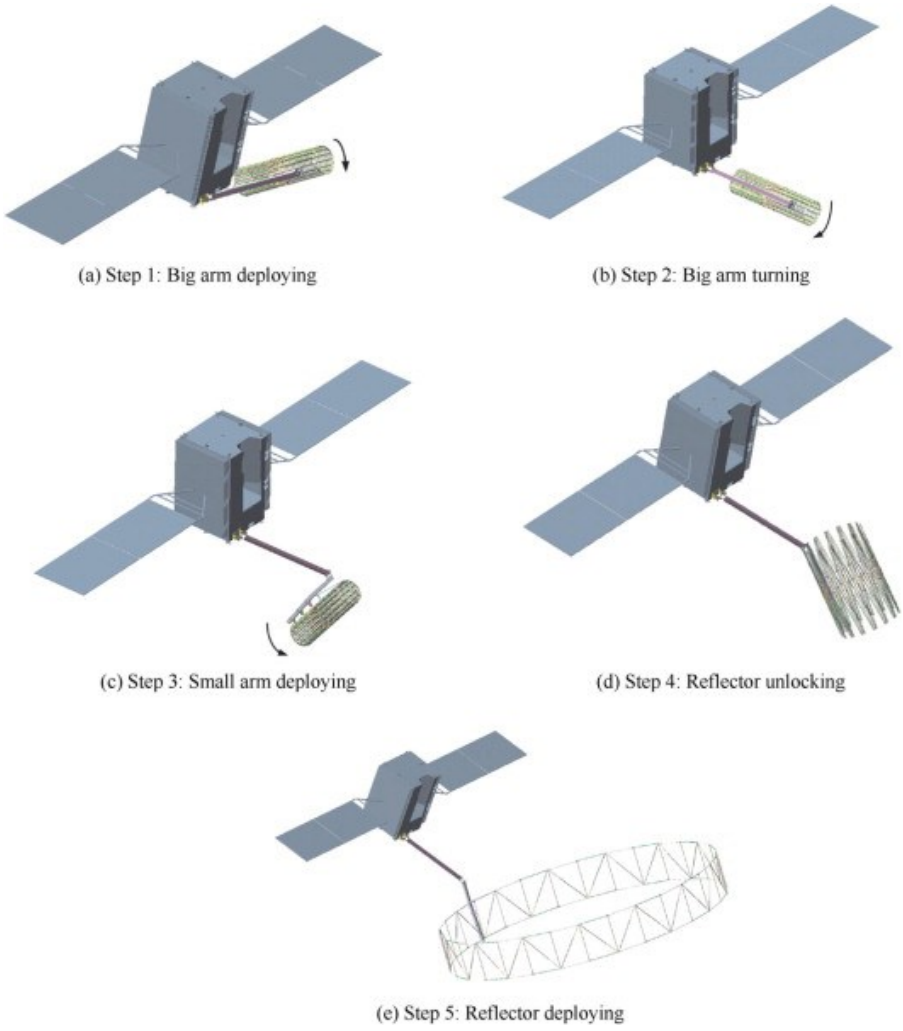

Fig. 2-2 Deployment of a satellite boom into a ring structure [34]

In aerospace applications, deformation frequently entails dimensional changes, particularly in two-dimensional (2D) connections like actuators and mechanical hinges that shorten or lengthen structural elements [35]. However, in order to maximize utility, it is common practice to change the length or shape of a structural element, especially in aircraft landing gear struts, deployable

aerospace structures from a cylindrical rod to a pre-configured shape and size [35], [36], [37], [38]. Deployable satellite booms are a prime example (Fig. 2-2), as they are designed with thin-walled cylindrical rods that fold into compact shapes for easy storage and transportation during launch [39], [40]. Once in orbit, they enlarge into their final deployed structure, enabling applications such as structural reinforcement, solar panel deployment, or antenna extension [41], [42]. This controlled deformation minimizes mass and maximizes utility, allowing for lightweight, space-efficient, and flexible structures [43], [44]. However, these systems have technical drawbacks, including actuation mechanics, maintaining structural stability, minimizing material fatigue, and ensuring accurate deployment [45], [46].

2.1.3 Deformation in Medical Devices: Cylindrical Rod to Specific Shape

In medical devices, shape transformation is achieved by applying external force on cylindrical rods or tube-like structures, resulting in controlled deformation [47]. To carry out their intended biological tasks, devices like guidewires, stents, and catheters depend on this deformation (Fig. 2-3) and deployment principles [48], [49].

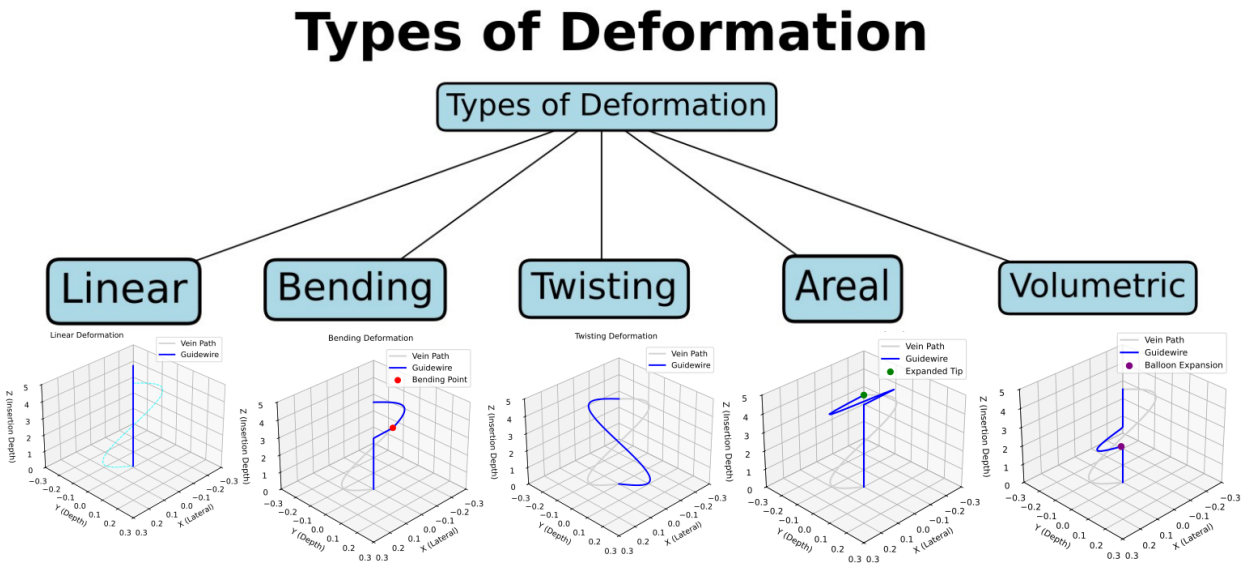

Fig. 2-3 Deformation used by medical devices to navigate through complex anatomy

A balloon catheter, which is assembled as a thin, tube-like device with a diameter in the millimeter scale for simple insertion into the human body, illustrates out-of-plane deformation [2], [50]. Therapeutic operations like angioplasty are made possible by the tip's expansion into a

balloon-like structure of size 18 to 25 mm when activated by external actuations [51]. The pre-configured deformation of the wires and support structures inside the catheter causes trans-dimensional shifts, which permit regulated expansion. However, constant external energy input is required to maintain the distorted shape, which makes the catheter's design complex [52]. This restriction limits the options for controlling and maintaining deformation in dynamic physiological conditions, which has an impact on the effectiveness and versatility of these devices.

2.1.4 Deformation Classification and Applications in Medical Devices

In general, there are five forms of deformation in medical devices: volumetric, areal, twisting, bending, and axial (linear). Whereas areal and volumetric deformations (like those found in deployable satellite booms and balloon catheters) are the outcome of a rational combination of these fundamental deformations to achieve a desired shape configuration (Fig. 2-4). For instance, warping arises from stresses induced by temperature, leading to bending deformation (BD) as thermal expansion happens in a flat plate [53], [54].

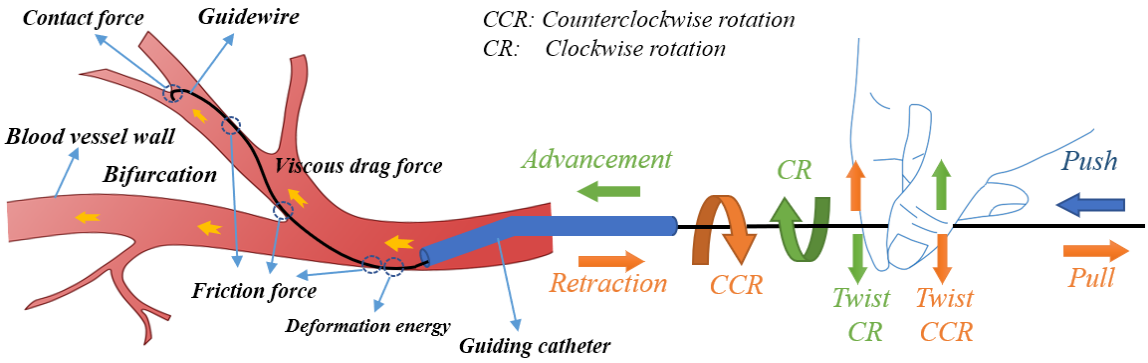

Fig. 2-4 Catheter undergoing various deformations to navigate through a vein [55]

Catheters experience all five forms of deformation [7] to navigate in human anatomy, where anatomical features and organ locations differ from patient to patient. A catheter requires bend (flex around stiff vein anatomy), twist (to negotiate complex paths), and travel (linear deformation (LD)) to reach the intended spot. Furthermore, balloon catheters, which start as narrow cylindrical tubes, can expand volumetrically, allowing them to enlarge within arteries during angioplasty procedures [2], [56], similar to a deployable satellite boom in aerospace applications exhibit regulated areal expansion as they evolve from a compact folded configuration to a fully stretched state [57].

2.2 Deformation Applied in Biomedical Devices and Minimally Invasive Surgery

2.2.1 Applications of Deformable Devices

Minimally invasive techniques have been transformed by the creation of robotic systems and surgical equipment, which allow for precise and controlled interventions [58]. Vascular navigation, diagnostics, interventional treatments, medication delivery, embolization, aneurysm repair, electrophysiological mapping, and ablation are all made possible by catheters and guidewires, which are crucial in this discipline [59], [60]. These gadgets require highly precise deformation to navigate well in intricate biological structures (Fig. 2-5).

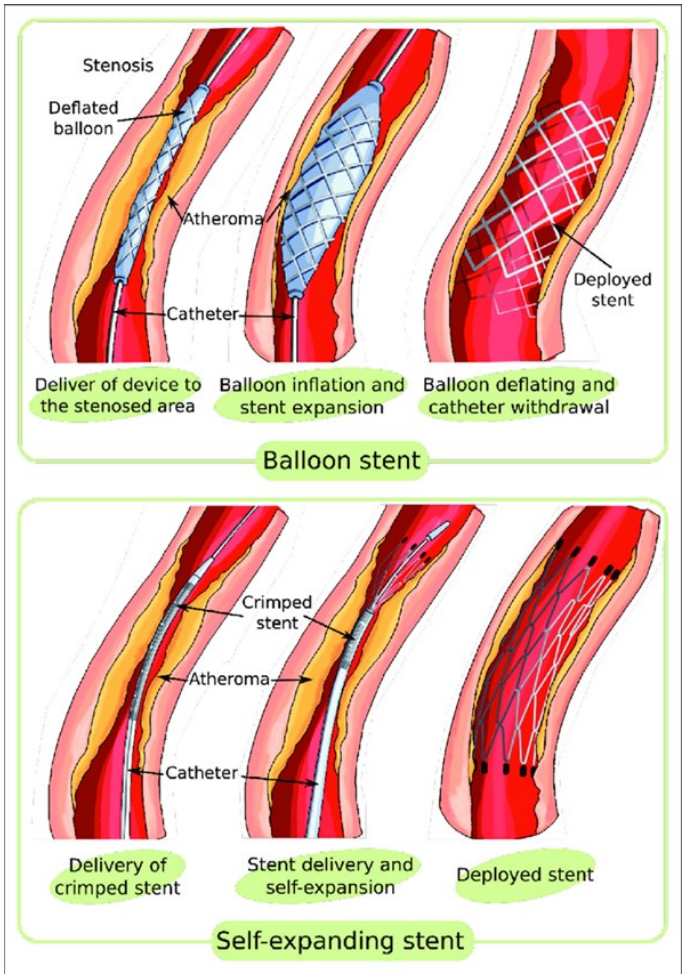

Fig. 2-5 Self-expanding stents and balloon inflation stents [61]

1. **Vascular Navigation and Access:** Guidewires require controlled bending and twisting to traverse intricate vascular pathways without damaging vessel walls. Their deformation properties influence flexibility, torque response, and steerability, which are crucial for procedures like neurovascular interventions and coronary angiography [60], [62].
2. **Interventional and Therapeutic Techniques:** Balloon catheters undergo volumetric deformation to restore blood flow in angioplasty and stenting. Understanding deformation behaviour ensures optimal balloon compliance, expansion, and recoil, minimizing tissue damage and restenosis. Similarly, electrophysiology catheters require precise bending and twisting for accurate arrhythmia treatment [59], [60], [62].
3. **Drug and Therapeutic Agent Delivery:** Drug-eluting catheters experience areal deformation upon interacting with vascular walls (Fig. 2-6), requiring careful control of strain, friction, and expansion for effective drug release and tissue protection [63].
4. **Structural Heart Disease Treatment:** Transcatheter aortic valve replacement (TAVR) catheters undergo bending and areal deformation while navigating the aortic arch, necessitating optimized flexibility for precise deployment without compromising push ability [64].
5. **Electrophysiology and Mapping:** Three-dimensional (3D) mapping catheters undergo complex bending and twisting to ensure accurate contact force and stability during arrhythmia treatment [65], [66], [67].

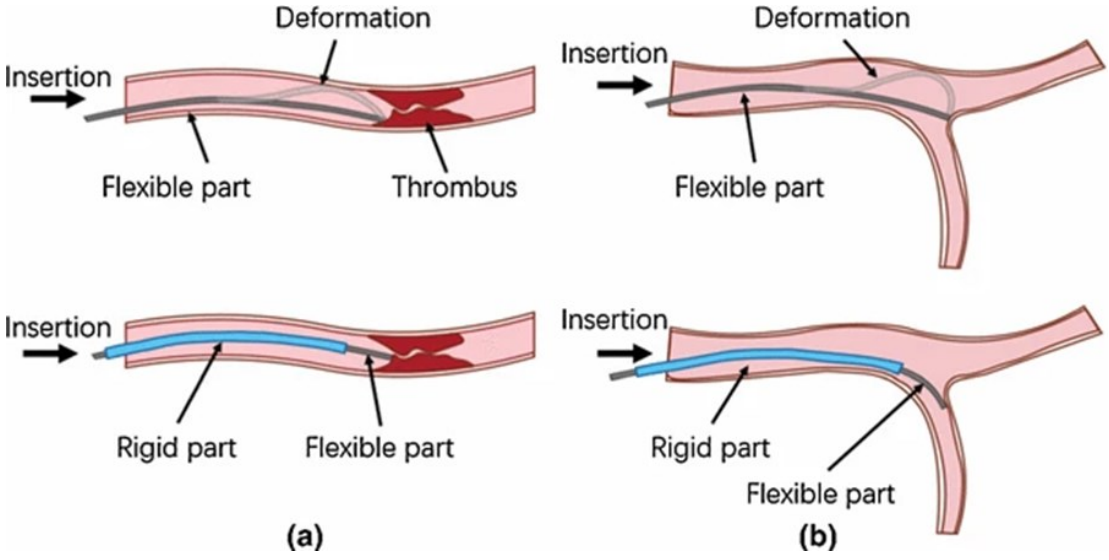

Fig. 2-6 Guidewire movement through a clogged vein [68]

To ensure safety, precision, and lifespan during medical procedures, catheters and guidewires must facilitate improved movement through precise deformation in clinical settings [11]. To avoid procedural inefficiencies, essential features, including form retention, material memory, fatigue resistance, and flexibility, are optimized. However, adjusting to complex cardiac and vascular architecture is a major challenge for current-generation devices [69]. The rigid or semi-flexible materials of the current device can kink, buckle, or lose their form memory, and thus complicate navigation, lengthen surgical times, and increase the risk of vascular damage [71], [72]. For example, guidewires made of cables have limited bending properties and insufficient torque response, which results in inaccurate positioning and lowers the effectiveness of operations, including angioplasty, thrombectomy, and cardiac ablation. Stent-delivery devices and balloon catheters made of rigid or semi-flexible materials frequently show uneven expansion and recoil, raising the risk of vascular damage or restenosis [2], [73], which requires better volumetric deformation control. Device stability is limited by the inability to hold a distorted shape without external support in surgical operations, such as TAVR and neurovascular surgeries [75], where precise positioning is crucial. AFib is one ailment that requires accurate mapping and ablation; in this case, sophisticated catheter designs can improve treatment reliability and procedure efficiency [4], [76].

2.2.2 Atrial Fibrillation

The most prevalent cardiac arrhythmia, atrial fibrillation (AFib), is typified by rapid and irregular electrical activity in the atria. AFib is a common heart condition in which, the heart beats in an irregular manner or arrhythmia, generating chaotic and out of sync electrical signals [75]. It raises the risk of heart failure, stroke, and other cardiac problems. It is projected that by 2050, more than 7-10 million [76] people in US and around 12-15 million in Europe will be affected by AFib [4], [5], [74]. AFib causes the upper and lower chambers to beat in an out-of-sync manner, which creates poor blood flow, increasing the risk of blood clots, stroke, heart failure, and other heart-related complications. The tissues involved create a complicated pattern of irregular arrhythmia, which features erratic electrical signal waves (Fig. 2-7). To fix this irregular heartbeat, the damaged tissue or region needs to be located and destroyed [77], [78]. AFib treatment uses a specialized mapping catheter and involves applying energy to carry out the ablation at the identified location

[79]. Once this precise site is located, an ablation treatment can be performed, in which a targeted therapeutic intervention is designed to destroy the problematic tissue.

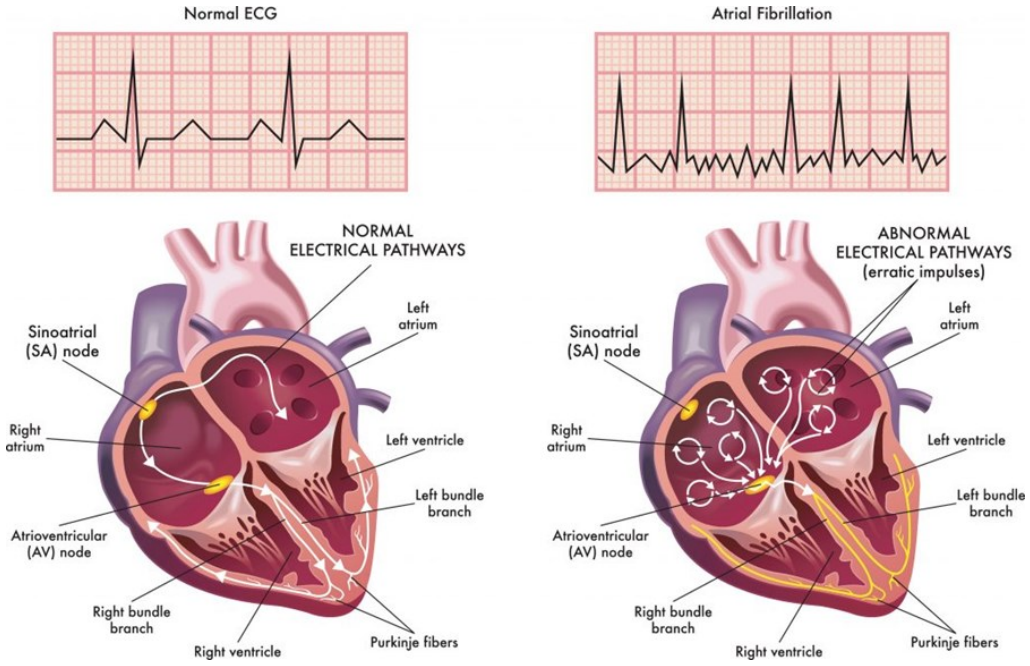

Fig. 2-7 Heart and ECG comparison of a normal and AFib-affected human [80]

2.2.3 Treatment Options

Treatment varies based on AFib severity and patient age. **Medication** (rate control, blood pressure regulation, and anticoagulants) can manage symptoms but complicates any other surgical interventions due to an increased bleeding risk. **Cardiac intervention** offers a direct approach using **mapping and ablation catheters.** [4], [78], [81], [82]. Ablation procedure has multiple good options:

Table 2-1: Classification of AFib ablation types [5]

Ablation Types	Best for
Radiofrequency (RF) Ablation	Paroxysmal & persistent AFib
Cryoablation (Cryoballoon)	Pulmonary vein isolation (PVI)
Pulsed Field Ablation (PFA)	Emerging technology, trials ongoing
Surgical Maze Procedure	Long-standing persistent AFib
Convergent Ablation (Hybrid)	Complex, persistent AFib

2.2.4 Mapping Techniques

Mapping methods are categorized as contact and non-contact techniques. Non-contact methods such as Charge/Dipole Density Mapping and Body Surface ECGI have an accuracy of less than 50% in detecting the arrhythmia source. Contact mapping involves minimally invasive surgery (MIS), where a catheter is inserted into the left atrium (LA)—a primary site for AFib detection. [83]. Two major contact mapping methods are:

1. **Panoramic Contact Mapping**: Provides a global view of atrial activity using techniques like Focal Impulse and Rotor Mapping (FIRM) and Electrographic Flow Mapping (Ablacon), though clinical results are mixed [67].
2. **Sequential Contact Mapping (SCM)**: Uses high-density electrode arrays to precisely identify re-entrant circuits and rotational activation, improving ablation outcomes. Examples include CARTOFINDER (Biosense Webster) and Spatiotemporal Dispersion Mapping (Volta Medical) [83], [84].

2.2.5 Sequential Contact Mapping

SCM uses multi-electrode catheters to collect electrogram data from different atrial regions, constructing a high-resolution 3D map for targeted ablation. Basket-shaped catheters, such as CARTOFINDER (Biosense Webster), enhance tissue contact by embedding electrodes on their surface. Depending on the electrical signal recognition methods following are various option available in the market [79], [83], [84], [85], [86], [87], [88], [89]:

- CARTOFINDER (Biosense Webster) – Utilizes PENTARAY catheters for high-density activation mapping.
- Spatiotemporal Dispersion Mapping – Identifies stable electrogram patterns without requiring activation annotation.
- Stochastic Trajectory Analysis of Ranked Signals (STAR) – Ranks activation sites based on wavefront trajectories to determine the earliest sites of activity (ESA).
- Real-time Electrogram Analysis for Drivers of AF (RADAR) – Computes 3D conduction vector maps using conduction velocities across electrodes.
- CardioNXT – A commercial system currently under evaluation for AFib mapping.

As these are mechanical human-made devices, there are limitations and drawbacks of these instruments [66], [83], [90], [91], [92], [93], [94]:

1. **Inconsistent Mapping Accuracy**: Low bipolar voltage zones have not always been reliably associated with techniques such as CARTOFINDER. The distinction between focal and rotating AFib drivers is not well-represented by STAR mapping.
2. **Variability in Electrode-Tissue Contact**: The basket-shaped catheters used in the majority of sequential mapping procedures deploy numerous electrodes to record electrical signals. Data collection is uneven because different patients have different percentages of electrodes in direct touch with atrial tissue. This variability often necessitates multiple mapping attempts to improve accuracy.
3. **Complexity in Real-Time Operation:** Basket catheters make the technician's job more difficult because they need external force mechanisms to maintain deformation. Accurate positioning is crucial for Real-time Electrogram Analysis (RADAR) to compute 3D conduction vector maps, but precise electrode location and distance estimation remain challenges.

2.2.6 Limitations and Future Direction for Improvement

The deployment and steering of catheters within the left atrium (LA) require a combination of bending (BD) and twisting deformations (TD), typically controlled by a guidewire-catheter system [95]. This process demands simultaneous operation of two systems, increasing procedural complexity and requiring significant expertise [60]. Once the catheter enters the LA, it deploys into a basket-shape to facilitate mapping. However, maintaining this deformed configuration relies on constant external force, which increases device weight and steering complexities [9], [12]. Additionally, blood flow obstruction and a limited number of electrode-tissue contact sensors reduce mapping efficiency [91], [94]. The fixed basket size restricts compatibility (Fig. 2-8) to patients with hearts of different sizes, making the procedure less adaptable. Furthermore, the central portion of the catheter is occupied by a mechanical actuator, which limits any further integration of an ablation catheter device.

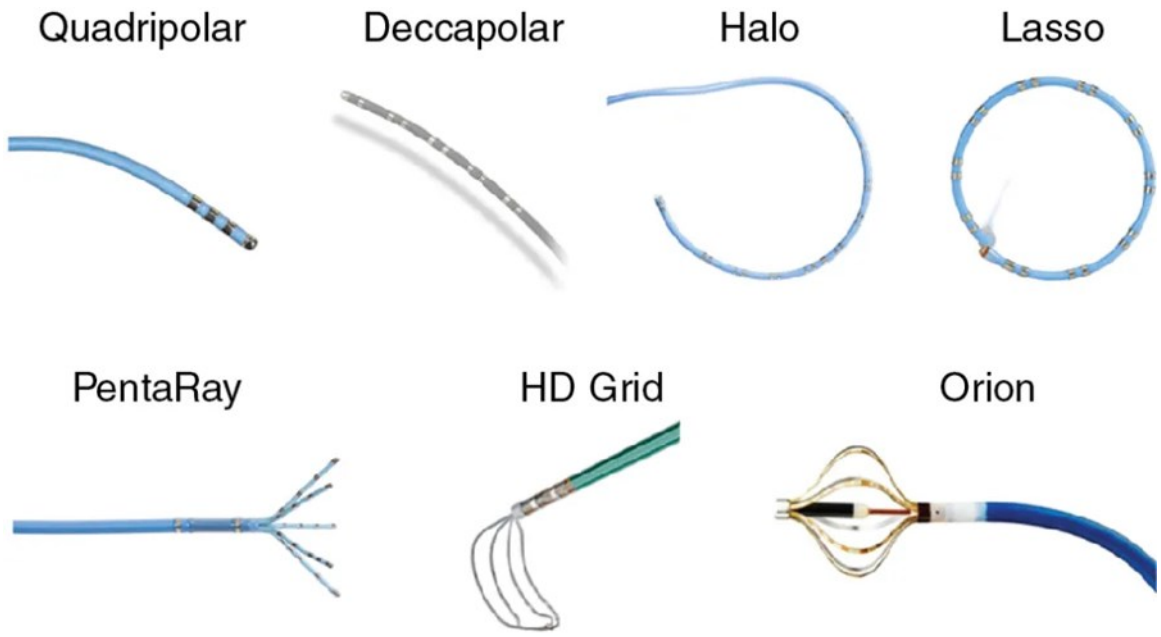

Fig. 2-8 Mapping catheter designs in the industry [96]

To overcome the aforementioned challenges, integrating compliant mechanisms into catheter designs offers promising solutions [97]. Shape Memory Alloy (SMAs) compliant mechanisms can achieve programmable deformations, which are triggered by temperature changes [75]. In contrast, body temperature remains constant, thereby limiting the effectiveness of SMAs. An alternative approach is the use of Bi-stable-concept-based metamaterials or metastructures, which can transition between two stable states without requiring continuous external energy input [24], [98]. By utilizing a Bi-stable metastructure, a catheter could maintain its deformed shape independently, eliminating the need for extra mechanical locking systems and reducing procedural complexity. The freed space would allow for the integration of both ablation and mapping functions into a single catheter, eliminating the need for dual catheter insertion and significantly improving efficiency, adaptability, and patient recovery time. Further research into metamaterials and their applications in compliant medical device design is necessary to assess their feasibility in next-generation catheters that are lighter, more flexible, and capable of multi-functional operation.

2.3 Metamaterials and Metastructures

2.3.1 Definition of Metamaterials

Metamaterials are systematically engineered materials designed to exhibit properties that are not commonly found in natural materials [99]. The physical properties of these materials have the potential to be tailored distinctly when compared to those of the base material. The prefix of the word “metamaterials” originated from a Greek prefix “meta” meaning “beyond”, representing their ability to obtain performance beyond their compositions and even surpass the conventional material limitations [19]. The rational structural design of unit cells, including the topology, distribution of different compositions, and assembly orientation of these unit cells, plays the leading role in deriving the properties, rather than depending mainly upon the chemical compositions of base materials [21]. The structural design consists of periodically or non-periodically tessellated unit cells, which enables the tailoring of various unique behaviors such as electromagnetic, acoustic, and mechanical properties[21], [100], [101].

2.3.2 Types of Metamaterials and their Advantages

Versatile metamaterials have been widely utilized in various physical sectors, including acoustic, electromagnetic, and mechanical applications. In acoustic applications, metamaterials are applied for protective screens, vibration damping, and anti-sonar applications. These acoustic metamaterials are curated by carefully controlling the distribution of bulk modulus, density, and chirality in a unit cell by using two or more base materials to interact with sound in specific ways [99]. On the other hand, electromagnetic metamaterials tailor their performance mainly by structural arrangement design, although the sensing of humidity, pressure, temperature, and biological molecules present in the environment is still [102], [103]. Mechanical metamaterials, which are engineered with unique unit cell structural orientation/architectures, to achieve extraordinary mechanical properties such as negative Poisson’s ratio, negative elastic modulus, and zero shear modulus [103]. The advantages of the mechanical metamaterials here introduced can be capitalized in several primary applications, where the material behaviour can adapt to changes in the environment, such as varying load conditions. Mechanical metamaterials can enhance the strength while maintaining the lightweight structural properties, making their

applications in the field of aerospace, defence, and medical devices of high values [21], [100], [101], [104].

2.3.3 Mechanical Metamaterials

Mechanical metamaterials are artificially designed materials to exhibit outstanding mechanical properties that are beyond those of the base material or even unprecedented in conventional materials. Their behavior is primarily programmed by their geometric arrangement rather than their compositions, unlike natural materials [19]. Borrowing concepts from crystal lattices, scientists periodically tessellate a single unit cell at the macroscale to construct “lattice materials”. Metamaterials with periodical tessellation are considered a kind of lattice material. Hierarchical metamaterials have unit cells with structural elements that themselves are constructed by structures at a lower length scale, such as the Eiffel Tower, in which the beam elements are constructed via truss structures [99]. These metamaterials with structural hierarchy are lightweight with high specific stiffness and strength. Designing metamaterials with extreme mechanical responses, such as negative Poisson's ratio, controllable stiffness, and programmable deformation, is now possible thanks to developments in computer modelling and multi-material additive manufacturing (AM) [105]. Metastructures refer to the smart structures that are not constructed by periodic unit cells in a lower length scale but still achieve designable functions via multi-physics interactions between elements and thus generate accelerating scientific and technological interest in recent years [99]. This differentiation in the length scales has propelled the development of metastructures, expanding their possible uses in domains such as wave manipulation, impact absorption, and adaptive structures [25], [28], [100], [103], [106]. Fig. 2-9 illustrates one example of mechanical metastructures, showcasing a tilted stable configuration under axial loading. The top and bottom thermoplastic polyurethane (TPU) sheets are connected with thermally trained Nitinol wire. The temperature variance makes the sandwich panel exhibit a tilt in its overall structural stability, making it a Bi-stable thermally induced structure.

2.3.4 Shape Reconfigurable Mechanical Metamaterials and Metastructures

Smart materials can react to changes in their environment by deformations. Common examples include piezoelectric ceramics and shape memory alloys that convert electrical and thermal field changes into mechanical deformations. One pressing issue of these single-component smart materials is that their functionalities depend on their compositions with limited tunability. In

contrast, mechanical metamaterials and metastructures can program their morphing reaction into their unit cell topology. Programmability depends on the applications they are being used for, such as for aerospace and medical devices, a deployment mechanism is crucial. In contrast to the early stage of metamaterial design, when small linear deformations were considered for high specific stiffness and a tailorable Poisson's ratio. In recent years, large non-linear deformations, especially buckling and instability transformation, have been applied for programming large deformations [107]. The programmed deformation can adapt to various applications, allowing for specific deployment, redistributing stress, and absorbing energy. Mechanical metastructures accomplish shape reconfiguration through geometric transformation, i.e. shifting from one stable stage to another in response to external stimuli, such as axial mechanical load, temperature changes, or variations in wavelength [102].

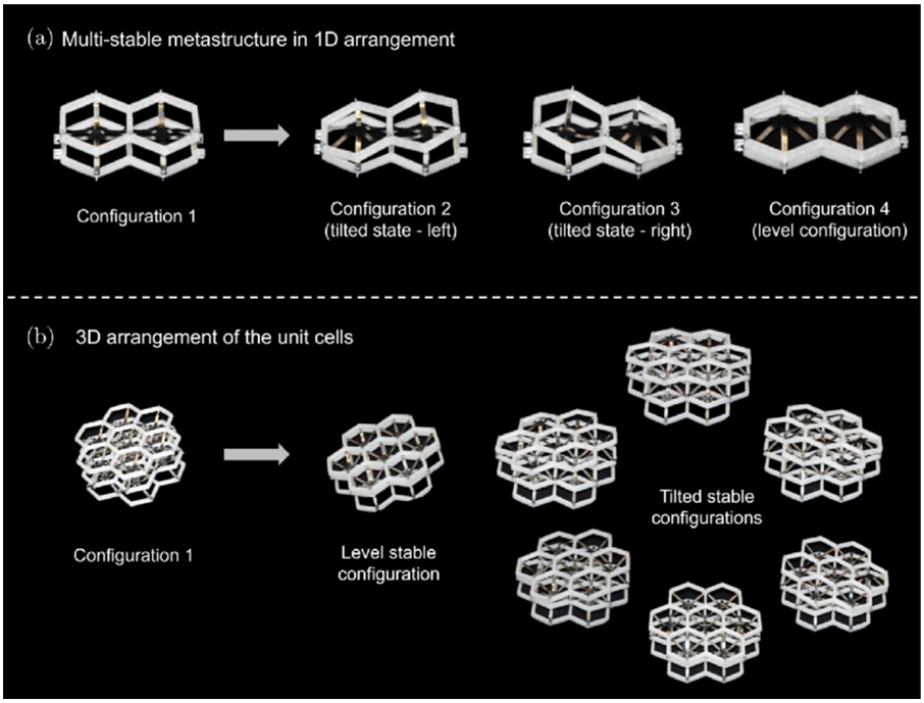

Fig. 2-9 Bi-stable hexagon metastructures with negative Poisson's ratio [108]

By mimicking traditional designs, small and simple mechanisms were developed in literature to reduce mechanical losses and enhance energy efficiency, including auxetic-based, origami and kirigami-based [107], and instability-based mechanisms. The auxetic mechanism designed on the principles of chiral or re-entrant unit cell placement permits a negative Poisson's ratio and greater flexibility [102]. The origami and kirigami-based [107] mechanism enable controlled shape

transformation of metastructures via mimicking pre-designed folding patterns and kinematic mechanisms. The folding mechanism is considerably more compact prior to deformation and expands to a larger size after deployment, making them suitable candidates for aerospace and medical applications where the size of the reachable envelope is crucial. Instability-based mechanisms, which purposefully use buckling and nonlinear responses to control deformation, are another important group [105]. The emergence of Bi-stable and multi-stable mechanisms enables structures to transit between multiple mechanical stable states without constant external energy inputs [109]. The aforementioned mechanisms have the potential to produce reversible shape changes for soft robotics and reconfigurable structures applications.

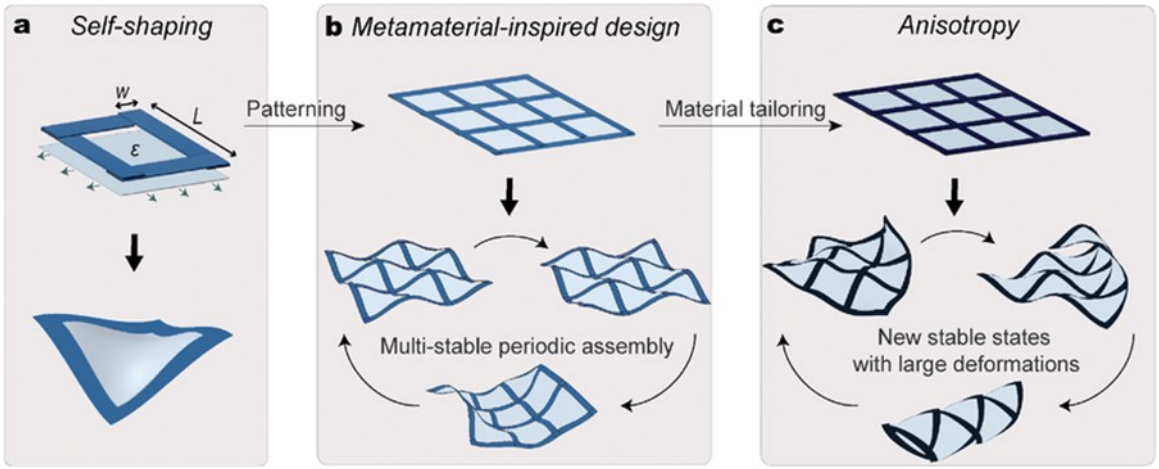

Fig. 2-10 Example of periodic cell placement for multi-stable design [110]

2.3.5 Mechanical Metamaterials and Metastructures with Bi-stability

Recent efforts have produced metamaterials and metastructures with morphing functionalities by mimicking the Bi-stable snap-through mechanism of the Venus Flytrap in nature. Bi-stable building blocks can reversibly snap between two or more mechanically stable positions, with strain energy reversibly stored and releases [111]. The Bi-stable mechanism has thus been a groundbreaking innovation in the deformation mechanism domain. The study of Bi-stable metastructures is emerging as a promising alternative solution for programmable mechanisms in metamaterials. For example, a Bi-stable sheet that can curl up under external stimuli is illustrated in Fig. 2-10. The Bi-stable concept can bridge the gap between dynamic, adaptive systems and static mechanical materials. Their multifunctionality, controlled deformation, and energy-efficient actuation make them a game-changer in robotic, medical, and aerospace applications.

2.4 Programmable Bi-stable Mechanism

As the world moves towards energy efficiency and sustainable solutions for every problem, the mechanics should also consider finding new ways of control, actuation, and deployment in extreme conditions, such as space, where even a 10-15% energy saving is considered a significant achievement. In recent years, the concept of Bi-stable structures has gained significance as a new approach, with examples seen in nature, such as the Venus Flytrap and the Impatiens genus [24]. These two examples illustrate the Bi-stable nature of leaves and seed pods, respectively. The Venus Flytrap (discussed in section 3.1) features two stable leaf forms, with the second stage activating when a fly lands on its inner surface. In a similar manner, plants of the 'impatiens genus' have seed pods that burst open when triggered by raindrops, insects, or wind. This concept was used to create shapeshifting in small toys, as illustrated in Fig. 2-11, where the origami-like structure of the ball has two distinct stages. Stage one represents when the radius is small. The ball transitions into the second stable stage when you stretch the ball; the radial dimension enlarges and moves to the second stable stage, increasing the size of the ball. This linkage connection and its structure inspire us to implement this design methodology to construct complex mechanisms for deployment, triggering, and other applications in aerospace, medical, and satellite industries [112].

Fig. 2-11 Expandable ball with multi-stable stages [113]

Bi-stable structures are characterized by the presence of two distinct energy states when analyzing the strain energy curve in numerical simulation. These structural designs mainly depend on reaching two steady states, which involve finding a local maximum and a local minimum on the strain energy curve. The local minimum in strain energy is defined as a stable point, i.e. when mechanical load disturbance is removed, the bi-stable structure will return to the stable point without external interference [24], [25]. The strain energy difference between these two points serves as an indicator of the stability of the post-deformed structure, providing insights into its

mechanical resilience. By tapping into Nitinol's super-elasticity obtained via its unique phase transformation properties, the proposed metamaterials can achieve large deformation without yielding or breaking. However, metamaterial and metastructure concepts that can explore different deformation modes with precisely tailored shape transformation, which can be programmed as per the applications, require further research.

This research introduces a novel category of Bi-stable metastructures referred to as "Meta-rod". The Meta-rod structures are capable of transforming between a rod-shaped stable stage and a target deployed stable stage, enabling various types of deformations, including linear translations, bending, twisting, as well as variations in area and volume. The specific deformation profiles can be meticulously programmed into the configuration of the Bi-stable structures, which are constructed using a tandem-tri-beam building block technique. By investigating the interplay between the symmetry of the building blocks and the resultant deformations, this project can design distinct deformation modes such as translation and twisting. Significantly, the Bi-stable structures retain precise control over programmed motion and deployment within a mechanically stable stage, thus optimizing the space and energy needed for maintaining shape integrity. This approach paves the way for exciting new applications in deployable medical devices, such as mapping and ablation catheters.

2.5 Research Objective

The overarching aim of this research is to develop a new family of programmable metastructures, termed Meta-rods, capable of achieving large, precise, and energy-independent shape transformations in cylindrical rod-shaped systems. The specific objectives are as follows:

1. Design and develop Meta-rod with five distinct morphing modes, i.e. linear, bending, twisting, area-expanding, and volume-expanding, each exhibiting a unique deformation mode suitable for deployable medical and robotic applications.
2. Develop a numerical simulation framework using finite element analysis (FEA) software (e.g. ABAQUS CAE) for parametric analysis and strain energy optimization to validate bistability and programmable deformation.
3. Quantify the deformation capacity of each model.

4. Establish a scalable and precise manufacturing methodology using computer numerical control (CNC) machining of Nitinol wires to enable reproducible fabrication of Bi-stable features across all Meta-rod variants.
5. Fabricate and test physical prototypes of all five Meta-rod models and experimentally evaluate their Bi-stable behavior, deformation stability, and repeatability.
6. To implement the Meta-rod concept into a functional mapping catheter prototype and evaluate its deformation performance under physiological conditions using a left atrium duplicator, aiming to eliminate reliance on external energy inputs or bulky actuation systems.

Chapter 3: Methodology

3.1 Concept Design

Deformations in nature occur as a reaction to environmental changes (i.e. applied load). For instance, the bi-layer pinecone scale structure demonstrates (Fig. 3-1a) how it responds to humidity: when the outer layers swell more than the inner layers due to wet weather, the scales curl inward, closing the cone. Similarly, the Mimosa Pudica plant showcases deformation through touch stimuli; its leaves close symmetrically due to the arrangement of their cellular geometry [114]. Both examples exemplify how the symmetric geometry of these natural structures contributes to their unique deformation behaviors.

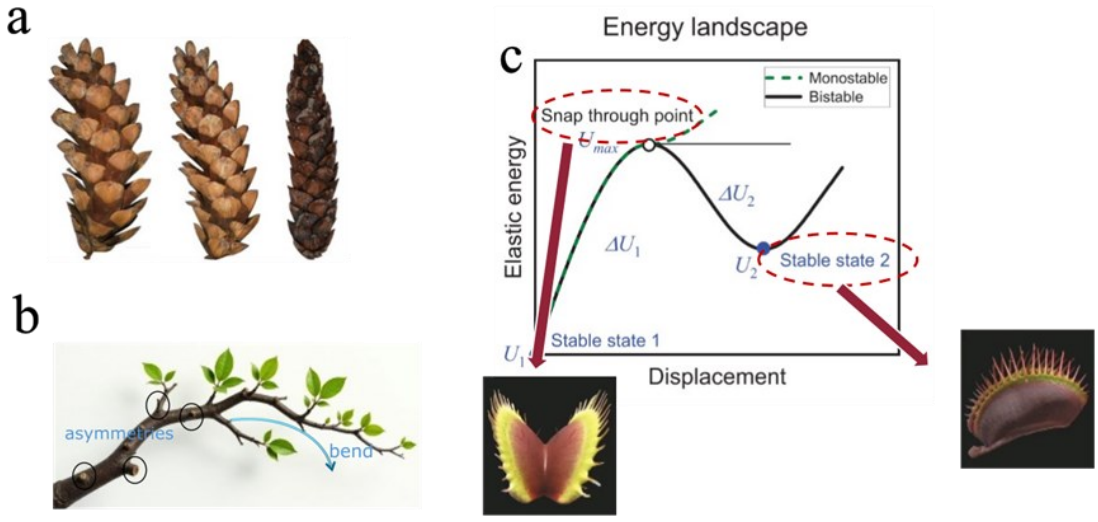

Fig. 3-1 Nature example of morphing structures: a) pinecone expansion via change in humidity; b) asymmetric growth on a tree branch causing a bend; c) snap-through behaviour of the Venus-flytrap plant representing bi-stability [115]

The following examples illustrate asymmetry in natural structures: tree branches with uneven notches or decay bend under their weight rather than compress uniformly (Fig. 3-1b). The Venus Flytrap's lobes, characterized by an asymmetric hinge structure, snap shut in a curved motion instead of closing linearly (Fig. 3-1c). Additionally, seashell spirals, which are asymmetrically shaped, display preferential bending when exposed to external forces such as water. Even in solid mechanics, a beam with unevenly spaced notches does not simply compress under

load but bends due to the imbalanced force distribution. Similarly, deployable solar panels and morphing aerospace structures use asymmetric hinges to control their unfolding behaviour [31], [37], [116]. By leveraging this knowledge, rod structures exhibit analogous behaviour when connected by hinges, transforming a rod into a tri-beam structure. Under vertical loading conditions, a tri-beam structure undergoes a shape transformation into a second stable configuration (Fig. 3-2).

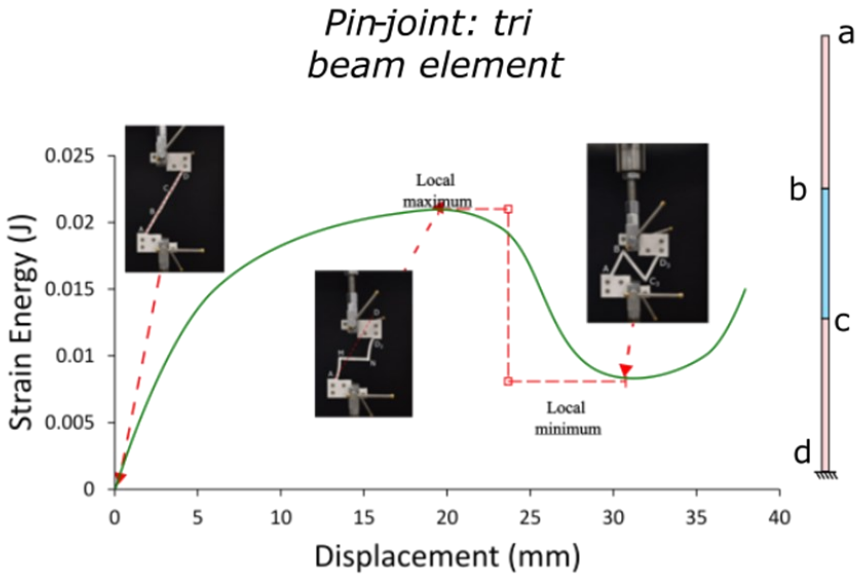

Fig. 3-2 Tri-beam element made of TPU and connected via hinges, exhibiting a Bi-stable nature.

3.1.1 Design Method

The proposed Meta-rod structures with programmable shape transformation and deformation functionalities are constructed via a Bi-stable rod building block, which is a tri-sectional straight beam concept as illustrated in Fig. 3-3. In the stable stage I, the three pin-joined straight beams are collinear with no initial deformation. When the top end moves straight down along the original axis, the structural strain energy is proportional to the bending and compressive/tensile deformation of the beam sections. The strain energy first increases and then decreases until the beam sections are collinear again in stage II. When all beam sections return to their original shape, the vanishing of deformation illustrates a zero-strain-energy stage. Introducing and subsequently removing disturbances around stage II, such as pushing or pulling the top end, allows the structural concept to revert to stage II, which is a mechanically stable stage.

Proposed Bi-stable building blocks (BBB) leverage stored strain energy to shift between stable states. Certain metals cannot withstand such stress without undergoing plastic deformation. A medical-grade alloy made from nickel and titanium, known as Nitinol, is widely used for its exceptional shape memory properties, particularly in the production of vascular stents. [117], [118], [119]. Nitinol has an additional quality that enables it to withstand significant strain changes before buckling and undergoing plastic deformation, known as its super-elastic property. This trait facilitates the investigation of Bi-stable phenomena in metallic structures without relying on shape memory properties. The tri-beam concept relies on hinges to undergo such deformation, requiring a complex assembly and manufacturing process. In order to realize a one-step manufacturing process that is compatible with the mass production of units, thin-walled compliant mechanisms replace the pin-jointed hinges (as illustrated in Fig. 3-4), crafting two notches on the surfaces of these rectangular rods. Fig. 3-4 Computer-Aided-Design (CAD) model shows the grooves made on the wire with specific dimensions, L is the total length and L_1 and L_2 are the two variable lengths which can be configured to find the optimal Bi-stable performance, which will be described in Sections 3.1.2.

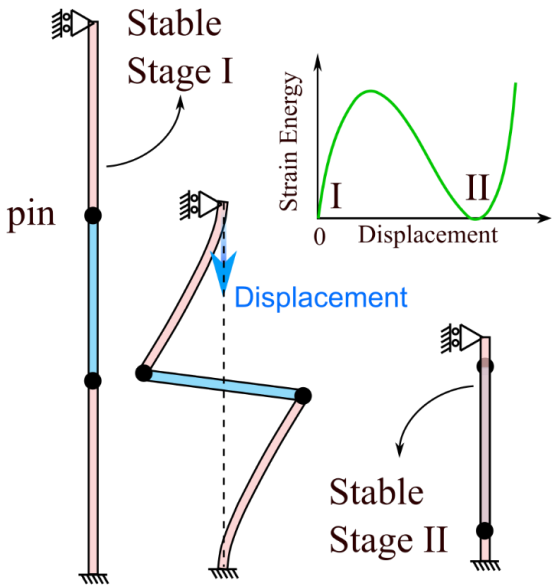

Fig. 3-3 Pin-joint-tri-beam element

To verify these properties provided by the supplier, Digital Image Correlation (DIC) testing was done on a small sample of the wire as shown Fig. A-5, the test gave similar properties with an error of 8% in the Young's modulus. The data from this test was used to calculate the material

properties of the sample. The samples used for creating the Meta-rod had dimensions as follows: "50×1.5×0.5 mm". Similar to that of the DIC test sample.

3.1.2 Design for Linear Model (LM)

The BBB is featured by the location and dimension of the two notches i.e. the thin-walled compliant mechanisms, as illustrated in Fig. 3-4a. The distance of the notches from the two ends and their thickness are represented by L_1, L_2, and t, respectively. The notch thickness is proportional to the beam thickness, T, and the notch length l is set to $0.1L$. Nitinol (a shape-memory alloy with $0°C < A_f < 10°C$, A_f is austenite transformation temperature) is used as the base material with a super-elastic behaviour at room temperature (20°C). The central region changes as we alter the lengths L_1 and L_2. By changing L_1 and L_2 lengths, we can move the notches along the complete length of the wire, altering the geometrical parameters of the model to attain bi-stability. The total length can be changed according to the application. Here, for the feasible manufacturing, we have considered L = 50 mm.

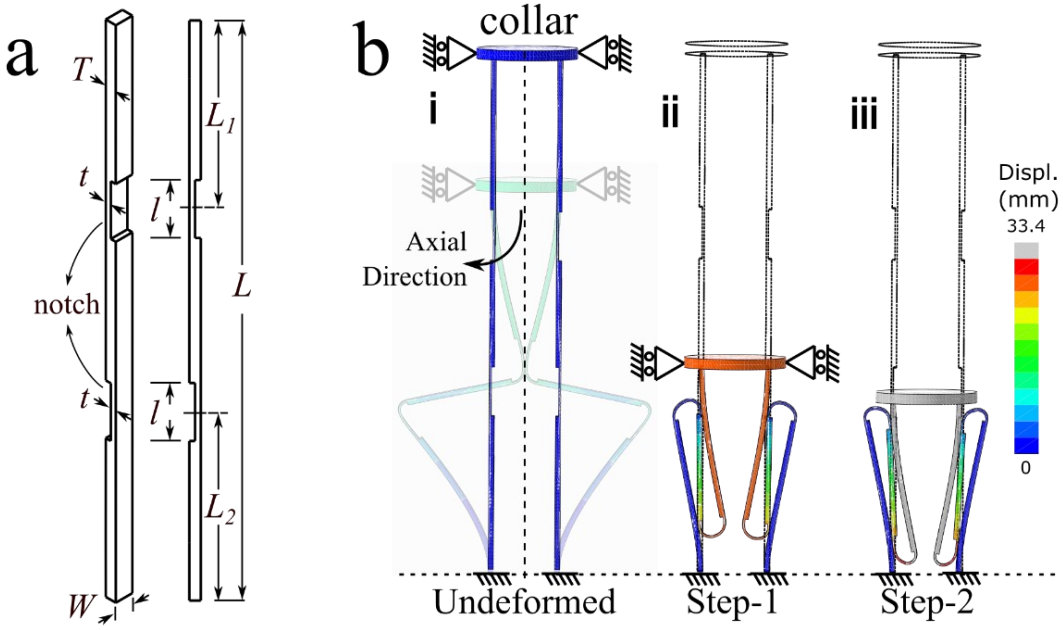

Fig. 3-4 Linear model concept design; a) Bi-stable building block; b) initial simulation of linear Meta-rod structure demonstrating bi-stability

Via simulation analysis, a tolerance range of 0.01 to 0.04 was observed to give similar bistability in a single model. Thus, the thickness of the notch was fixed to the entire thickness of the wire, and the relation obtained was as follows, as $t = 0.4T$. The lengths L_1 and L_2 are changed from 10% to 40% of L from both sides, to design a range of linear models that can exhibit varying

post-deformation lengths with strong bistability. As shown in Fig. 3-4b, to construct the model with linear deformation (i.e. linear model, LM), two BBBs are arranged in a left-right symmetrical position to build a Meta-rod unit cell. With the unit cell bottom fixed, when the top collar is compressed downward (by applying symmetrical loading conditions), the symmetrical structure (two BBBs in left-right symmetrical relationship) will result in symmetrical deformation, a linear shapeshifting, as they undergo symmetrical buckling, which results in uniform force distribution on a structure.

3.1.3 Design for Bending Model (BM)

Two BBBs are integrated into the linear unit cell (Fig. 3-4b) with a left-right symmetrical relationship. Under symmetrical loading conditions, e.g. compression along the axial direction, the resulting symmetrical deformation offers LD behavior of the Meta-rod (Fig. 3-4b). To investigate the effects of asymmetrical notch locations on the deformation modes, a new unit cell featuring left-right asymmetry is proposed for the bending model (BM). To do so, one side of the Meta-rod (left-hand side) is fixed, and the right-hand side's notches can be moved around the length of the wire.

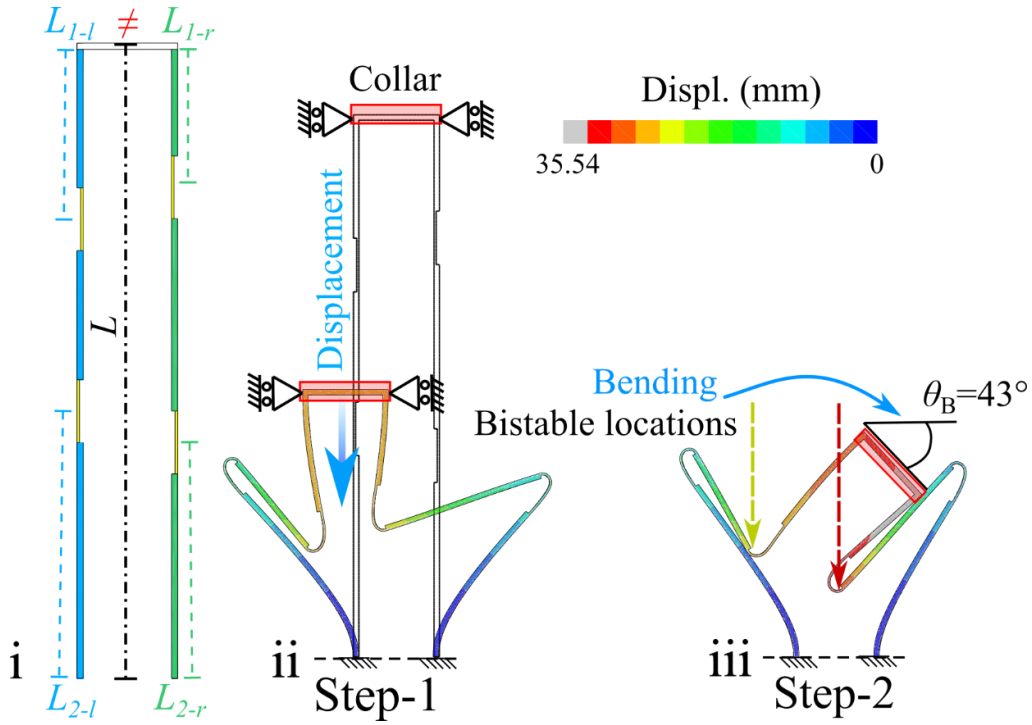

Fig. 3-5 Bending model design concept; i) bending mode Bi-stable building block; ii-iii) initial simulation of bending Meta-rod structure demonstrating bi-stability

In the left-right asymmetrical model (Fig. 3-5), the notch positions on the right side of the BBB (L_{1-r} and L_{2-r}) are varied unequally with respect to those on the left side (i.e. L_{1-l} and L_{2-l}). The mismatch in left-right notch positions causes the mismatch in Bi-stable locations. Analogous to pinecone scale bi-layer structures, which bend under identical humidity change, under identical dislocation on the top end (Step-1 in Fig. 3-5-ii), the mismatch in the structures results in a horizontal displacement of a free top collar. After compression is released in Step-2 (Fig. 3-5-iii), the second stable stage obtains a bending deformation (BD) mode with a bending angle defined as θ_B (Fig. 3-5-iii). Various bending angles of the Meta-rod can be tailored via adjusting geometrical parameters, e.g., the notch locations L_1 and L_2. Parametric study on the tailored notch locations can be performed via numerical simulations, where a local minimum in strain energy represents the existence of a mechanical stable stage.

3.1.4 Design of Twisting Model (TM)

In the twisting model (TM), four BBBs construct two bending elements, one marked in blue and the other in green (Fig. 3-6-i). The two bending elements are configured in a chiral arrangement, as shown in Fig. 3-6. Under a vertical compression, with the rotational degree of freedom fixed at the top end in Step-1, the vertical displacement independently triggers the snap-through of the two bending elements, indicating a deformed pattern in chiral symmetry.

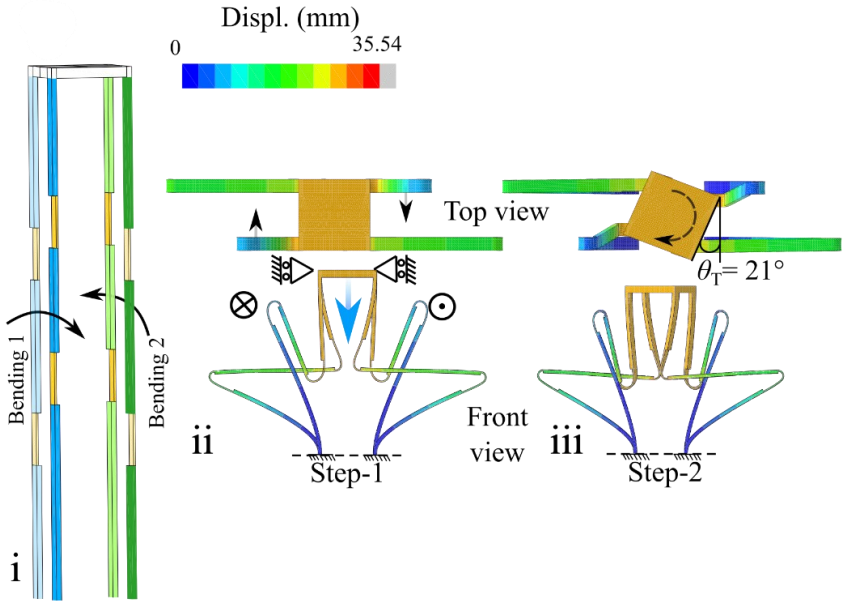

Fig. 3-6 Twisting model design concept: i) Bi-stable building block; ii-iii) initial simulation of twisting Meta-rod structure demonstrating bi-stability

After releasing the rotational degree of freedom at the top end in Step-2 (Fig. 3-6-iii), the blue and green bending elements turn in the opposite directions, which twists the top collar (Fig.3-6-iii). The interaction of these coupled bending actions produces a resultant torsional moment at the top surface, which ultimately leads to the observed twisting deformation of the surface, with a twisting angle defined as θ_T (Fig. 3-6-iii). The concept of chiral arrangement was verified via numerical simulations. Analogy to the bend aspects can be altered by changing the notch location, and the rotational angles in twist models can be verified via a numerical parametric study.

3.2 Numerical Simulation

The investigation presented here centers around a numerical analysis of nonlinear snap-through buckling deformation, a critical phenomenon in many engineering applications. Utilizing the highly regarded finite element analysis (FEA) package, Abaqus CAE, this study meticulously evaluated the behavior of structures under specific loading conditions. The analysis utilized the Standard Implicit Dynamic solver, known for its moderate dissipation properties, enabling accurate dynamic simulations of snap-through buckling. The proposed models were design in the ABAQUS part design interface via a python script to introduce parametric designing. The methodology involved a two-step simulation process. Step 1 was used to apply all the boundary conditions and displacement to the top face of the models. Step 2 was implied to check the bi-stability of the models, when all the restrictions are removed. The super elastic and standard material of nitinol in Abaqus material library were used for the simulation setup. To analysis the contact interaction between two BBBs, a general contact interaction was applied at the initial step which propagates in the remaining steps as well. Normal and tangential mechanical constraints were selected in the general contact interface and applied to the complete model. This general contact law was, crucial for preventing surface penetration during buckling transition. A reference point and a surface on the top face of the model was coupled to transmit the force in uniformity and symmetry on the complete structure. The boundary conditions in the step 1 were defined as follows: 1) a vertical compression in the form of displacement was applied on that reference point, which acted as the driving force; 2) the bottom face of the model was fixed; 3) all the degrees of freedoms were locked to facilitate the symmetrical deformation of the rods, with symmetrical force transmission and uniform buckling. In step 2, first and third boundary conditions were removed to make the model free, with only locking the vertical rotation of the model. This was crucial for the

simulation as this change reduced the computational time to solve the stiffness matrix and thus reducing the simulation time. The meshing strategy for this study utilized a standard 3D stress type element (C3D20R). This ensured accurate representation of structural behavior, with a seed size of 0.0002 generating over *3554* elements. The mesh provided the detail and precision needed to capture nonlinear behavior during buckling. To streamline modelling and to automate the simulation, a python script was used to parametrise the model creation in the Abaqus interface, enhancing efficiency and reducing human error in setup. Finally, the a combination MATLAB, Python scripts was used to extract local strain energy data from Abaqus's .obd files . This data was used to evaluated the bi-stability of the models. By analyzing strain energy, the study characterized energy states for various deformation modes. Nitinol's unique properties offered a valuable exploration avenue for bi-stability. Its shape memory and superelasticity allowed for a detailed analysis of structural performance under various loading conditions. Table 3-1 and 3-2 describes all the materials properties of Nitinol.

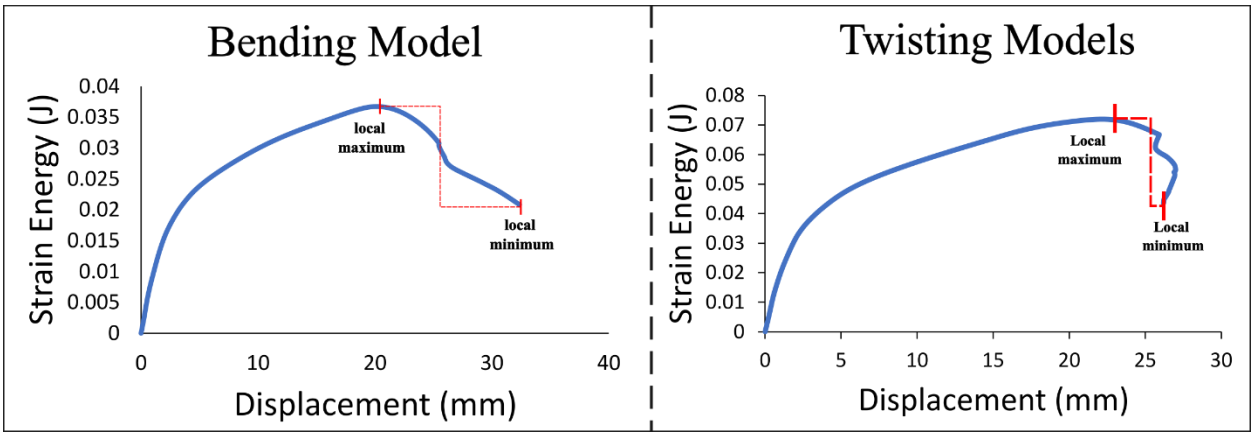

Fig. 3-7 Strain energy curve of bending model and twisting model showcasing energy barrier

The analysis of the data was used to produce contour plots, which proved instrumental in visualizing the performance of differing configurations relative to bi-stability. The findings underscored a significant relationship between geometric factors and performance outcomes (Fig. 3-8). Specifically, the analyses indicated that symmetrical notch placement emerged as the optimal configuration for achieving a robust Bi-stable response.

Table 3-1: Nitinol's basic material properties.

Standard material properties of Nitinol	
Density	6450 g/m^3
Young's modulus	$64647 \times 10^6\ Pa$
Poison's ratio	0.33
Damping	0.5

Table 3-2: Shape transition properties of Nitinol.

Nitinol's shape transition properties	
Martensite - Young's modulus	$28125 \times 10^6\ Pa$
Martensite - Poisson's modulus	0.33
Transformation strain	0.09
Start of loading	$449 \times 10^6\ Pa$
End of loading	$700 \times 10^6\ Pa$
Start of un-loading	$190 \times 10^6\ Pa$
End of un-loading	$30 \times 10^6\ Pa$
Load in compression	$449 \times 10^6\ Pa$
Reference Temperature	18.2° C
Loading	0.067
Unloading	0.067
Shape setting value	0.101

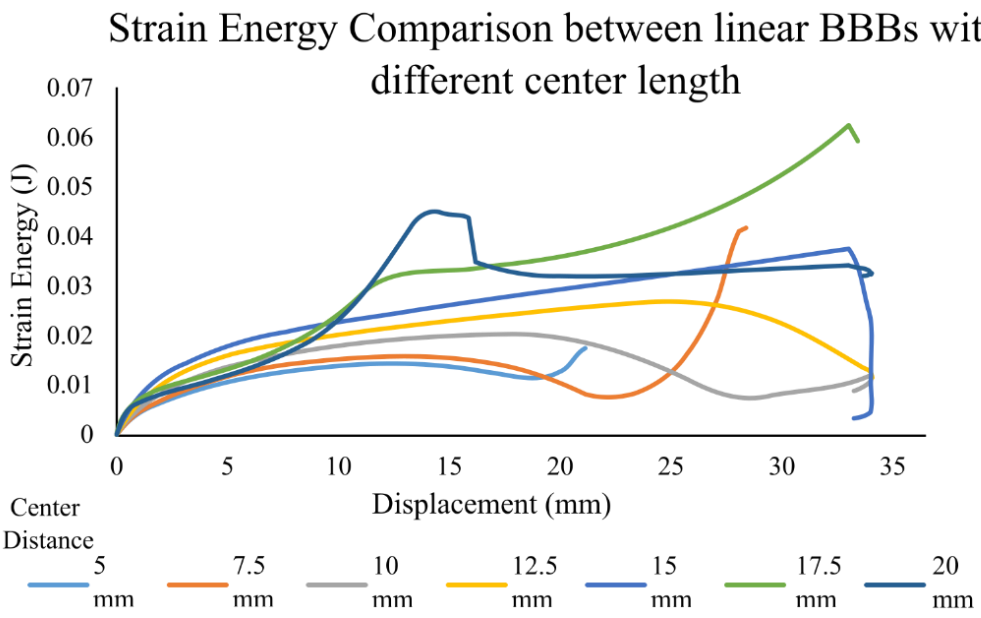

Fig. 3-8 Strain energy comparison of Bi-stable building blocks with varying central distance.

3.3 Manufacturing

Following the completion of the design phase for the linear, bending, and twisting deformation models, the manufacturing process was initiated to construct and validate their performance. The fabrication involved two primary steps: 3D printing the PLA collars and precision machining the Nitinol wire.

3.3.1 Nitinol Wire Machining Process

With an emphasis on accurate notch placement and surface polishing to guarantee Bi-stable behavior, the Meta-rod models were manufactured in accordance with the established design parameters. The notches were machined onto the wire to make it compliant, resulting in hinge-like grooves that permit deformation without thermal activation. Because of its hardness and flexibility, Nitinol wire presented several machining issues that necessitated a customized CNC G-code script-based automated machining approach. For high-precision milling, a tungsten carbide tool with a diameter of less than 1 mm was installed on a tabletop three-axis CNC (Genmitsu 3030-PROVer, SainSmart, China) as shown in Fig. 3-10. To achieve 75–95% accuracy in notch thickness, the CNC toolpath was created over several iterations. Early machining experiments revealed that heat accumulation during milling had a negative impact on the material's characteristics, especially when larger-diameter tools were used. The complete machine details and manufacturing set-up are

shown in Fig. 3-9. This was seen in post-fabrication deformation testing, where wires exposed to high temperatures exhibited reduced bi-stability and changed mechanical behavior.

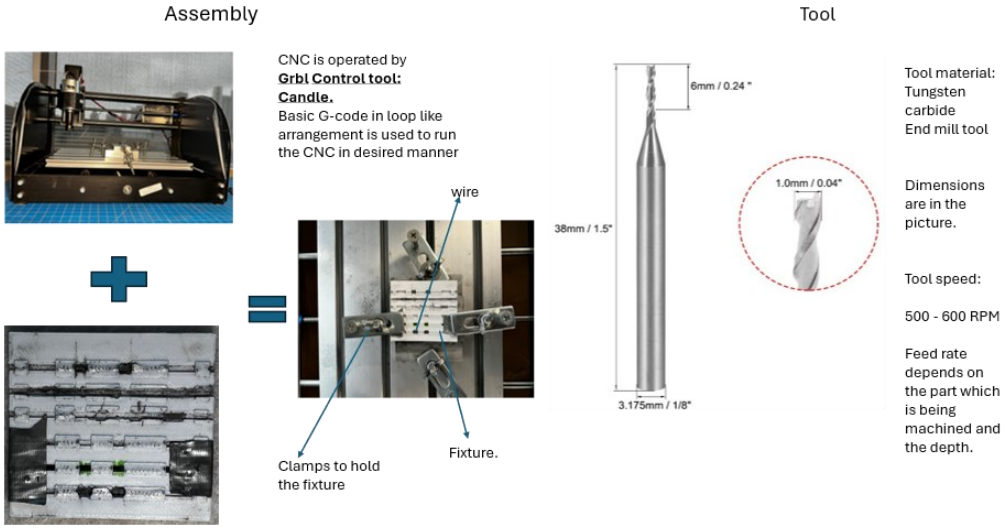

Fig. 3-9 Nitinol machining process and complete details

To mitigate these issues, the machining parameters were optimized to improve precision and prolong the wire's lifespan. Key adjustments included:

- Spindle speed: Set at 8000 RPM to minimize heat generation.
- Feed rate: Optimized at 15 mm/min for controlled material removal.
- Coolant application: A diluted soap–water coolant (Sunlight®, Canada; 1:20 soap-to-water ratio) was applied to regulate surface temperature below the martensitic transformation threshold while simultaneously reducing metal oxidation during machining.
- Vibration control: Vibration control was achieved by clamping the nitinol wire in a rigid aluminum fixture to dampen high-frequency modes, while spindle speed (500 rpm) and feed rate (0.05 mm/s) were optimized through trial cuts to minimize chatter and produce a uniform surface finish..

The final post-machining process, if required, involved surface grinding to eliminate tool wear artifacts and ensure a smooth finish. This structured approach ensured that all meta-bar models were manufactured with high precision and durability, ready for assembly with the 3D-printed collars in the final deployment mechanism.

3.3.2 Manufacturing of Fixture-Collars using Additive Manufacturing

The fixture-collars for securing the Nitinol wires were fabricated using additive manufacturing, ensuring a precise connection between the wire and structure. 3D printing enabled the rapid production of customized collars for each deformation model. PLA (polylactic acid) was chosen for its ease of handling and strong adhesion, securing the Nitinol wire effectively. Each model, linear, bending, and twisting, had unique design requirements, leading to multiple CAD designs to meet different mechanical constraints. The fabrication utilized Bambu Lab and UltiMaker 3D printers, with adjustments for precision and durability.

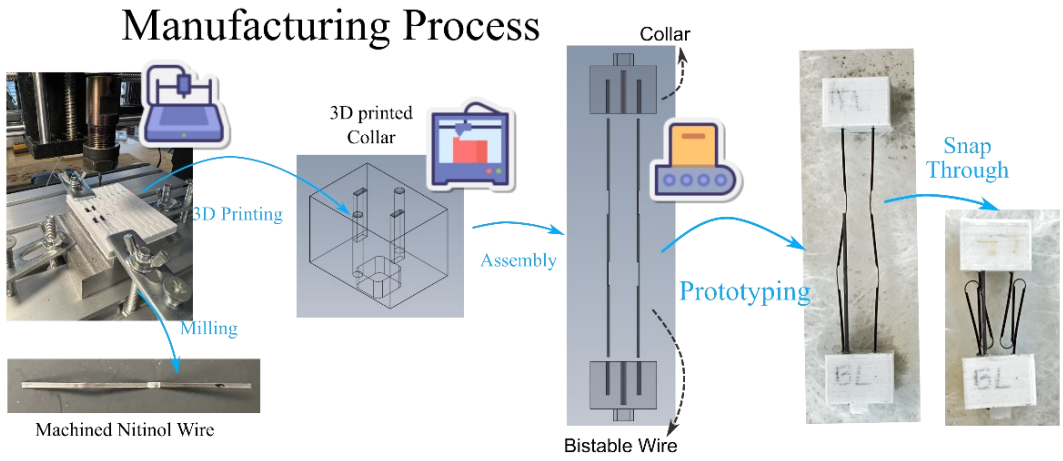

Fig. 3-10 Complete manufacturing process

Designing and printing PLA collars for small rectangular slots (1.5 mm × 0.5 mm) posed challenges due to shrinkage and resolution limitations. Initial trials with the UltiMaker-3 Extended 3D printer faced difficulties because the 0.4 mm nozzle restricted the reproduction of sub-millimeter features. Switching to the Bambu Lab printer improved accuracy and resolution for fine-featured prints. Slot dimensions were enlarged by 13% to compensate for material shrinkage and ensure a proper fit post-printing. An iterative approach refined the design through adjustments in print parameters and model dimensions. Various collar configurations were manufactured, including arrays of holes at different distances, to optimize wire placement for controlled deformation via trial and error. The final collars provided the necessary stability while maintaining flexibility for Bi-stable deformations, enabling the assembled system to withstand mechanical loads during testing.

3.4 Surface Area-based Mapping Catheter Model

The above-mentioned BBB exhibits a 2-D shift transformation, which considerably limits the spatial shape-reconfiguration possibilities. To solve this significant problem, we have introduced an innovative tri-notch BBB along with its rotational symmetrical arrangement, both before and after deployment (Fig. 3-11). The tri-notch building block is based on a tri-beam model concept. However, when compared to the original building block, the first section is notably shorter and the third section is deliberately longer, featuring one additional notch in the third section designed for bending instead of bi-stability. Under a vertical compression, the structure demonstrates its inherent Bi-stable nature by remaining firmly in the second stable state, as shown in Fig. 3-11-ix and vii. The first notch enables the building block to deform into a distinctive U-shaped geometry at the deployed stable stage. The extra notch allows the third section to bend outward, enabling a part of the third section, measuring a length of L_2, to be perpendicular in relation to the rod's axial direction. Under the principles of rotational symmetry, four or more tri-notch building blocks can effectively generate a “wire spoke” pattern, which creates a circular disk-like shape. The generated disk-like area provides an opportunity for embedding multiple electrical sensors nearby, thus making the signal mapping process significantly more efficient. The L_2 value governs the radius of this disk area and is optimized to a maximum based on insights gathered from a comprehensive simulation study. The key geometric parameters were established in Fig. 3- -11, with the total length limited to $L = 45$ mm to comply with catheter design constraints.

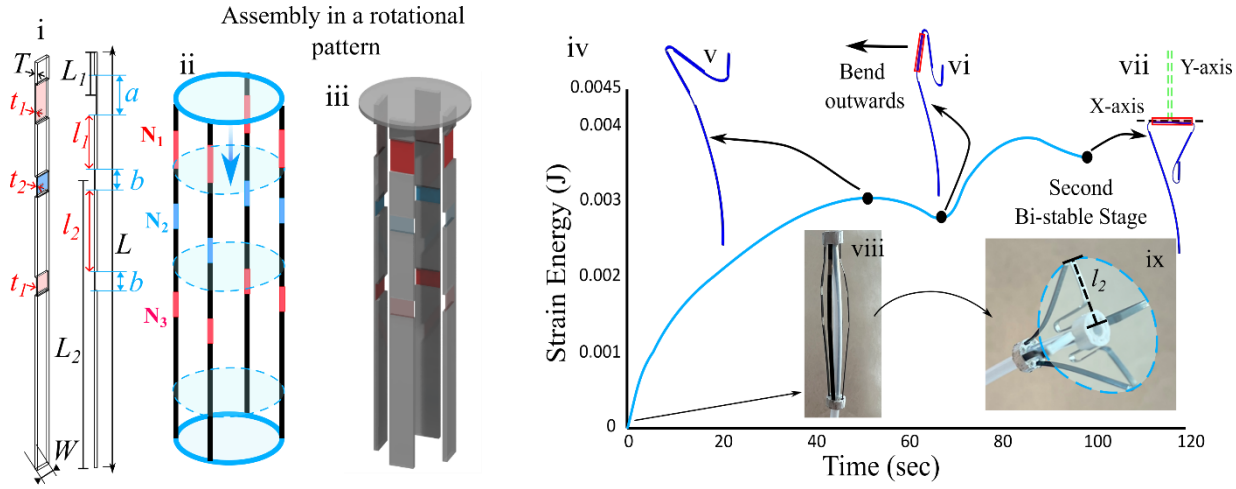

Fig. 3-11 Area model design concept; i) three notch bistable building block; ii) Rotational symmetric placement of three notch bistable building block; iii) CAD assembly model; iv - vii) strain energy profile of the three notch bistable building block; viii - ix) initial prototype of the proposed catheter design

A numerical parametric analysis was performed to evaluate the geometrical dimensions of the tri-notch building block. The length and position of the first notch are a = 4.3 mm and 2.5 mm from the top. The length of the second and third notch is set to b = 2 mm (see Fig. 3-11-i). The notch thickness is evaluated through numerical simulation, resulting in a tolerance range of t_1 = 0.105-0.125 mm and t_2 = 0.075-0.105 mm, while the wire's overall thickness is T = 0.3 mm and width is W = 1.5 mm (Fig. 3-11-i). Two span lengths, L_1 and L_2, were introduced to govern bi-stability and area, respectively.

3.5 Volumetric Model (Balloon Catheter Replacement)

To effectively model a balloon-like structure, a volume-generating transformation must be implemented to replicate a spherical configuration. The challenge presented by a notch-based approach for generating a Bi-stable wire in this context is significant; therefore, an alternative solution is proposed: employing an LM that serves as a locking mechanism, coupled with thinner spline elements designed with notches to form a shape reminiscent of a balloon (Fig. 3-12). BBBs operate as self-locking mechanisms, enabling the design of a hybrid volume model that integrates flexible spline elements arranged strategically around the Meta-rod. Upon the compression of the Meta-rod, the splines expand outward, prompting a transition of the volume model from its initial stable rod state to a secondary volume stable state.

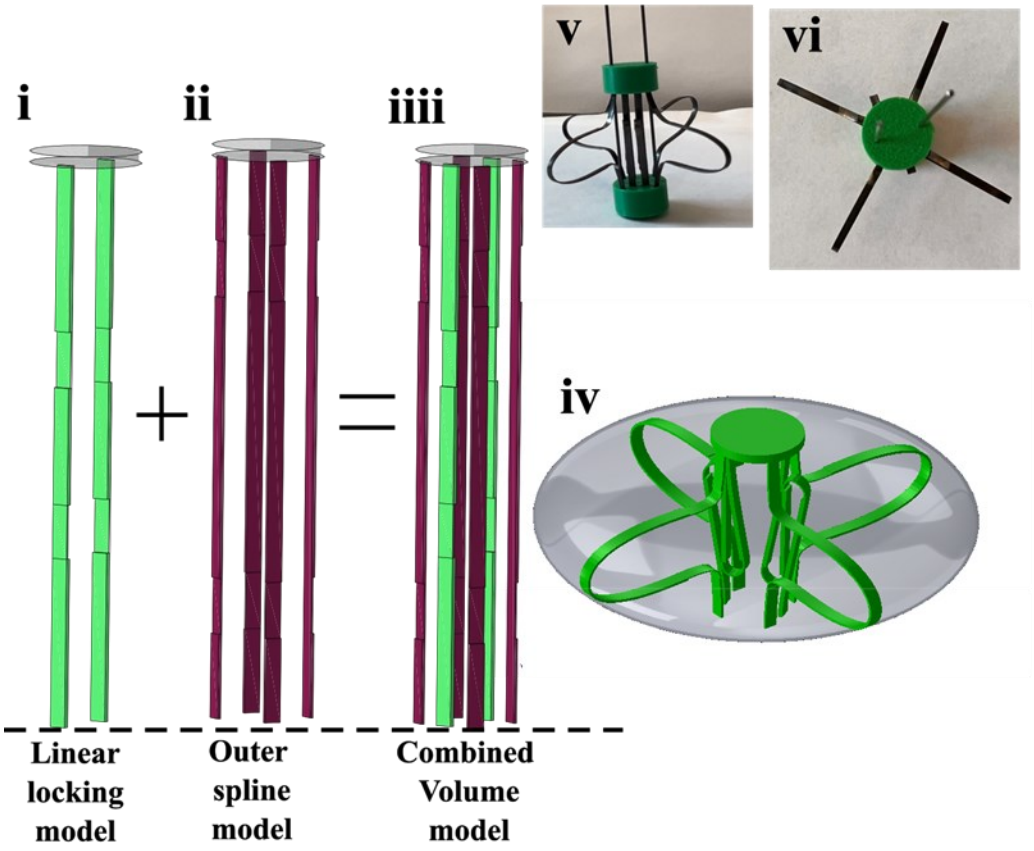

Fig. 3-12 Volume Bi-stable model assembly and deformation profile design

This transition creates a desired volumetric profile at the second stable stage, which can be tailored meticulously to accommodate various applications, such as a balloon-catheter cross-section or more complex, application-specific envelopes, thus allowing for an array of deployment configurations. The top circular collar was fabricated through 3D printing using PLA filament. Once deployed, the rod's stored strain energy maintains the volumetric profile, assuring structural integrity independently of pneumatic or hydraulic systems. By exploiting the self-locking features inherent in the BBBs, we enable passive and programmable volumetric transformations by modifying the volume design accordingly.

3.6 Triggering Mechanism Development

The triggering mechanism for the Bi-stable structure was developed to facilitate the deployment and retraction of the mapping catheter's active element without requiring continuous external energy. The key design objective was to ensure controlled actuation while maintaining

structural stability during deformation. This mechanism was integrated into a tendon-driven deployment system, allowing for remote activation via a handle-based control interface.

Table 3-3: Deployment mechanism components and material

Component	Material	Properties/Notes
Catheter Body	Nylon	Durable, flexible, excellent mechanical properties.
Collars	PLA (Polylactic Acid)	Biocompatible, good for precise manufacturing.
Smaller Tube (Ablation Catheter)	PTFE (Polytetrafluoroethylene)	High chemical resistance, minimal friction.
Tendons	Nylon	High strength and flexibility, good wear resistance.

The deployment mechanism was designed to operate using a dual-trigger system within the handle mechanism. When activated, one trigger applies tension to the tendons, engaging the Bi-stable structure and shifting it into its deployed configuration. A second trigger enables retraction, ensuring that the structure returns to its initial state. This method eliminates the need for external mechanical supports, allowing the mapping tool to be positioned precisely within the atrium. The Bi-stable nature of the structure ensures that once deployed, the mapping element remains stable until the retraction trigger is engaged, preventing unintended movements during the procedure.

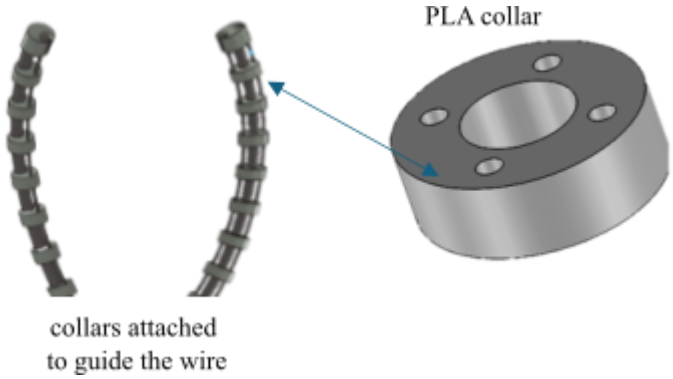

Fig. 3-13 CAD assembly design of deployment mechanism

The manufacturing process of the deployment mechanism involved the fabrication of two essential fixtures to support the Bi-stable transformation. A fixed fixture was anchored at the catheter tip, while a movable fixture was designed to slide along the catheter body, engaging or disengaging the Bi-stable structure as required. These components were 3D-printed using PLA, ensuring high precision and compatibility with the catheter's flexible framework.

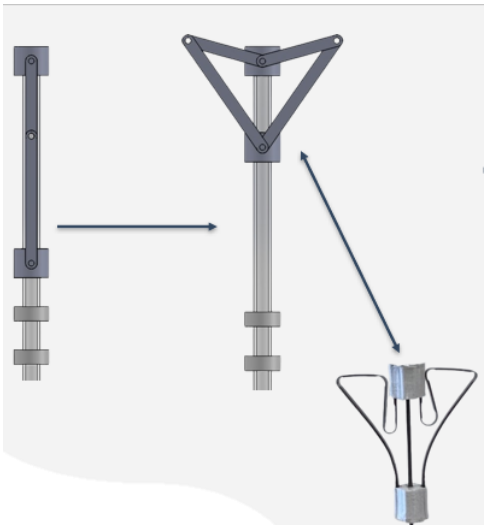

Fig. 3-14 Assemble design and prototype the integration of nitinol wire

3.7 Mechanical Testing Setup

Tensile testing machine was used for the force analysis and material properties verification for DIC testing. A 500N and 10 kN load cell was used for the respective tests. Fixtures were designed to hold the Nitinol wire and collar on the tensile machine. Fig. 3-15 is one of the examples of these testing, it represents the DIC testing of the Nitinol wire sample.

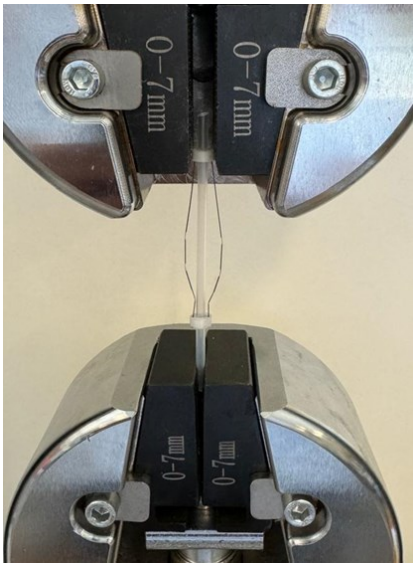

Fig. 3-15 Compression test to study the triggering force of the area model

3.8 Static-Test Setup for Areal Model

Static testing refers to fluid-less environment testing, where the deployment mechanism is assessed under controlled conditions without external flow influences. To conduct these tests, a real-size Left Atrium (LA) model was fabricated using 3D printing. The base model was 3D printed in PLA and then coated with clear silicone (XIAMETER RTV-4234-T4, Dow Corning, MI, USA) to create an elastic representation of the heart cavities. The fabricated LA model, designed to mimic anatomical features, is shown in Fig. 3-16.

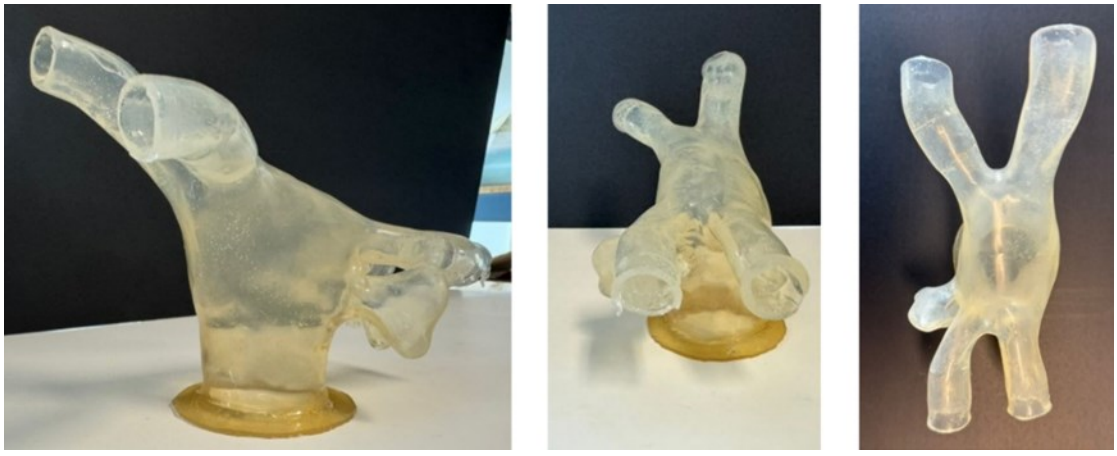

Fig. 3-16 Silicon Left Atrium model

For testing, the LA model was securely fixed to a table using clamps, ensuring stability during catheter insertion. The catheter was gradually introduced through the right pulmonary vein, progressing into the LA chamber in its un-deployed state (as shown in Fig 3-17). Once the catheter reached the center of the LA, deployment testing was conducted to evaluate the functionality of the triggering mechanism. These tests should verify whether the Bi-stable structure and tendon-driven actuation system performs as expected, ensuring controlled and precise deployment within a realistic anatomical model.

3.9 Dynamic-Test Setup for Areal Model

A dynamic test was performed under a controlled fluid flow environment. A customized left ventricle duplicator was used for this study. LA was attached to the top of the LV in this setup. The above-mentioned LA model was 3D printed by referring a complete adult human heart using a CT and MRI scan (Solid Heart Gen 2 Zygot: American Fork, UT, USA). This LA model was anatomically placed on the LV to replicate the actual human heart positioning. This model had a pulmonary vein with an appendage to ensure the realistic flow of blood inside the system [120], [121]. The key characteristics of this model include a base-to-apex measurement of 90 mm, a maximum width of 70 mm, a maximum depth of 50 mm, a left ventricular outflow tract diameter of 32 mm, an end-diastolic volume of 155 ml, and an aorto-mitral angle of 166° [122], [123]. The duplicator creates the intended physiological flow and pressure waveforms by simulating the realistic extraction and expansion of the left ventricle by hydraulic activation. An airtight hydraulic chamber that is attached to a piston cylinder arrangement encloses the LV and LA. A specialized LabVIEW (National Instruments; Austin, TX, USA) graphical user interface controls a linear motor (LinMot P01-37 × 120, NTI AG; Spreitenbach, Switzerland) that drives the piston [120], [121], [122], [123]. When the piston moves forward, the ventricle contracts, which results in the ejection (systole) through a bioprosthetic aortic valve; when the piston moves backward, the diastole, or filling phase, occurs, during which the aortic valve shuts, and the mitral valve opens.

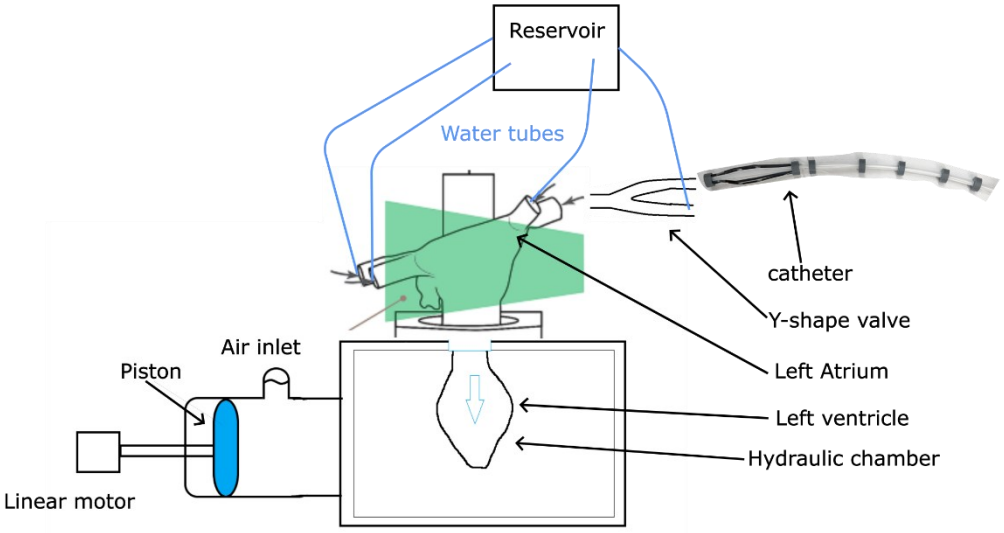

Fig. 3-17 Block diagram of dynamic testing apparatus

The four pulmonary veins of the LA are then connected to pipes which lets the fluid flow through it (as illustrated in Fig. 3-17), creating an actual heart pump situation. This set-up helped to test the catheter model in a realistic condition and gave us the required testing scenario to validate the bi-stability of the design under specific/ desired physiological blood flow and pressure waveforms, which are generated by an actual heart inside human body. The right superior pulmonary vein (RSPV) and right inferior pulmonary vein (RIPV) of the LA was used to insert the catheter inside the LA, as the whole system should be a closed loop to let the fluid flow properly throughout the operation experiment, a Y shaped valve was attached to the RIPV of the LA model, and the RSPV was connected to the fluid tank. This Y shaped valve had two outlets one had a fix value to let us insert the catheter and the other mouth was again attached to the fluid tank to complete the loop. For the testing of the catheter tip stability, the simulator was turned on before inserting the catheter to replicate the actual operational conditions. Catheter consisting of the Bi-stable device tip was inserted into the LA model (as illustrated in Figs. 3-15 and 16). Once reached to the desired position it was deployed from the outside to its next stable position.

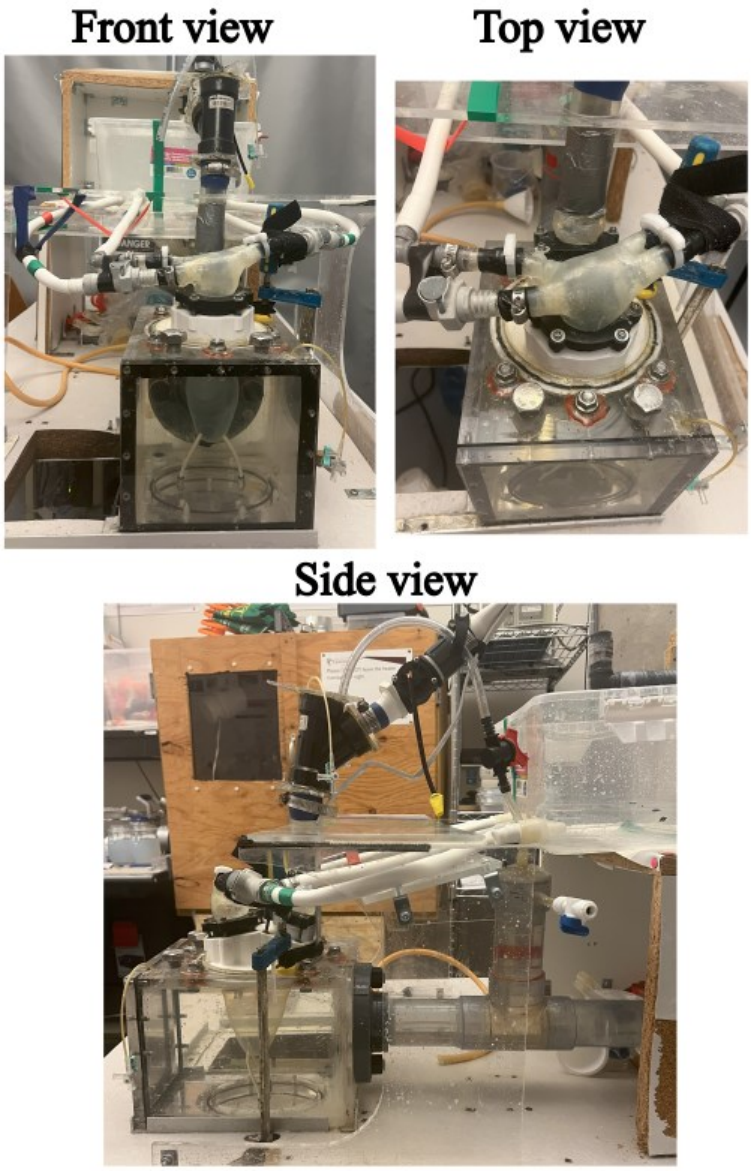

Fig. 3-18 Left Atrium duplicator setup

3.10 pH Paper Test Setup

To evaluate tissue, contact regions, small $1\ mm^2$ pH indicators were affixed to the surface of the Nitinol wire. The precise 1×1 mm pH paper dots were fabricated using a CO_2 laser cutter, ensuring accurate and repeatable cuts. A long strip of pH paper was initially secured onto an acrylic plate using adhesive tape, as illustrated in Fig. 3-19, to facilitate laser cutting.

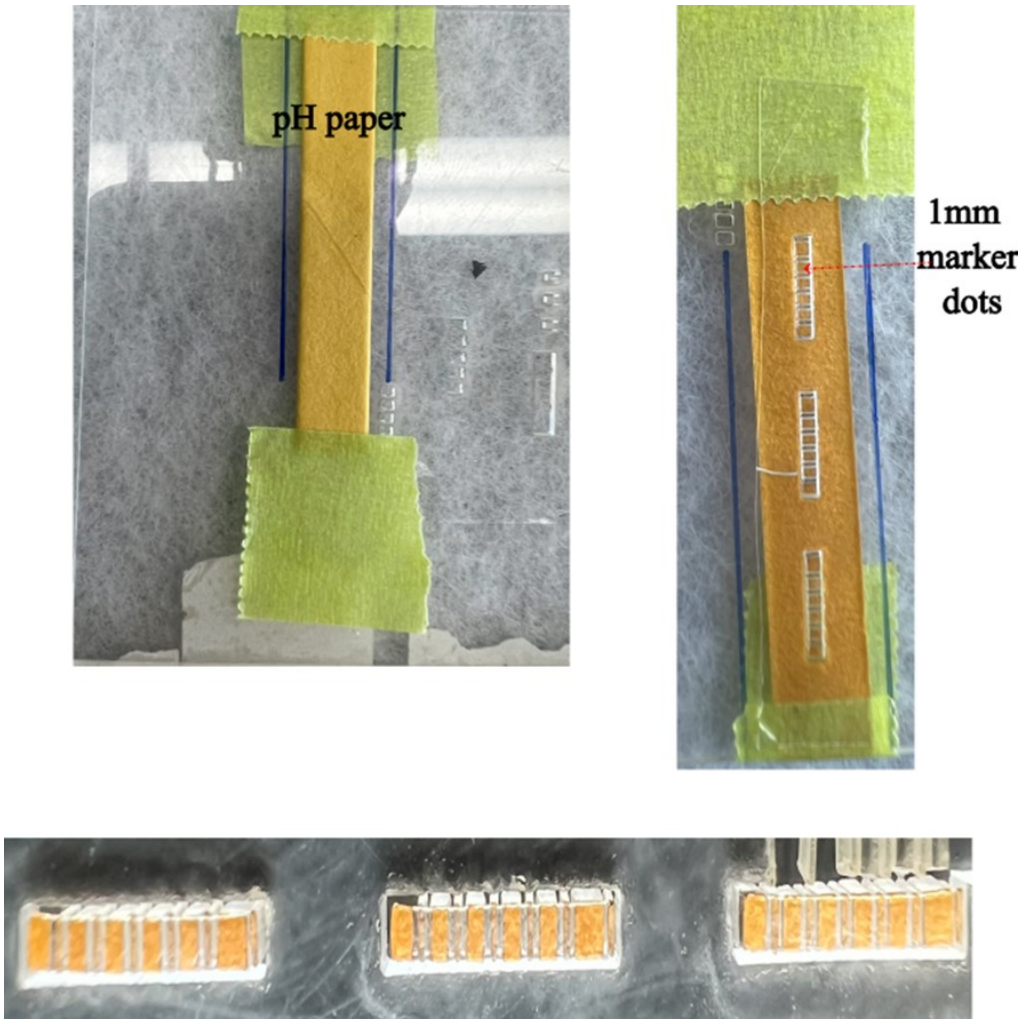

Fig. 3-19 Laser-cut pH paper strips samples with 1 mm size pH indicators

For the initial trials, a single array of pH dots was cut to validate the process parameters. Once optimized, multiple arrays were generated in a single cycle, cutting 2–3 pH strips simultaneously to increase efficiency. Following the cutting process, a thin, transparent adhesive sheet was applied to the surface of the pH strip. This allowed for easy transfer of the pre-cut pH dots from the acrylic plate onto the Nitinol wire, ensuring proper adhesion while maintaining the integrity of the markers for subsequent deployment and contact assessments. Fig. 3-20 shows how the complete process of laser cutting and making the sensor strip samples for the tissue-sensor contact test.

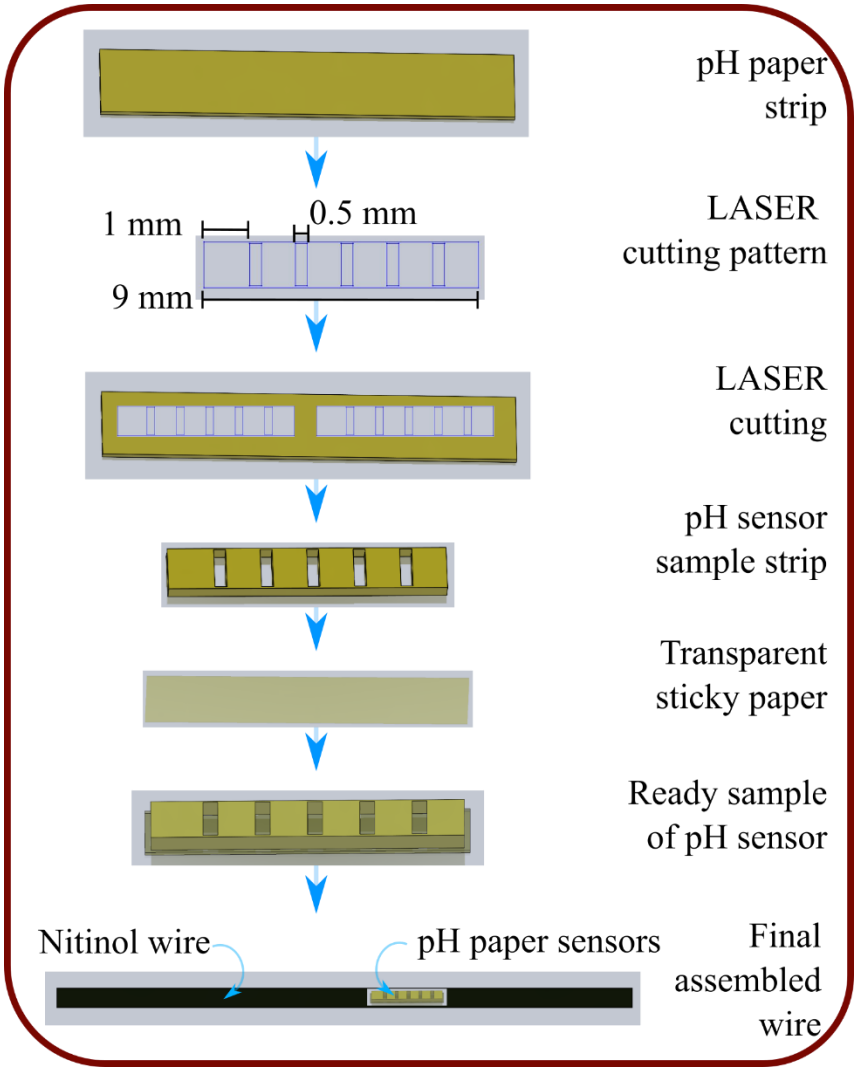

Fig. 3-20 Flow chart diagram of laser-cut pH paper sensors

Chapter 4: Results and Discussion

4.1 Bi-stability Criteria

A simulation study was conducted to evaluate the bi-stability and deformation of an LM by varying two parameters, L_1 and L_2. Not all configurations exhibited bi-stability, underscoring the mechanism's sensitivity to parameter changes. To investigate the presence and intensity of bi-stability, strain energy and force-displacement data were extracted from ABAQUS ODB files using Python scripts and MATLAB. The strain energy curve, which reflects Bi-stable behavior, yielded two essential values: the maximum strain energy (E_{max}) and the minimum (E_{min}).The bi-stability can be appraised via a ratio of the local minimum and local maximum of the strain energy $\varepsilon = \frac{E_{min}}{E_{max}}$ called as the bi-stability indicator, was calculated to assess bi-stability, following established methodologies [45, 46, 47, 43].

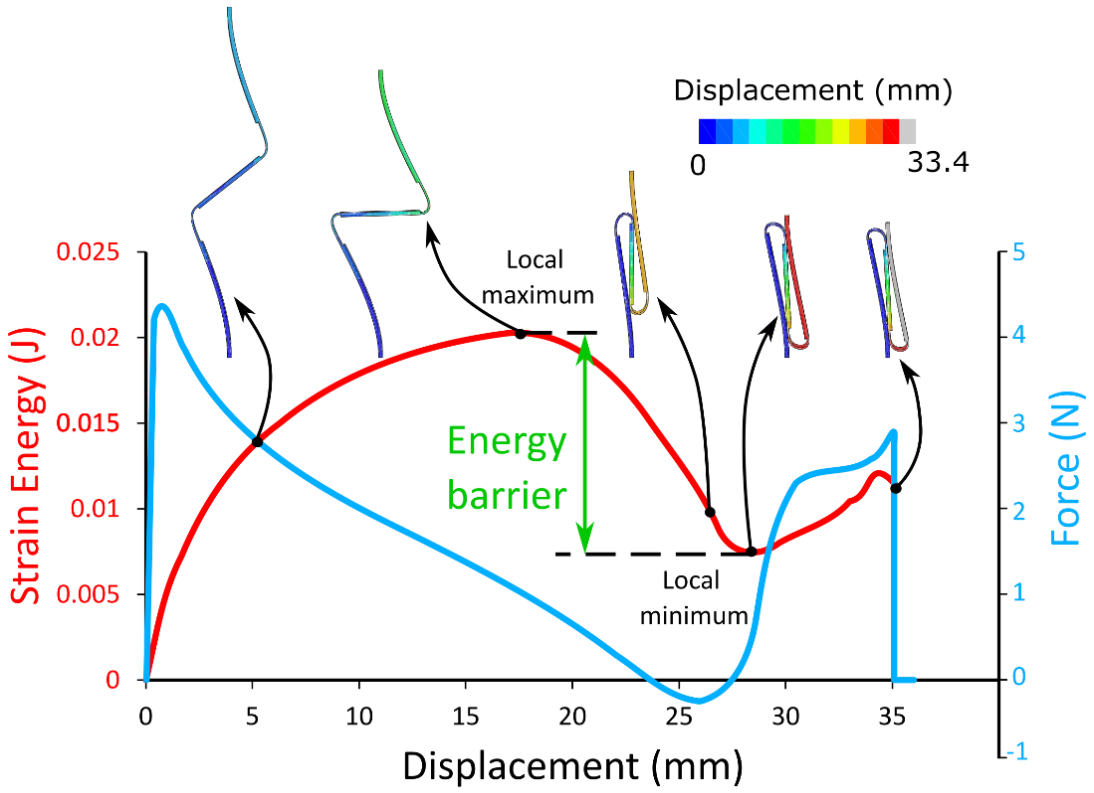

Fig. 4-1 Strain energy vs Force vs Displacement curve representing the bi-stability concept.

The ε value near to zero exhibits a strong bi-stability, while as the value increases the bi-stability starts to decrease. This is caused by the decrease in energy barrier as shown in Fig. 4-2. The theoretical mono-stable stage is represented by $\varepsilon = 1$. The range of ε for stronger Bi-stable models was observed from 0.29 to 0.89 in the simulations, while the models with ε in the range of 0.9 to 1 displayed mono-stable nature. Bi-stable behavior was also evident in the force-displacement curve, as illustrated in Fig. 4-1, which features a clear peak followed by a decrease to zero force, indicating a transition between stable states. After this point, the structure released potential energy, thereby lowering the energy barrier (as shown in the linear BBBs simulation in Fig. 4-2).

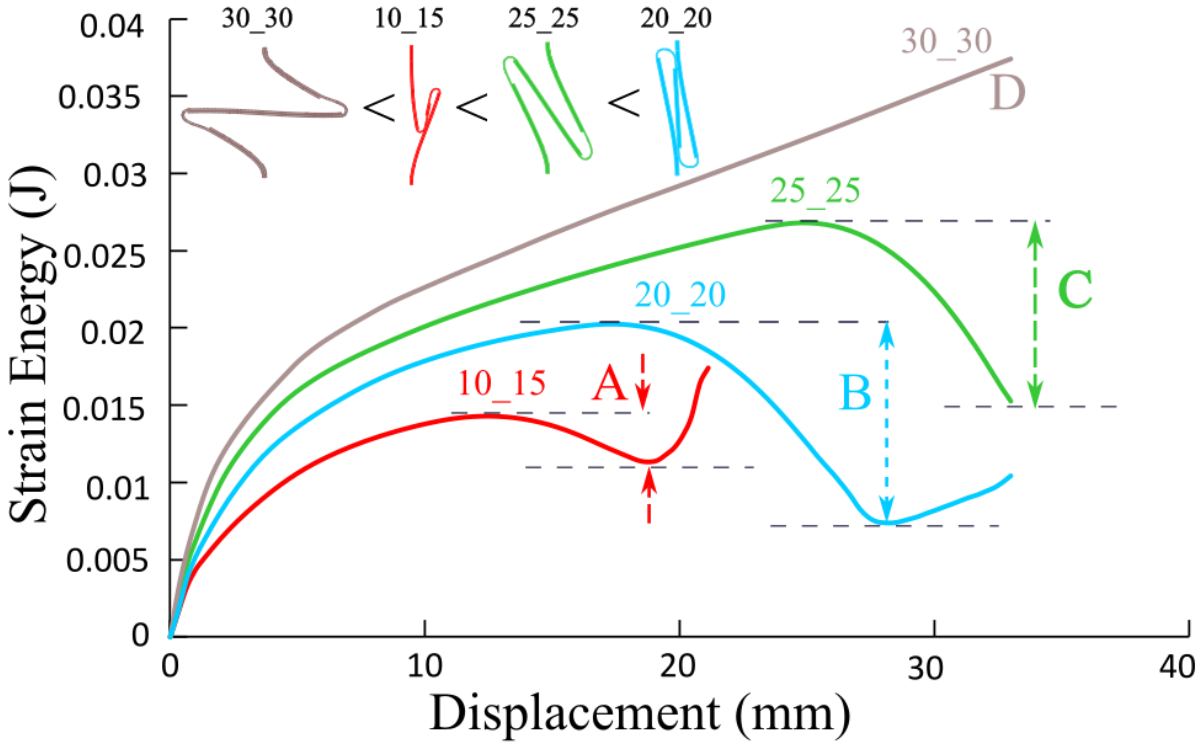

Fig. 4-2 Strain energy curves exhibiting the difference in energy barrier

4.2 Linear Model

In this section, numerical simulations, verified by physical testing, reveal the relationship between the geometrical parameters (e.g. L_1 and L_2 in Fig. 3-4) and the programmable bi-stability

(e.g. LD at the second stable stages). The value of $\varepsilon = 1$ represents $E_{min} = E_{max}$, i.e. a mono-stable structure. In contrast, for a Bi-stable Meta-rod ($\varepsilon < 1$), energy barrier, $E_{min} - E_{max}$, represents the disturbance resistance of the bi-stability. While the value of closer to zero represents a strong bi-stability, a Bi-stable structure with a value of near one is less resistant to the disturbance. In this study, L_1/L and L_2/L change from 10% to 40%, respectively, with step length of 5%, thus generating seven distinct values of each of the notch locations for L_1 and L_2.

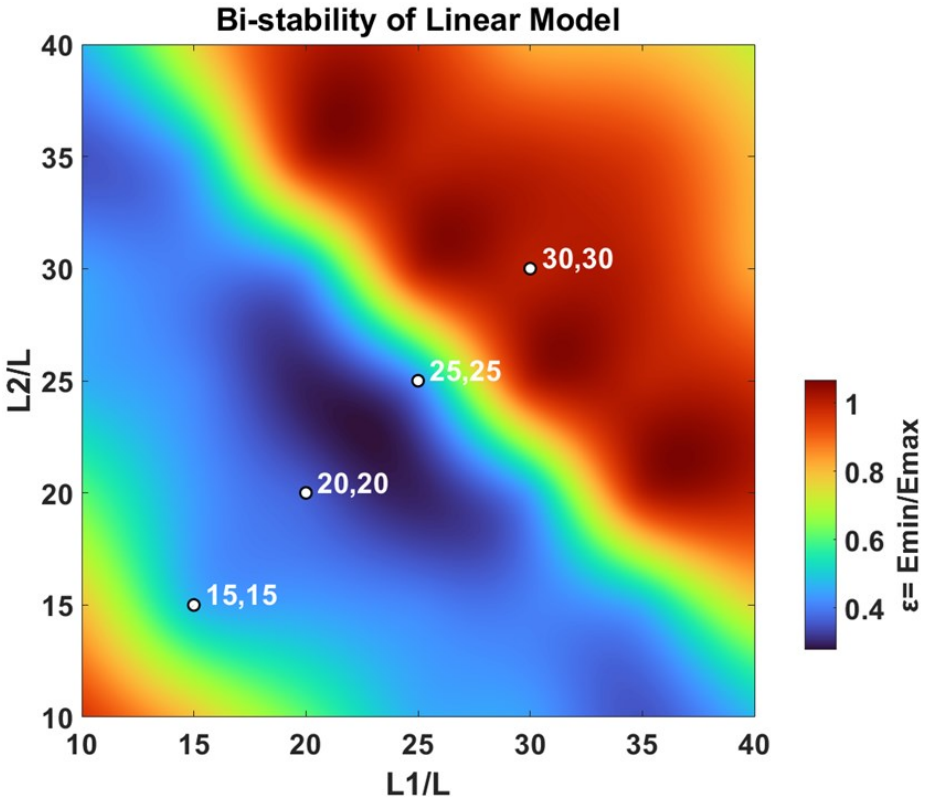

Fig. 4-3 Contour plot of bi-stability of the linear model Meta-rod

Contour plot Fig. 4-3 compares the bi-stability and the corresponding LD of 49 different configurations. The models are represented in the following format: "$^{L_1\text{-Left-side}}_{L_2\text{-Left-side}}L^{L_1\text{-Right-side}}_{L_2\text{-Right-side}}$." The model with L_1 = 15 mm and L_2 = 15 mm (represented by '$^{20}_{20}L^{20}_{20}$' in Fig. 4-4) has the lowest value of $\varepsilon = 0.2943$, showing in dark blue shade on the plot, which has the strongest Bi-stable energy constraints. While the model with L_1 = 17.5 mm and L_2 = 17.5 mm (represented by '$^{25}_{25}L^{25}_{25}$' in Fig. 4-4) has $\varepsilon = 0.5781$, with the energy barrier ($E_{min} - E_{max}$) defined in Fig. 4-2, less than that of the

‘ ${}_{20}^{20}L_{20}^{20}$ ’ model, which shows a weak stable stage at the end of step-2. The snap-through behavior in the BBBs results from the symmetric buckling of the nitinol wire. When notches are placed on opposite surfaces, they deform symmetrically, creating a zig-zag bending mode. This in-plane zig-zag deformation helps release strain energy and prevents unwanted out-of-plane snapping.

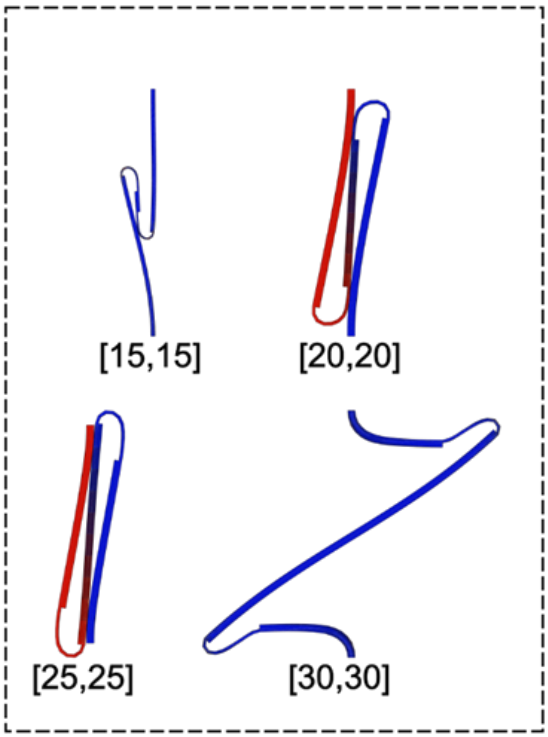

Fig. 4-4 Different linear models.

It was clear from the contour plot that as the distance between the two notches increases, the bi-stability starts to vanish. If we attempt to manufacture a model with a center distance less than 5 mm, the energy barrier is almost zero, resulting in very small bi-stability (Fig. 4-2). When the notch distance went above 13.5 mm the models had $\varepsilon > 0.89$, as represented by the ‘ ${}_{30}^{30}L_{30}^{30}$ ’ on the contour plot, with red color zone representing mono-stability. The contour plot (Fig. 4-5) represents the LD analysis for each simulated model with actual displaced length at the second Bi-stable stage. The Bi-stable structure with notch locations L_1 and L_2 = 15 mm has a displacement D_{15} = 33.526 mm at the second stable stage. The models with a center distance between 5 - 10 mm show the displacement in the range of 20 - 33 mm, which enables programmability in linear displacement. The energy barrier defined above depends on the length of the middle section of the beam; Fig. 4-2 shows LM with different lengths of the middle section. As the length increases from

5 mm to 15 mm the bi-stability also increases, i.e., the energy barrier also increases. It was observed that as the middle section length goes beyond 17.5 mm the bi-stability vanishes, which gives us insights onto the extent of this novel concept.

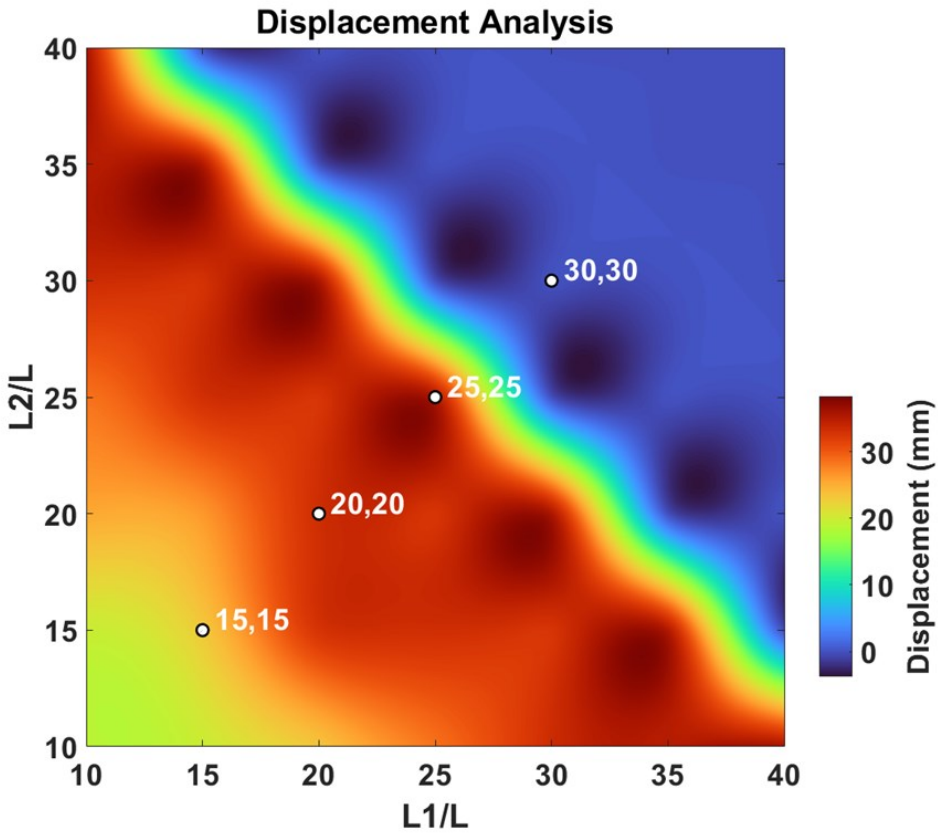

Fig. 4-5 Linear model deformation analysis

4.3 Bending Model

The LD model is designed as a combination of BBBs as defined in Fig. 3-4. Applying the bi-stability criteria specified in section 4.1, a similar simulation analysis was performed for the BM. The evaluation of bi-stability in the BD model involved altering the notch position parameters L_1/L and L_2/L and examining contour plots that illustrated both the bi-stability ratio ($\varepsilon = \frac{E_{\min}}{E_{\max}}$) and the bending angle. Effective notch locations of the unfixed side (right-hand side in Fig. 3-5) are varied within the range of 20% - 34% for L_1/L and 17% - 33% for L_2/L, respectively. The models are represented in the following format: "${}^{L_1\text{-Left-side}}_{L_2\text{-Left-side}}B^{L_1\text{-Right-side}}_{L_2\text{-Right-side}}$." For simplicity, eight distinct

values of each of the notch locations for L_1 and L_2 were selected in model construction to generate a step length of approximately 2%. Contour plot Fig. 4-6 demonstrates the bistability and the corresponding bending angle of 64 distinct configurations.

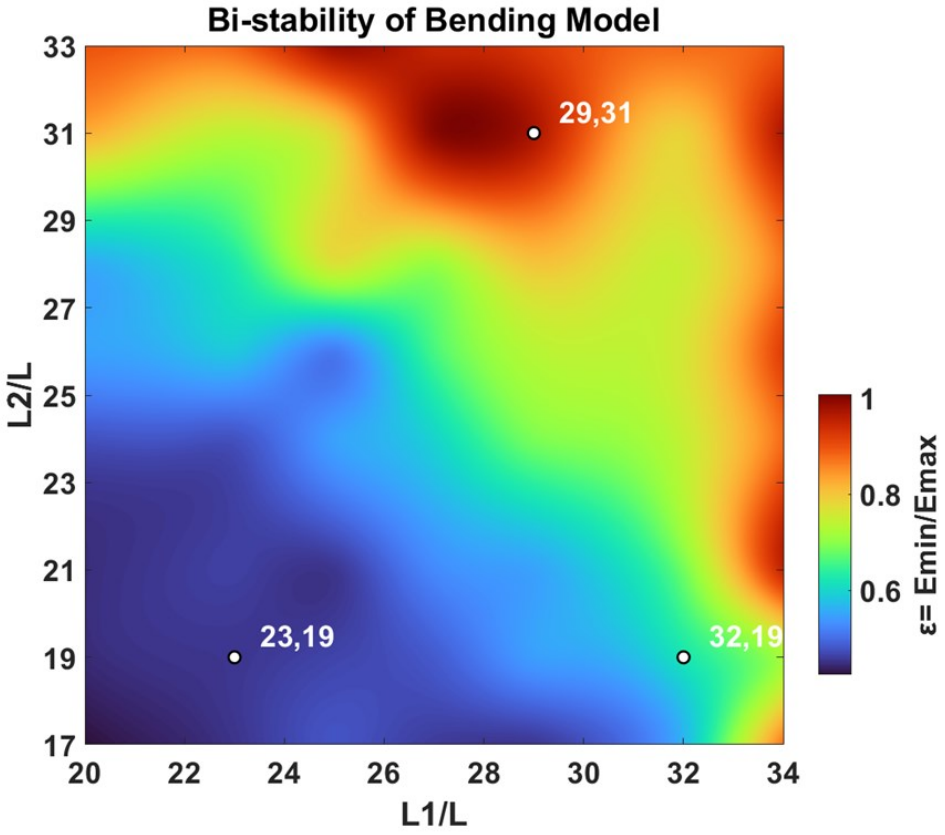

Fig. 4-6 Contour plot of bi-stability of the bending model Meta-rod

The asymmetric relationship between the notches of both rods in bending units weakens the mechanical boundary conditions and decreases bi-stability. In the contour plot shown in Fig. 4-6, the dark blue shade on the plot shows strong Bi-stable energy constraints. The ${}^{18}_{23}B^{19}_{23}$ model (Fig. 4-7) featured notch positions that closely mirrored those of the fixed rod, resulting in the strongest Bi-stable Meta-rods achieved in simulation, with a bi-stability indicator $\varepsilon = 0.398$. With an increase in L_1 or L_2 (Fig. 4-6), the ε value increased, indicating a decrease in bi-stability. For example, the model with ${}^{18}_{23}B^{32}_{19}$ has $\varepsilon = 0.586$, which still shows a strong bi-stability (represented by '[23,19]' in Fig. 4-7). as the values of L_1/L and L_2/L increased beyond 32% and 26%, respectively, the ε value continued to increase gradually from 0.624 to 0.978, indicating a vanishing of bistability (shown as a dark reddish orange color). The angle is donated by 'θ_B'. Thus,

higher parameter values resulted in bending angles reaching 48°–50 °. The increased angle range was accompanied by a reduction in bi-stability due to stress concentrations caused by asymmetry, which are mainly induced on the notch surfaces.

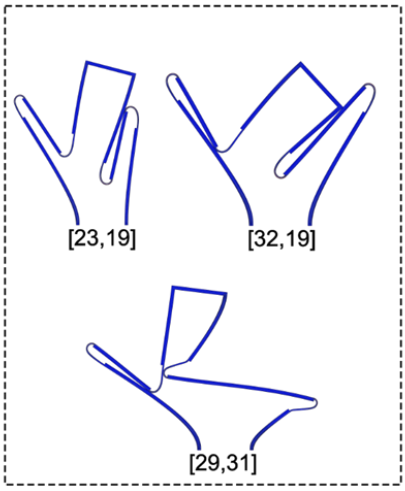

Fig. 4-7 Different bending models

The strain energy profile of a BM is shown in Fig. 3-7. Further investigation was carried out to calculate the bending angle generated by simulated models.

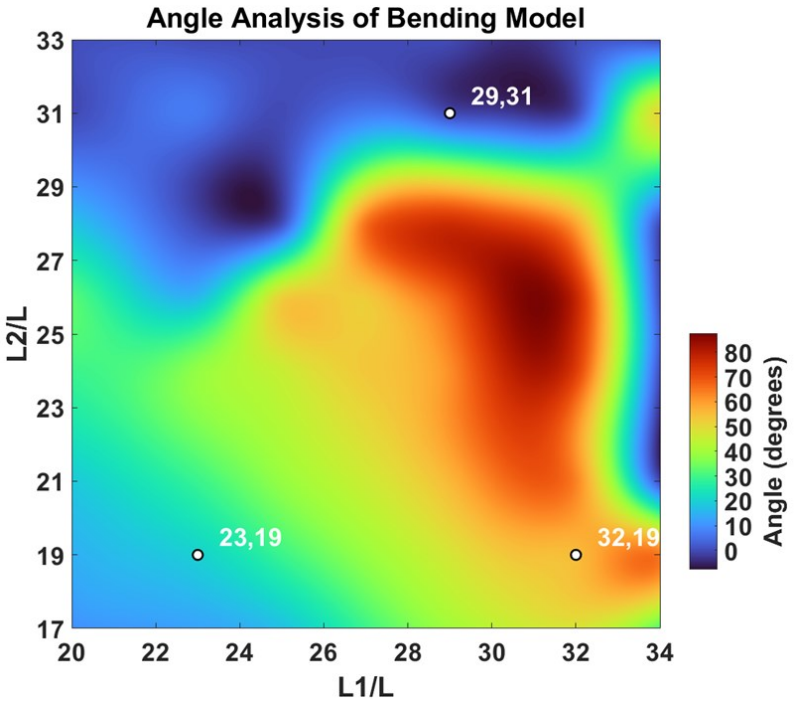

Fig. 4-8 Angle analysis of bending model

As the distance between two notches increases, the bi-stability decreases. Weakened Bi-stable structures allow a high deflection tendency, resulting in an increase in the corresponding bending angles. The bend angle values for the ‘ ${}^{18}_{23}B^{19}_{23}$ ’, ‘ ${}^{18}_{23}B^{32}_{19}$ ’, and ‘ ${}^{18}_{23}B^{19}_{31}$ ’ models were noted as $\theta_B = 9.5°$, $\theta_B = 43°$, and $\theta_B = 0°$, respectively.

4.4 Twisting Model

Following the examination of BD and its related bi-stability and angles, a specific contour plot for TD was analyzed to pinpoint optimal parameter regions. As illustrated in Fig. 4-9, the TD map was divided into three sections based on bending parameters. The top-right section was determined to be monostable absence of bi-stability in the BM configurations in that region. The bottom-left area corresponded to bending angles below $\theta_B = 8–10°$, which, in simulations, resulted in twisting angles of ‘$\theta_T = 2 – 3°$’ (point 21_20 on Fig. 4-9), which are negligible, as the respective bending angles for those models are minimal. The twisting model is represented as follows: “ ${}^{L_1\text{-Left-side}}_{L_2\text{-Left-side}}T^{L_1\text{-Right-side}}_{L_2\text{-Right-side}}$ ”.

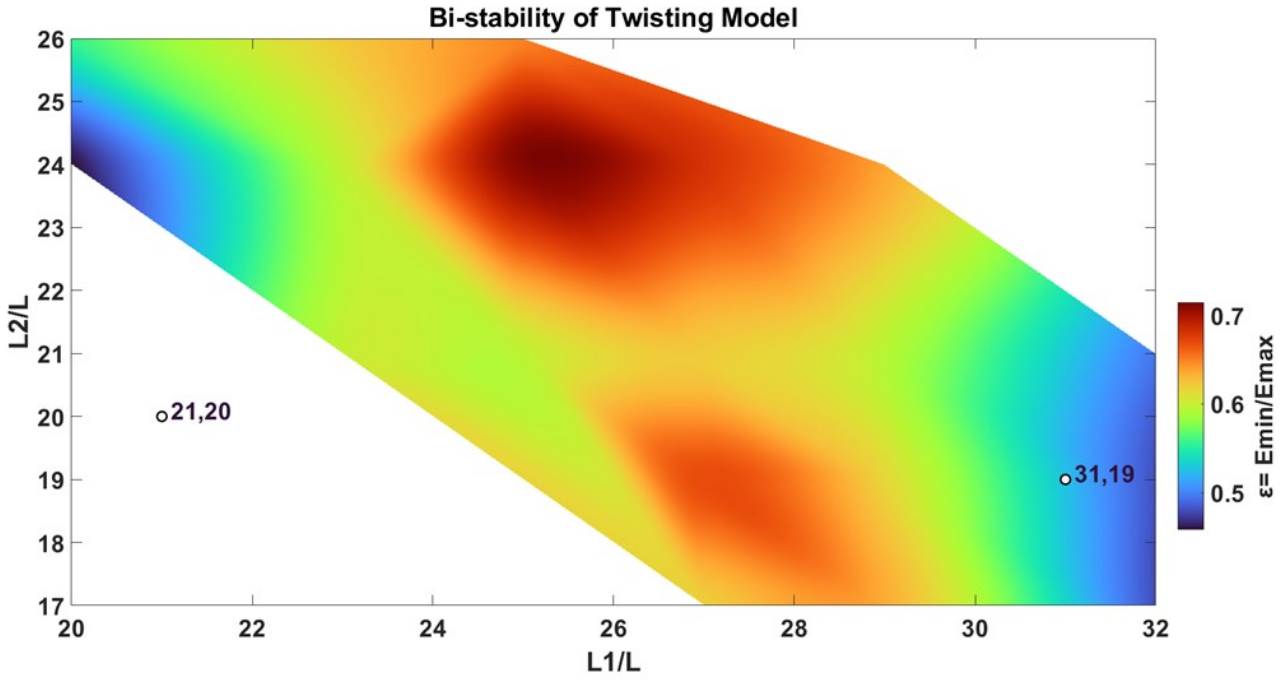

Fig. 4-9 Contour plot of bi-stability of the twisting model Meta-rod

The largest bending angles can be achieved with $L_1/L \in [26\%, 32\%]$ and $L_2/L \in [24\%, 26\%]$, Bi-stable twisting concepts appear in the same location which exhibited ε values between 0.4 and 0.55, showed notable bi-stability alongside advantageous twisting angles. The '$^{18}_{23}B^{32}_{19}$' bend model, which corresponds to a θ_B = 43° bend angle, was selected for prototype twist model concept, resulting in a twist of θ_T = 18°, which closely aligns with the simulation outcome of θ_T = 21°. Although the upper-right region permitted potentially larger angles, it lacked the energy barrier necessary for dual stability. The prototypes illustrated that chiral geometries can efficiently convert bending-induced asymmetry into programmed twisting (as illustrated in Fig. 4-10).

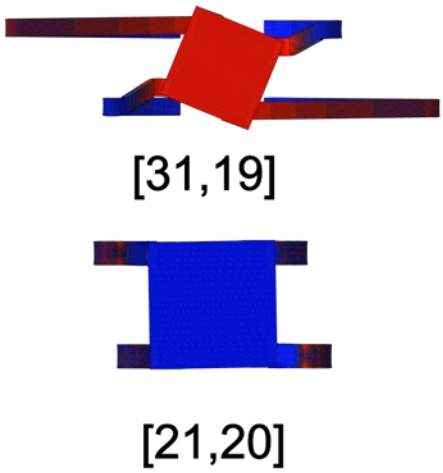

Fig. 4-10 Different configurations twisting models

The prototypes illustrated that chiral geometries can efficiently convert bending-induced asymmetry into programmed twisting. Therefore, these findings validate that geometries optimized for bending can be effectively adjusted for stable and programmable TD. These findings demonstrate that selecting parameters via BMs enables Bi-stable twisting with enough deformation, benefiting medical devices, robotics, aerospace, drug delivery, and other applications requiring compact, controllable, multi-mode deformation.

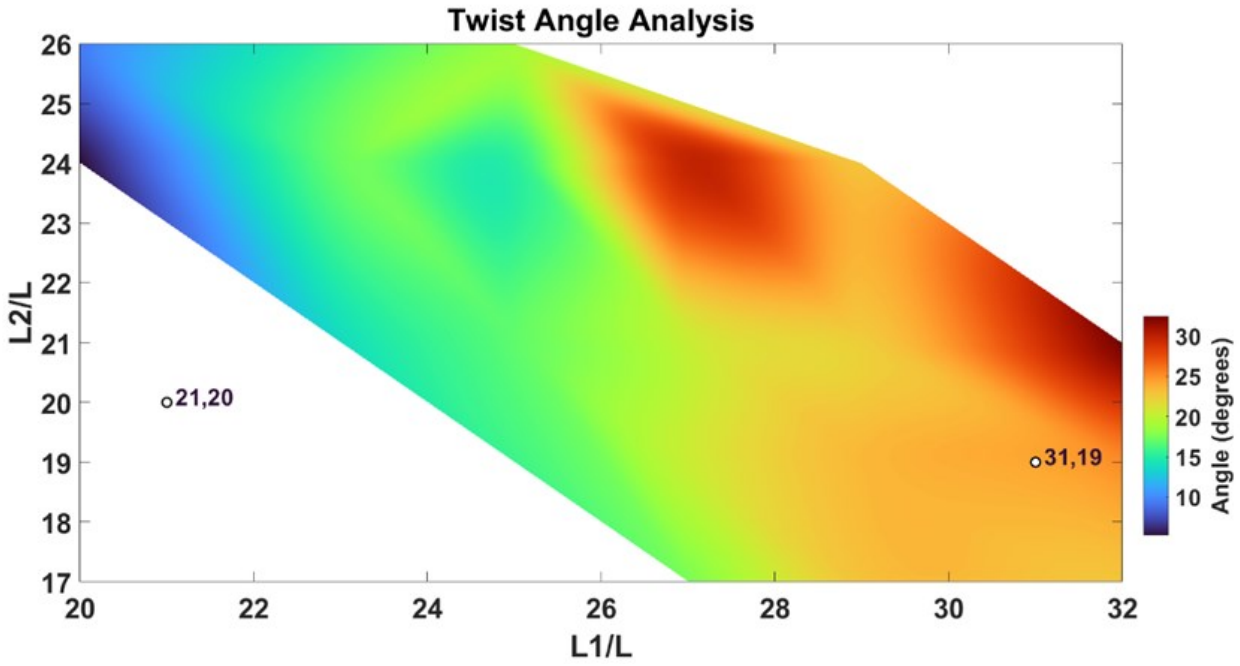

Fig. 4-11 Angle analysis of twisting models

4.5 Prototyping

Fig. 4-12 illustrates a comparison of three deformation models, linear, bending, and twisting, with deformation angles serving as the main metric for the latter two. At first, a central support rod (initially placed to guide the deformation vertically downwards) positioned within the deformation area caused inconsistencies, resulting in final deformed lengths (about 22–25 mm) that differed from the simulated about 19.5 mm.

Relocating the support rod outside the deformation zone and modifying collar designs allowed the improved model to align closely with simulations, achieving lengths between 18.5 mm and 19.5 mm. Additionally, reducing wire spacing from 9 mm to 6.5 mm enhanced shape accuracy and bi-stability. In the BM, substituting a thicker rod with a 0.75 mm diameter rod enabled the structure to attain the targeted θ_B = 41° bending angle. Likewise, the TM accomplished the anticipated twisting range of θ_T =15–20°. A out of plane buckling was observed in the linear model when is went to the second stable stage. This can contradict the simulation results, but in this case the out of plane buckling was caused due to manufacturing defects and assembly problems such as, the nitinol and PLA collars were not completely joined via a glue, which resulted in the sliding of the nitinol wire from the grooves in the collars.

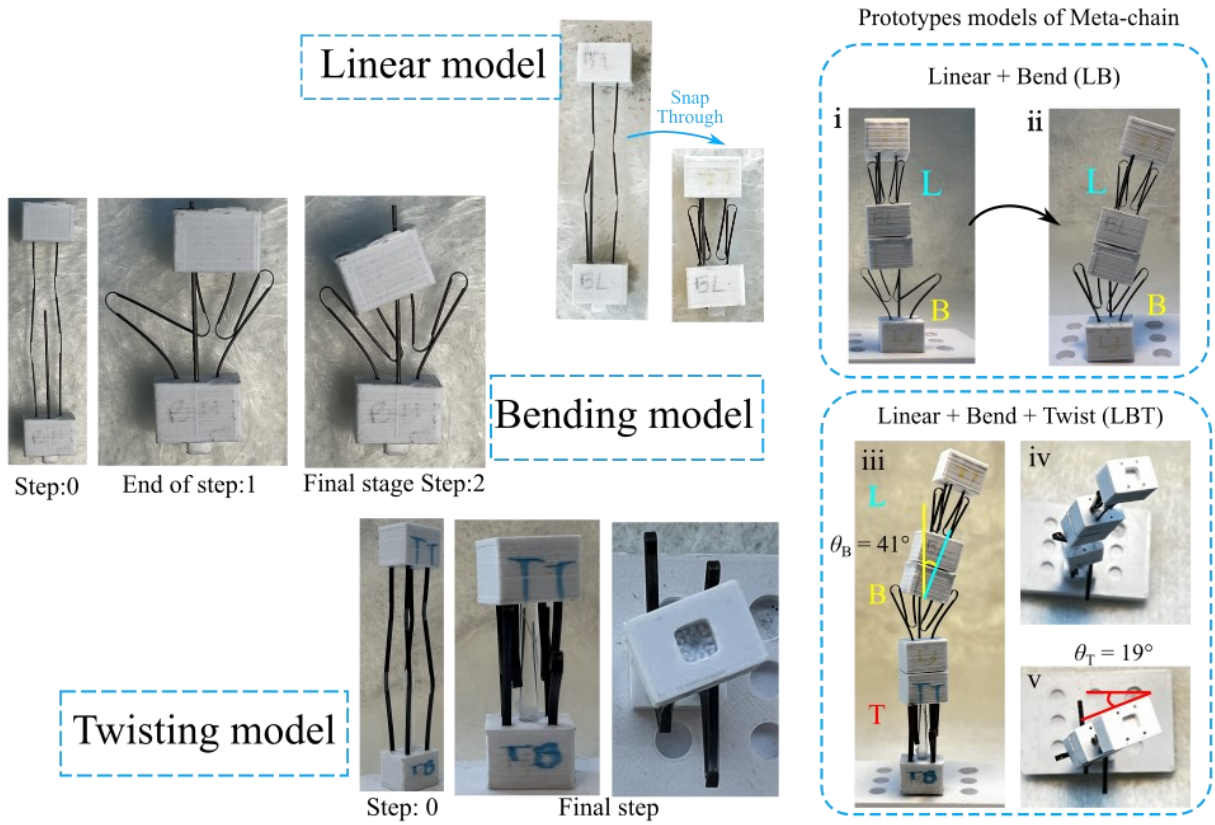

Fig. 4-12 Prototype models of all mode and their series connection mode.

The integration of all three models into a unified framework was accomplished by linking multiple unit cells into a meta-chain, as shown in Fig. 4-12. This meta-chain consists of various deformation models, with the upper part representing the linear model and the lower part representing the bending model. The post-deformation behavior indicates that the deflection of the linear model results from a LEGO-like series connection between the two models. This effectively confirms the concept of a Bi-stable bending model. Additionally, when all three deformation modes are combined, the upper linear model can perform bending and twisting, as illustrated in the same figure.

4.6 Area model: Prototype, Deployment Mechanism Test Results

The area model was designed using the same principles as the linear, bend, and twist modes, with a modification that introduced a third notch, which splits the middle section into L_1 and L_2 parts. The third notch creates a local beading to form an area under a rotational symmetrical pattern. To address this, the variables L_1 and L_2 affecting the deformed area were considered, fixing all

remaining geometric parameters at a prominent Bi-stable configuration. The catheter tip was designed using an area model with three notches at different distances to achieve an expected post-deformation shape, a circular disk-like surface for sensor placement on flat rectangular branch surfaces. Aiming at evaluating the design space of the area, L_1 and L_2 were varied from 5.5 mm to 6.5 mm and from 7.5 mm to 9 mm, respectively.

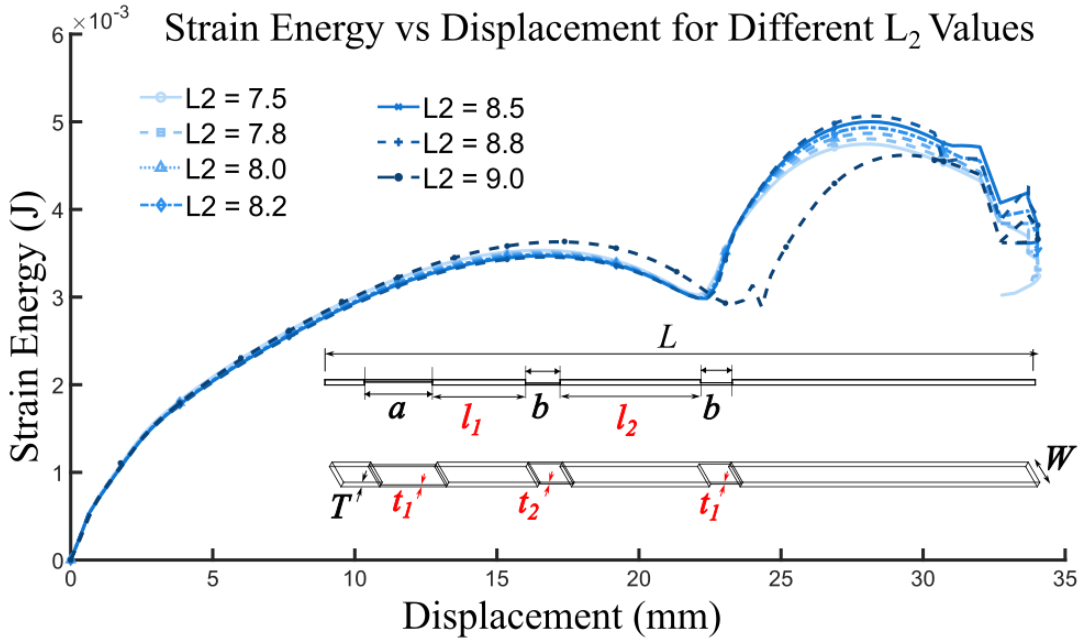

Fig. 4-13 Strain energy curve of area model with varying L_2 values.

The introduced third notch first generates an intermediate stable stage (Fig. 3-11), showing as a local minimum of strain energy with a small energy threshold. After this susceptible intermediate stable stage, further vertical displacement transfers the building block to another local minimum in strain energy, achieving a stable stage to realize a flat disk with programmable radius. By tuning the geometric dimension (i.e., L_1 and L_2), the radius can be tailored from 7.5 mm to 9.5 mm, verified via local minimums in the strain energy graph, as shown in Fig. 4-13. Further static and dynamic tests were conducted to analyze the bi-stability inside an LA model.

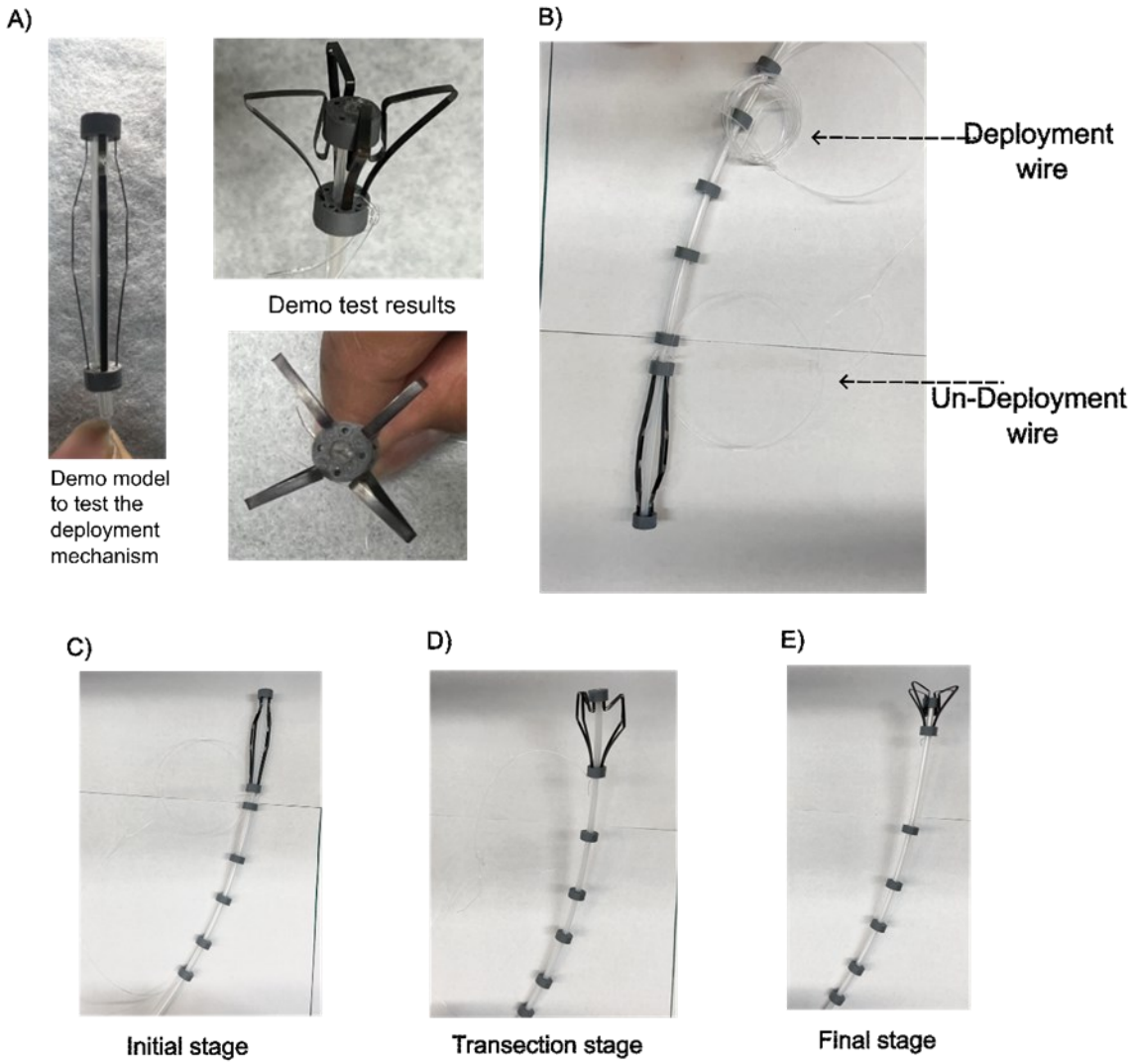

Fig. 4-14 Aera model and deployment mechanism integrated together to form a catheter

The current model consists of 4 branches, which can go up to 6-8, depending upon the design of the complex collar that will be required to hold these intact in place. In the current prototype, this collar is made of 3D printed material, which was the easiest and most feasible way to manufacture at that time. Segment L_2 (defining radius of the circular disk) acted as a contact branch of the Meta-rod (as shown in Fig. 3-11) can be used to tessellate sensors. Further static and dynamic tests were conducted to analyze the bi-stability inside a LA model (discussed in Section 4.6.2 and 4.6.3). Next step was to install this model on the deployment mechanism design to test this concept in an actual working condition. To deploy the Bi-stable mapping catheter (i.e. the aera Meta-rod), a pull-wire deployment mechanism was designed and manufactured [124],[125], [126], [34].

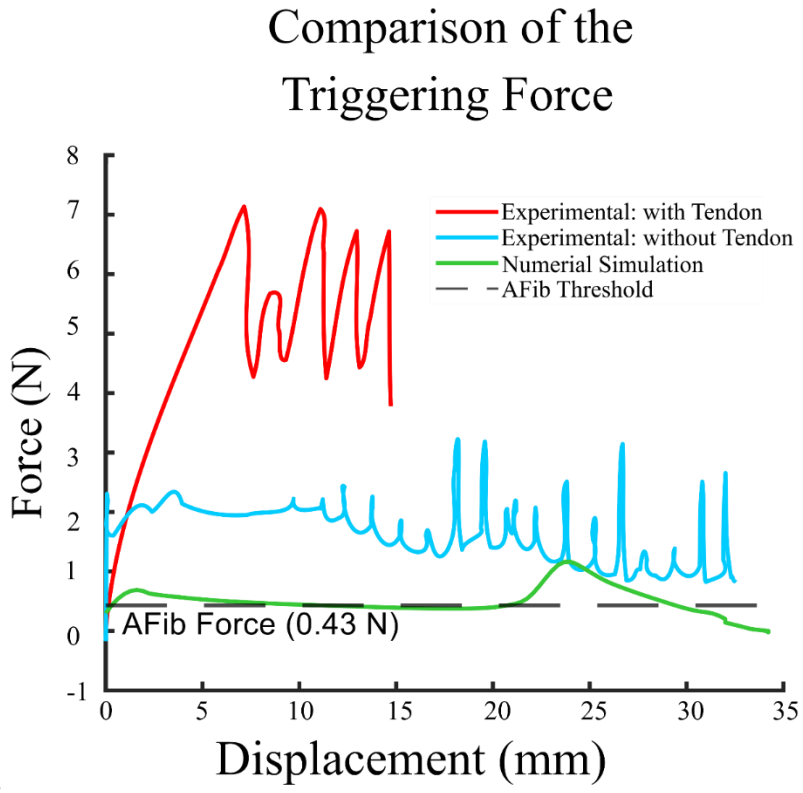

Fig. 4-15 Experimental triggering force analysis of area model with deployment mechanism

The proposed mechanism (as shown in Fig. 4-14) is integrated onto the Meta-rods via a home-made custom circular collar. To validate the snap-through triggering force of the BBBs, a force analysis was conducted via a combination of numerical simulation and physical method, i.e. deployment test in a left atrium model in static and dynamic conditions. (as shown in Fig. 4-17 and 4-18). The physical testing was conducted via a universal tensile tester (Kezhen, China) under displacement-controlled loading conditions, equipped with house-made fixtures. The green curve in Fig. 4-15 represents the simulation results of a nitinol area BBB with a snap-through triggering force of 1.5 N. However, tensile testing with and without the tendon-wire (refer to the appendix Fig. A-2 and A-3) showed 7 N and 2 N triggering forces (in compression), respectively (force graphs shown in Fig. 4-15). This is caused by the presence of friction between the wire and other elements, such as the collar and nitinol contact, and the interaction between the wire and the PLA collar, which can be removed in future development of an actual catheter. When compared to the force exerted by heart tissue (0.43 N force [127]) in an AFib arrhythmic condition (as shown in Fig. 4-15). Thus, the snap-through triggering force achieved by compression tests and single nitinol

wire simulation is significantly larger, enabling the performance of SSthe deployment tests in a dynamic environment.

The proposed catheter model's area can be programmed via the numerical dimensions of the design (e.g., L_1 and L_2). The pre-deployment Meta-rod has a diameter of 7 mm, resulting in a cylindrical structure with a cross-sectional area of to 1.54×10^2 mm^2 . Whereas, the post-deployment diameter reaches 23 mm, generating a cross-sectional area of 1.66×10^3 mm^2, 10.8 times the original area. Compared to the devices in industry, such as a basket-shaped mapping catheter with a sheath diameter of 19 to 25 F (6.33 mm to 8.33 mm) and a post-deformation size up to 30 mm , the proposed Meta-rod mapping catheter falls in the industry standard range.

4.6.1 Static and Repeatability Testing in an Anatomical Phantom

After successfully developing the catheter's Bi-stable deployment mechanism, static tests were carried out to assess its anatomical compatibility, deployment functionality, and mechanical repeatability in a life-sized atrial model. A 1:1 scale model of the human LA was constructed using rigid PLA through high-resolution 3D printing techniques, which was used as a mold for pasting a silicon coating to generate a soft model.

3D printed LA Test: This left atrial model was constructed utilizing hard PLA through 3D printing techniques. To effectively simulate the elasticity of heart chambers, we coated the 3D-printed base with clear silicone (XIAMETER RTV-4234-T4, Dow Corning, MI, USA), resulting in each model comprising five to six layers of silicone and achieving wall thicknesses between 1.5 and 2.5 mm. This specific model was the only one employed for all testing due to the considerable time and resources demanded for manufacturing and curing various shapes. Additionally, our objective was to create a model that accurately represented the actual size, thereby reducing the workload associated with resizing it to fit the correct dimensions.

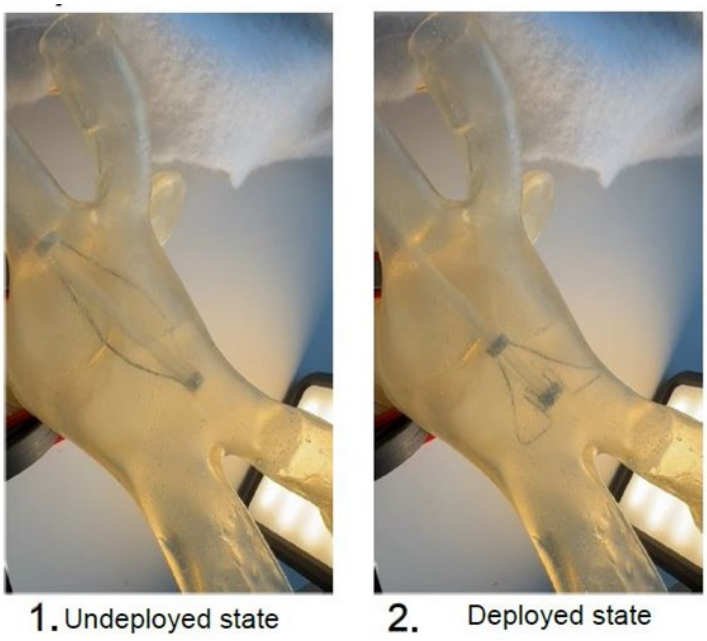

Fig. 4-16 Static tests of the deployment mechanism

The catheter was inserted into the LA via the right pulmonary vein in its undeployed state (Fig. 4-16). Once it reached the central atrial area, it was slowly pulled back to evaluate the ease of insertion, dimensional fitting, and control during operation. For this initial test, only two actuation wires were connected to the catheter tip (Fig. 4-16). This method was intentionally selected for two reasons: (1) to limit external factors and focus on the mechanical functionality of the deployment mechanism (Fig. 4-16); and (2) to prevent possible damage to the actuation wires during repeated handling and assessment (Fig. 4-16). These tests were classified as static, as they were conducted in a dry environment without any fluid interaction or simulated atrial wall motion. The focus was on validating the catheter's shape conformance, contact interaction with the chamber wall, and Bi-stable behavior under idealized static conditions.

To evaluate the repeatability of the Bi-stable catheter, four independent insertion and deployment trials were performed using both the static PLA atrial phantom and the dynamic left atrial duplicator system. In each case, the catheter was introduced via the RSPV, fully retracted, and reinserted to simulate clinical handling. Across all trials, the device reliably transitioned to its second stable state with minimal variation in arm positioning, contact orientation, and spatial fit relative to the atrial wall.

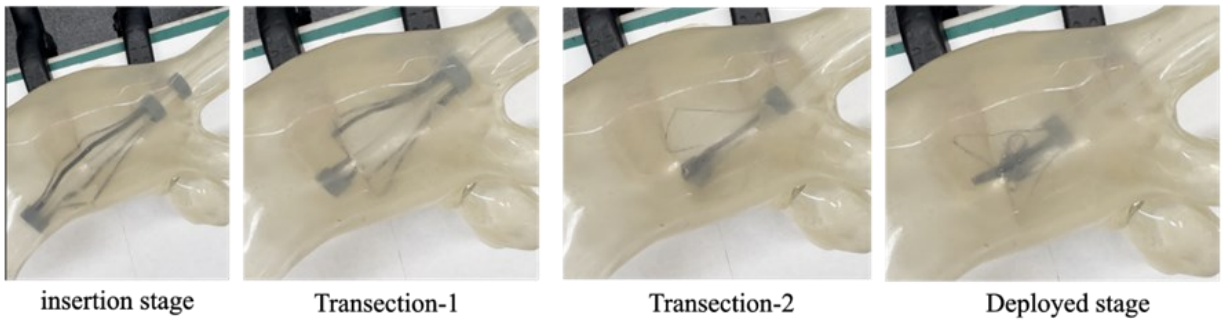

Fig. 4-17 Deployment procedure inside a left atrium model

Visual assessment confirmed that the sensor-supporting arms consistently re-established contact with the target regions (Fig. 4-17). No signs of asymmetric deployment, delayed actuation, or mechanical drift were observed. While no quantitative imaging metrics were applied, this evaluation constitutes a functional test: the device achieved its intended deployment function across repeated trials. At present, there are no formal industrial or medical standards that define acceptable force, deviation, or variance limits for catheter-based metamaterial structures of this type. In clinical electrophysiology, deployment reliability is generally assessed by whether the mapping catheter maintains stable contact during intracardiac positioning. Our trials demonstrated that the prototype fulfills this functional requirement, which is the key attribute for reliable operation during mapping procedures.

4.6.2 Dynamic Testing

A customized left ventricle duplicator was used for this study. LA was attached to the top of the LV in this setup. This LA model was anatomically placed on the LV to replicate the actual human heart positioning. The model had a pulmonary vein with an appendage to ensure the realistic flow of blood inside the system [121], [122]. The key characteristics of this model include a base-to-apex measurement of 90 mm, a maximum width of 70 mm, a maximum depth of 50 mm, a left ventricular outflow tract diameter of 32 mm, an end-diastolic volume of 155 ml (as shown in Fig. 3-16), and an aorto-mitral angle of 166° [120], [121], [122]. The duplicator creates the intended physiological flow and pressure waveforms by simulating the realistic extraction and expansion of the left ventricle by hydraulic activation. An airtight hydraulic chamber that is attached to a piston cylinder arrangement encloses the LV and LA. A specialized LabVIEW (National Instruments; Austin, TX, USA) graphical user interface controls a linear motor (LinMot

P01-37 × 120, NTI AG; Spreitenbach, Switzerland) that drives the piston. When the piston moves forward, the ventricle contracts, which results in the ejection (systole) through a bioprosthetic aortic valve; when the piston moves backward, the diastole, or filling phase, occurs, during which the aortic valve shuts and the mitral valve opens. The four pulmonary veins of the LA are then connected to pipes which lets the fluid flow through it, creating an actual heart pump situation. This set-up helped to test the catheter model in a realistic condition. It gave us the required testing scenario to validate the bi-stability of the design under desired physiological blood flow and pressure waveforms, which are generated by an actual heart inside human body [120], [121], [122], [123].

The RSPV and RIPV of the LA was used to insert the catheter inside the LA, as the whole system should be a closed loop to let the fluid flow properly throughout the operation experiment, a Y shaped valve was attached to the RIPV of the LA model, and the RSPV was connected to the fluid tank. This Y shaped valve had two outlets one had a fix value to let us insert the catheter and the other mouth was again attached to the fluid tank to complete the loop. For the testing of the catheter tip stability, the simulator was turned on before inserting the catheter to replicate the actual operational conditions. Catheter consisting of the Bi-stable device tip was inserted into the LA model. Once the desired position was reached, the catheter was deployed from the outside to its next stable position.

Testing setup: undeployed stage

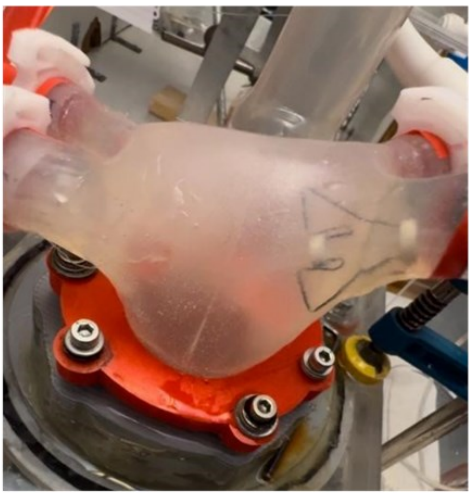

Testing setup: deployed stage

Fig. 4-18 Dynamic testing on a left atrium duplicator

After successful deployment the catheter was kept inside the system for 20-30 seconds and simultaneously moved around inside it to check if while steering the flow triggers the Bi-stable back to its initial stage or not (Fig. 4-18). Throughout the test cycle, the Bi-stable structure maintained its deployed geometry without exhibiting any reversion to its initial state. No structural instability, deformation, or displacement was observed under flow-induced shear or atrial wall movement. Thus, the results of this test affirm the mechanical resilience and shape-locking fidelity of the Bi-stable catheter under dynamic physiological loading. The system demonstrated reliable in-situ deployment retention, supporting its suitability for secure navigation and stable positioning during intracardiac mapping procedures in a beating heart environment.

4.6.3 pH Paper Test

To evaluate the contact accuracy of this model, it was inserted into the same LA model, but this time the focus was more on the contact region rather than bi-stability performance. To analyze the contact area, a pH paper test model was used, where small pH paper samples were placed in the working area of the deployable Bi-stable catheter tip. The maximum radial length of the optimized design was 8.8-9 mm, and laser-cut samples were made in two different sizes and shapes. The first sample was a 1.5×1 mm sensor with 1.5 mm spacing, resulting in 3-4 sensors per wire,

totaling 15-18 sensors after manufacturing. The second sample measured 1 x 0.5 mm, spaced about 1 mm apart, with roughly 4-6 sensors per wire. The current model contained four such wires, totaling approximately 20-24 sensors per test. These sensors were attached to single-sided sticky paper, which was then glued to the surface of the Nitinol wire, allowing for easy repetition without damaging the structure (as shown in Fig. 4-19).

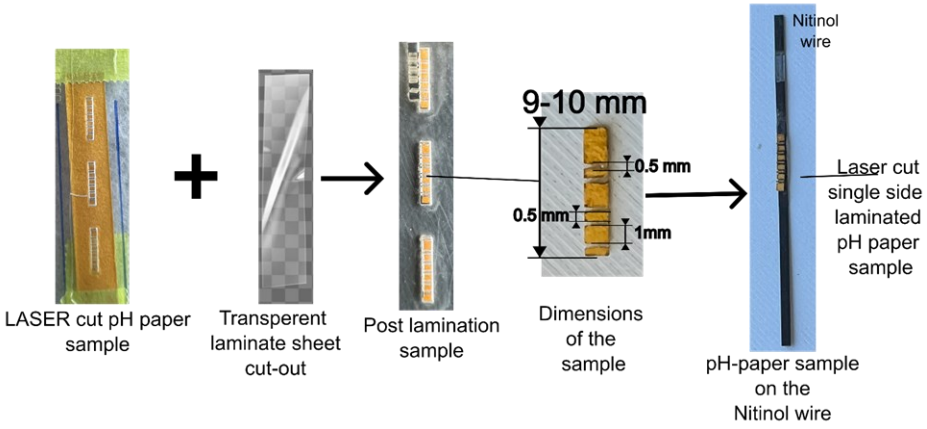

Fig. 4-19 pH paper dummy sensor assembly on the Nitinol wire

Three tests were conducted to verify the consistency of the pH paper test for each size of the test sample. Before each test, the inside of the LA model was coated with an alkaline solution with a pH of 9-10, causing the pH paper to turn yellow-green upon contact. When attaching the pH paper to the catheter, it was carefully inserted into the LA. Our method involves covering each area separately, rather than testing the entire area at once and then analyzing it to find the location. Devices in industry have a standard limitation, which focuses on globalized mapping techniques rather than a precise localization of irregular tissue to enable targeted ablation. By doing so, it minimizes tissue damage compared to broad-area ablation. Care was taken to prevent contact between the pH paper and surfaces before deployment. Two key points in the LA, where mapping is challenging with a basket or balloon-shaped tip, were tested: at the junctions of LSPV and LIPV, and RSPV and RIPV, since contact at these regions is difficult with such catheters, as studies indicate that very few sensors interact with the tissue there.

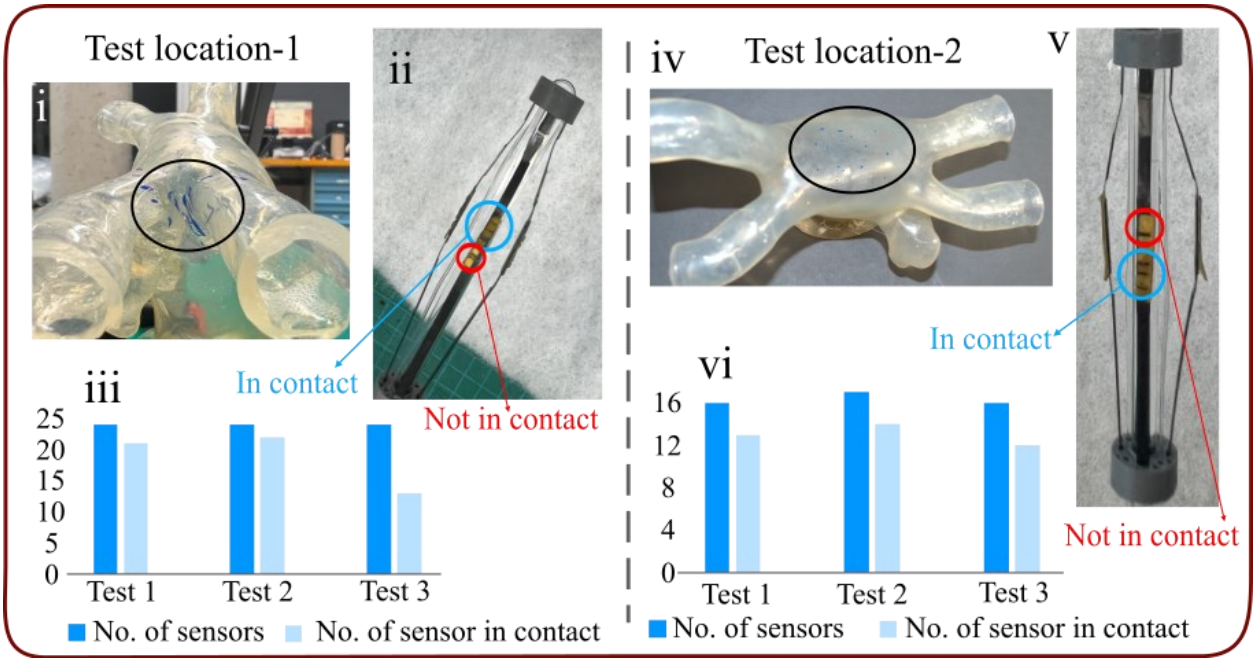

Fig. 4-20 Tests results of pH sensor contact with targeted location

The figure above displays the test results, accompanied by a bar chart (Fig. 4-20) showing contact data for each sensor during each test. This highlights the accuracy of the design and the precision of the mapping capability of this catheter model. From the data, it was observed that about 80% of sensors in the test were in contact with the surface, with 13 out of 16 sensors in contact. When the number of sensors in the area was increased in the test, the contact percentage rose to 88.88%, with 21-22 sensors out of 24 in contact during each test. This confirms the consistency and repeatability of the concept model and testing process, as shown in Fig. 4-20.

4.7 Volume Model Analysis

As specified in the methodology, the volume model was developed based on the locking mechanism characteristics of the LM. The dimensions of the LM remained the same; model '$^{20}_{20}L^{20}_{20}$' was used for this volume model, which has a final total displacement of *33 mm*. These splines were also constructed from Nitinol, with a total thickness of 0.3 mm and a length of 50 mm, similar to the LM. A MATLAB code was utilized to predict the curvature of this spline by analyzing rectangular beam deformation under axial loading conditions.

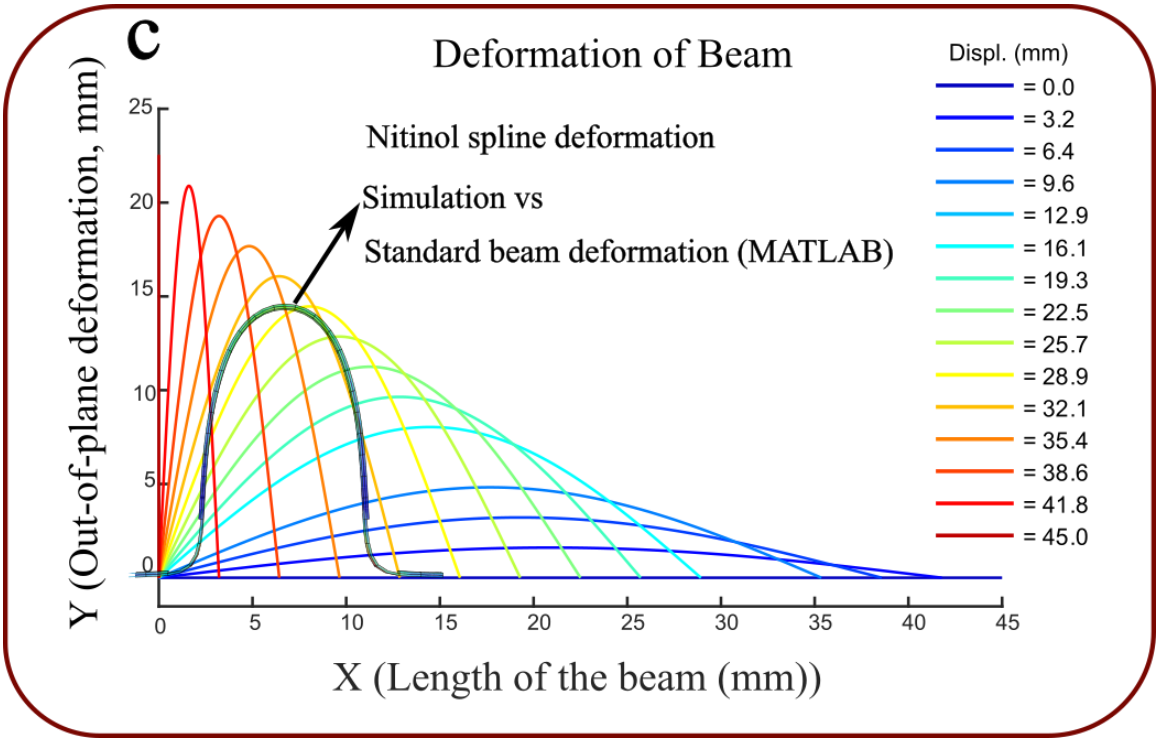

Fig. 4-21 Analytical curve representation via MATLAB, compared to simulation profile

Fig. 4-21 displays the graph generated by MATLAB for a beam of length 50 mm, displaced at intervals of 5 mm, illustrating the corresponding curvature for each specific deformation value. The results were compared with those from the simulation model, where a similar rectangular bar was simulated to assess the bending curvature. These curves were compared to the MATLAB predictions (Fig. 4-21), showing a good match with the simulation outcomes. This confirms the spline profile concept of the volume model. Therefore, the spline profile can be customized according to the application, further affirming the locking mechanism principle of the LM and supporting the volume expansion concept.

4.7.1 Numerical Analysis

The volume of the structure is calculated by rotating the given 2D arc area around the central axis, with a radial distance of 4.5 mm (half the collar diameter). This accurately represents the actual physical setup of beams arranged in a circle around a central shaft. The integral function for total volume (Volume) is represented in the equation below.

$$Volume = \oint (A(x) + r)\, dx \text{----------(1)}$$

where, $A(x)$ = Arc area at displacement x; r = radial offset (4.5 mm).

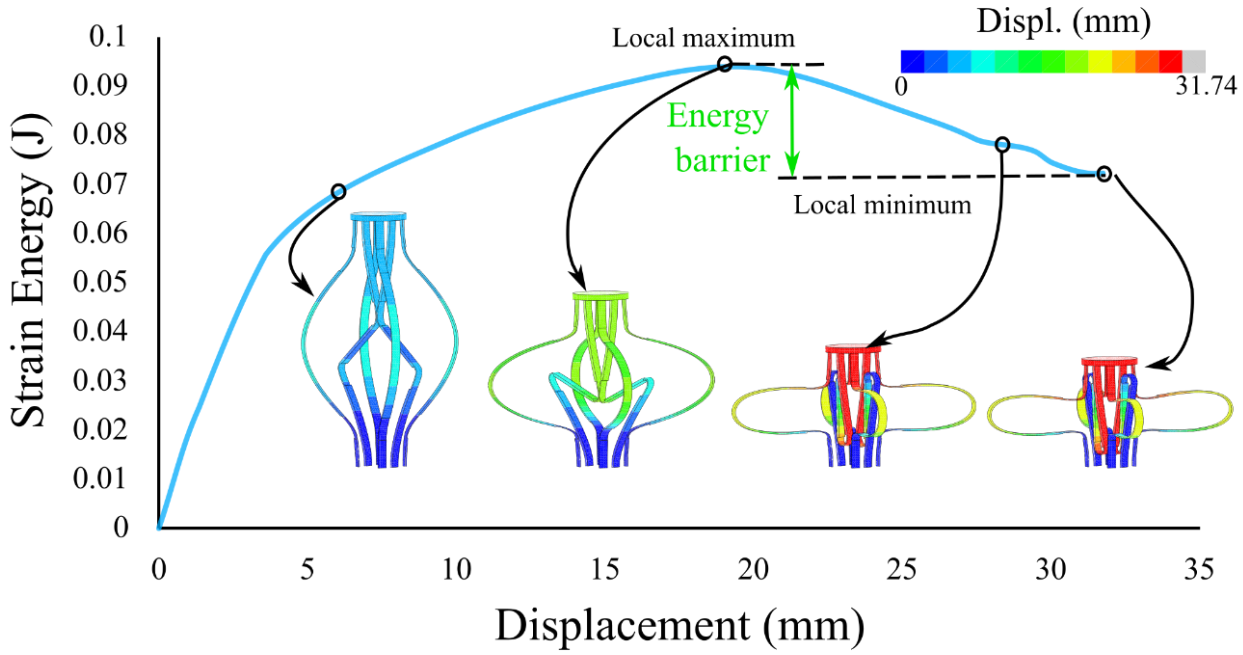

Fig. 4-22 Strain energy vs Displacement curve of volume model with its simulated models

The volume configuration Meta-rod can be programmed via changing the spline structure to alter its deformed shape. The proposed volume Meta-rod has a pre-deployment diameter of *9 mm* and a length of 50 mm, generating an overall cylindrical volume of $3180.86\ mm^3$. Under applied triggering loading conditions, the Meta-rod expands like a balloon catheter, increasing in volume. The analytically calculated maximum volume generated by the spline with a spline arc length of 17.61 mm is $354609.09\ mm^3$.

The displacement increases from 5 mm to the final locking stable stage of the LM at *33 mm*, generating volumes ranging from $42157.86\ mm^3$ - $354609.09\ mm^3$. The Meta-rod volume can be expanded to 111.5 times that of the original size. This confirms the spline profile concept of the volume model. Therefore, the spline profile can be customized according to the application, further affirming the locking mechanism principle of the LM and supporting the volume expansion concept.

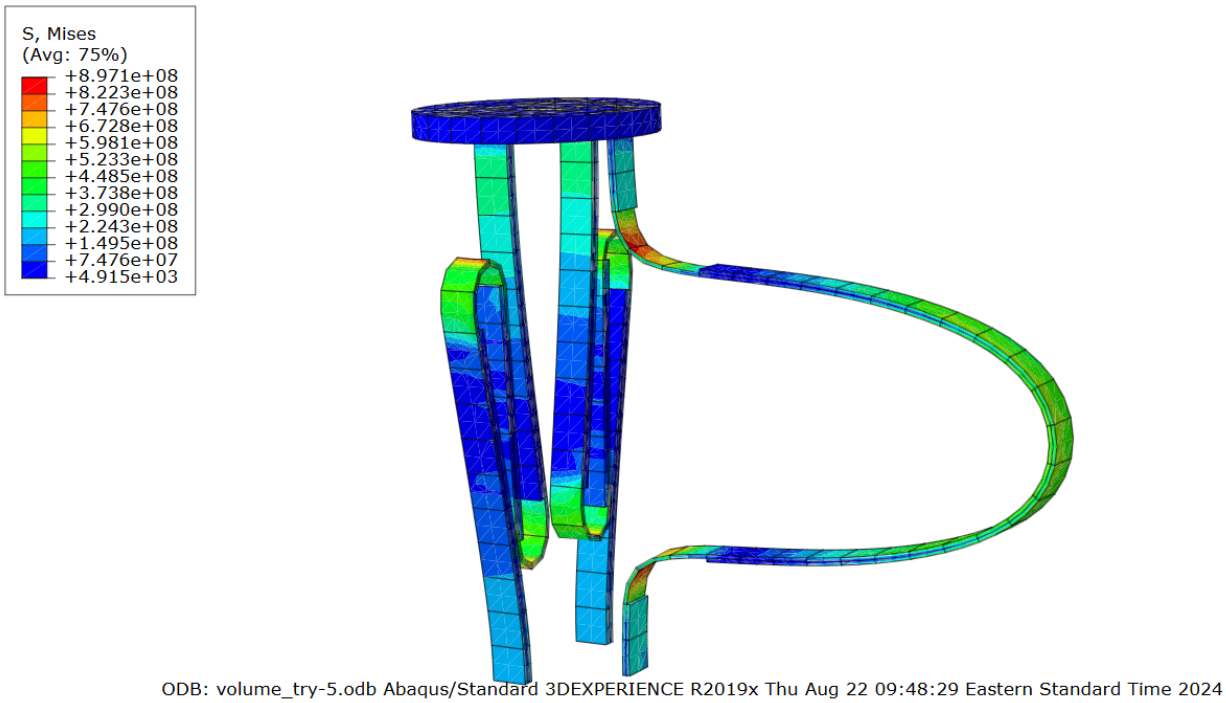

Fig. 4-23 Simulation of a single spline attached to the linear model acting as a locking mechanism

Chapter 5: Conclusion and Future Work

5.1 Conclusion

This project developed a new family of 'Meta-rod' Bi-stable metastructures, using metal alloy 'Nitinol', utilizing its super-elastic material properties. The Meta-rod exhibits programmable linear, bending, and twisting deformations, with the help of symmetric and asymmetric notch placements. The snap through response of the unit cell was studied experimentally and numerically by constructing the prototypes based on simulation analysis. Following is the conclusive outcome of the research:

5.1.1 Deformation Analysis

This study has demonstrated the capability for precise and programmable deformation across various models. The LM notably achieved significant shape-shifting, maintaining a stable length of 18 mm after undergoing deformation from an initial length of 50 mm. Additionally, the models offered a variety of deformation configurations, with final displacements ranging from 18 mm to 28 mm. The BM revealed a robust range of Bi-stable configurations, with bend angles extending from 9° to 60°, exhibiting comparable levels of programmability and precision as evidenced in the findings. Likewise, the TM recorded a maximum simulated twist of 21°, while post-manufacturing results indicated a twisting capability of 18°. These findings underscore the significant potential of these models for practical applications requiring controlled deformation.

5.1.2 Manufacturing

A streamlined manufacturing technique has been formulated that utilizes common instruments such as CNC machines and 3D printers, avoiding the need for sophisticated machining tools when processing Nitinol. Given the inherent complexities associated with machining Nitinol, the strategic application of these methods enhances efficiency and reduces processing time, with an average notch machining cycle 20 minutes/notch with 95%-dimensional accuracy, with no additional finishing required. With dimensions measured in mere microns, precision was paramount, which this approach successfully addressed, allowing for tolerances within a range of 15 microns.

5.1.3 Area Expandable Rod Structures

The proposed three-notch model can generate a deployable surface area that is 10 times its initial cross-section area. The model underwent a size change from 1.54×10^{2} mm^{2} to 1.66×10^{3} mm^{2}, resulting in the significant increase in the size. This innovative area Meta-rods present a transformative solution in fields requiring intricate shape transformations, such as medical surgery, where autonomous deformation is critical. This validated model excels in scenarios where self-locking is necessary, eliminating the need for external support to achieve and maintain deformation amid unpredictable conditions.

5.1.4 Tests in Left Atrium Model

The Bi-stable catheter model underwent physical evaluation of deployability and surface-tissue interaction via a realistic left atrium. 1) Under static conditions, deployment tests were performed on a left atrium model to demonstrate anatomical compatibility (size and configuration), as well as the deployment accuracy and repeatability of the proposed Bi-stable catheter prototype. 2) Dynamic testing (fluid flow) via a left atrium duplicator, tested under physiological conditions, demonstrated the durability and flow sustainability of the Bi-stable catheter's shape retention and self-locking ability. Catheter consistently remained in its second stable state throughout all trials, yielding reliable outcomes. 3) The sensor-tissue interaction was evaluated through a contact test using pH paper sensor interaction with the left atrium model. This proposed Bi-stable catheter model effectively quantified the contact surface, with over 85% of pH paper sensors engaged. The testing procedures were replicated multiple times, confirming the reliability of the concept.

5.1.5 Application of Self-Locking Linear Model and Volume Expansion

The volume model successfully demonstrated a programmable volumetric transformation driven by the self-locking principle inherent in the linear deformation (LD) configuration of the Meta-rod. By preserving the same dimensional constraints as the LM and integrating a flexible Nitinol spline structure, the model achieved controlled radial expansion through a stable locking sequence. This locking mechanism effectively retained the deformed state without requiring continuous external input, validating the LM’s Bi-stable behavior as a reliable actuation and holding strategy. The deformation profiles predicted analytically and through simulation showed strong agreement, confirming the design's accuracy and functionality.

Furthermore, the spline architecture enabled the tailoring of final deformed volumes, achieving up to a 111.5-fold increase compared to the undeformed state. This adaptability makes the system ideal for application-specific designs, such as balloon catheter geometry, highlighting its versatility. Overall, the study confirms that the locking-based deformation strategy can serve as a foundational mechanism for volume expansion in deployable medical structures, further extending the applicability of Meta-rod configurations in real-world biomedical environments.

In summary, the combination of Bi-stable mechanisms and nitinol's super-elastic properties marks a significant advancement in the field of large deformable ‘metal’ metamaterials. The proposed library of Meta-rod structures enables achieving large deformation with more than one degree of freedom. Self-locking behaviour makes the rod shape transform into a complex geometric shape without the support of an external energy system. The proposed Meta-rods are poised to revolutionize applications across biomedical devices, soft robotics, and energy-efficient systems. The compelling results from rigorous experimental and simulation analyses underscore the transformative potential of these Meta-rod structures. Their development could catalyze a new era of innovative, highly efficient, and reliably groundbreaking applications in medical technology and advanced functional systems, establishing a new frontier in scientific and technological innovation.

5.2 Future Work

Following the development of three different modes of deformation, i.e., linear bending and twisting, future work involves a study of series combination of these models as shown in Fig. 4-12. As per the analysis of all three modes, a combination of maximum displacement, maximum bending angle and twisting angle can be selected to develop a 3 unit cell building block consisting of linear, bending and twisting model. The post deformation contour of this new unit cell can exhibit a change in coordinates of the topmost collar. Resulting in curve formation. The study can represent an envelope of such curves showing the maximum reach of a single unit cell with 3 models. Further laying the groundwork for multi-mode unit-cell building block creation. Followed by manufacturing of such samples to test the concept and its feasibility.

The area model concept can be integrated on a cylindrical nitinol structure, machines on a 4-axial CNC system to avoid the use of PLA or any support material, hence making it a singular structure, easy to mount and deploy. This method will free up the central space in the device, give a possibility to integrate a thinner guidewire with different application on to a single catheter. Hence making it a multi-mode, multi-purpose concept device. Further research and studies needed to verify the concept.

List of Publications

Peer-reviewed Papers

1. Atharva Pande, Lyes Kadem, and Hang Xu, "*Bi-stable Meta-Rods with Programmable Deformation for Deployable Compliant Structures: Application to Cardiac Mapping Catheters*", to be submitted, 2025.
2. Floriane Miquet, Atharva Pande, Gayaneh Petrossian, Yassine Diouri, Boland Xu, Hang Xu, Fabio Cicoira, "*3D-Printed Recyclable Conductive Foams: Process Optimization and Application Development.*" to be submitted, 2025

Conference Abstract

3. Atharva Pande, Lyes Kadem, and Hang Xu, "*Bi-stable Meta-Rod Structures with Designable Shape Transformation*", Canadian Society for Mechanical Engineering/Computational Fluid Dynamics Society of Canada (CSME/CFD) Conference, 25-29 May 2025, Montreal, Quebec, Canada.

Poster

4. Atharva Pande, Lyes Kadem, and Hang Xu, "*Bi-stable Meta-structures with Precisely Programmable Motion and Deployment*", Poster presentation at CREPEC Students Conference, 25th May 2024, Concordia University, Montreal, Quebec, Canada.

References

[1] B. Wang, J. Zhu, S. Zhong, W. Liang, and C. Guan, “Space deployable mechanics: A review of structures and smart driving,” Jan. 01, 2024, *Elsevier Ltd*. doi: 10.1016/j.matdes.2023.112557.

[2] D. E. Kiousis, A. R. Wulff, and G. A. Holzapfel, “Experimental Studies and Numerical Analysis of the Inflation and Interaction of Vascular Balloon Catheter-Stent Systems,” *Ann Biomed Eng*, vol. 37, no. 2, pp. 315–330, 2009, doi: 10.1007/s10439-008-9606-9.

[3] V. Vitiello, S.-L. Lee, T. P. Cundy, and G.-Z. Yang, “Emerging Robotic Platforms for Minimally Invasive Surgery,” *IEEE Rev Biomed Eng*, vol. 6, pp. 111–126, 2013, doi: 10.1109/RBME.2012.2236311.

[4] J. Xu, J. G. Y. Luc, and K. Phan, “Atrial fibrillation: Review of current treatment strategies,” 2016, *AME Publishing Company*. doi: 10.21037/jtd.2016.09.13.

[5] N. Mujović, M. Marinković, R. Lenarczyk, R. Tilz, and T. S. Potpara, “Catheter Ablation of Atrial Fibrillation: An Overview for Clinicians,” Aug. 01, 2017, *Springer Healthcare*. doi: 10.1007/s12325-017-0590-z.

[6] N. J. Wilson, S. Ceron, L. Horowitz, and K. Petersen, “Scalable and Robust Fabrication, Operation, and Control of Compliant Modular Robots,” *Front Robot AI*, vol. 7, Apr. 2020, doi: 10.3389/frobt.2020.00044.

[7] W. Lawton, R. Raghavan, S. R. Ranjan, and R. R. Viswanathan, “Tubes in tubes: catheter navigation in blood vessels and its applications,” 2000. [Online]. Available: www.elsevier.com/locate/ijsolstr

[8] A. Ramadani, M. Bui, T. Wendler, H. Schunkert, P. Ewert, and N. Navab, “A survey of catheter tracking concepts and methodologies,” Nov. 01, 2022, *Elsevier B.V.* doi: 10.1016/j.media.2022.102584.

[9] A. Ali, D. H. Plettenburg, and P. Breedveld, “Steerable Catheters in Cardiology: Classifying Steerability and Assessing Future Challenges,” Apr. 01, 2016, *IEEE Computer Society*. doi: 10.1109/TBME.2016.2525785.

[10] H. Holman, M. N. Kavarana, and T. K. Rajab, “Smart materials in cardiovascular implants: Shape memory alloys and shape memory polymers,” May 01, 2021, *John Wiley and Sons Inc*. doi: 10.1111/aor.13851.

[11] S. Amarghan, “Navigation of guidewires and catheters during interventional procedures A computer-based simulation”, doi: 10.4233/uuid:078e8cff-d9bb-417a-b80e-8fcac19c3b9a.

[12] Y. Fu, H. Liu, W. Huang, S. Wang, and Z. Liang, “Steerable catheters in minimally invasive vascular surgery,” 2009, *John Wiley and Sons Ltd*. doi: 10.1002/rcs.282.

[13] S. W. Hetts *et al.*, “Endovascular catheter for magnetic navigation under MR imaging guidance: Evaluation of safety in vivo at 1.5T,” *American Journal of Neuroradiology*, vol. 34, no. 11, pp. 2083–2091, Nov. 2013, doi: 10.3174/ajnr.A3530.

[14] G. W. Rogers, “Piezoelectric ultrasonic micro-motor system for minimally invasive surgery - The Intellimotor,” in *AIP Conference Proceedings*, 2012, pp. 705–708. doi: 10.1063/1.3703280.

[15] H. Rafii-Tari, C. J. Payne, and G. Z. Yang, “Current and emerging robot-assisted endovascular catheterization technologies: A review,” 2014, *Kluwer Academic Publishers*. doi: 10.1007/s10439-013-0946-8.

[16] B. K. Fang, M. S. Ju, and C. C. K. Lin, “A new approach to develop ionic polymer-metal composites (IPMC) actuator: Fabrication and control for active catheter systems,” *Sens Actuators A Phys*, vol. 137, no. 2, pp. 321–329, Jul. 2007, doi: 10.1016/j.sna.2007.03.024.

[17] J. P. Vandenbrink, R. I. Brown, S. L. Harmer, and B. K. Blackman, “Turning heads: The biology of solar tracking in sunflower,” 2014, *Elsevier Ireland Ltd*. doi: 10.1016/j.plantsci.2014.04.006.

[18] N. K. Choudhry, B. Panda, and U. S. Dixit, “Energy Absorption Characteristics of Fused Deposition Modeling 3D Printed Auxetic Re-entrant Structures: A Review,” Oct. 01, 2023, *Springer*. doi: 10.1007/s11665-023-08243-3.

[19] E. Barchiesi, M. Spagnuolo, and L. Placidi, “Mechanical metamaterials: a state of the art,” *Mathematics and Mechanics of Solids*, vol. 24, no. 1, pp. 212–234, Jan. 2019, doi: 10.1177/1081286517735695.

[20] R. Xu *et al.*, “The design, manufacture and application of multistable mechanical metamaterials-a state-of-the-art review,” *International Journal of Extreme Manufacturing*, vol. 5, no. 4, Dec. 2023, doi: 10.1088/2631-7990/acf96a.

[21] P. Jiao, J. Mueller, J. R. Raney, X. (Rayne) Zheng, and A. H. Alavi, “Mechanical metamaterials and beyond,” *Nat Commun*, vol. 14, no. 1, Dec. 2023, doi: 10.1038/s41467-023-41679-8.

[22] L. Zhang and X. Sheng, “A review on the research progress of mechanical meta-structures and their applications in rail transit,” 2022, *Oxford University Press*. doi: 10.1093/iti/liac010.

[23] Y. Zhang, Q. Wang, M. Tichem, and F. van Keulen, “Design and characterization of multi-stable mechanical metastructures with level and tilted stable configurations,” *Extreme Mech Lett*, vol. 34, p. 100593, Jan. 2020, doi: 10.1016/J.EML.2019.100593.

[24] Y. Cao, M. Derakhshani, Y. Fang, G. Huang, and C. Cao, “Bistable Structures for Advanced Functional Systems,” *Adv Funct Mater*, vol. 31, no. 45, p. 2106231, 2021, doi: https://doi.org/10.1002/adfm.202106231.

[25] A. Rafsanjani and D. Pasini, “Bistable auxetic mechanical metamaterials inspired by ancient geometric motifs,” *Extreme Mech Lett*, vol. 9, pp. 291–296, Dec. 2016, doi: 10.1016/j.eml.2016.09.001.

[26] Y. Zhu, S. Li, and B. Wang, “Classification of inelastic deformation and material-intrinsic indices about mechanical performance of general solid matter,” *Sci China Phys Mech Astron*, vol. 66, no. 11, Nov. 2023, doi: 10.1007/s11433-023-2167-5.

[27] X. T. He, X. G. Wang, and J. Y. Sun, “Application of the Variational Method to the Large Deformation Problem of Thin Cylindrical Shells with Different Moduli in Tension and Compression,” *Materials*, vol. 16, no. 4, Feb. 2023, doi: 10.3390/ma16041686.

[28] K. Frydrych *et al.*, “Materials informatics for mechanical deformation: A review of applications and challenges,” Oct. 01, 2021, *MDPI*. doi: 10.3390/ma14195764.

[29] X. T. He, X. G. Wang, and J. Y. Sun, “Application of the Variational Method to the Large Deformation Problem of Thin Cylindrical Shells with Different Moduli in Tension and Compression,” *Materials*, vol. 16, no. 4, Feb. 2023, doi: 10.3390/ma16041686.

[30] D. van den Berg, D. Asker, T. S. Awad, N. Lavielle, and B. D. Hatton, “Mechanical deformation of elastomer medical devices can enable microbial surface colonization,” *Sci Rep*, vol. 13, no. 1, Dec. 2023, doi: 10.1038/s41598-023-34217-5.

[31] M. Saadat, L. Cretin, R. Sim, and F. Najafi, “Deformation analysis of large aerospace components during assembly,” *International Journal of Advanced Manufacturing Technology*, vol. 41, no. 1–2, pp. 145–155, Mar. 2009, doi: 10.1007/s00170-008-1464-y.

[32] E. H. Lee, “Elastic-Plastic Deformation at Finite Strains,” 1969. [Online]. Available: http://asmedigitalcollection.asme.org/appliedmechanics/article-pdf/36/1/1/5449476/1_1.pdf

[33] V. Romanova, E. Dymnich, R. Balokhonov, and O. Zinovieva, “Mechanical Aspects of Deformation-Induced Surface Roughening in the Presence of Inclusions in a Subsurface Layer. Numerical Modeling,” *Front Mech Eng*, vol. 6, Aug. 2020, doi: 10.3389/fmech.2020.00066.

[34] Z. Xing and G. Zheng, “Deploying process modeling and attitude control of a satellite with a large deployable antenna,” *Chinese Journal of Aeronautics*, vol. 27, no. 2, pp. 299–312, 2014, doi: 10.1016/j.cja.2014.02.004.

[35] S. Gan, X. Fang, and X. Wei, “Parametric analysis on landing gear strut friction of light aircraft for touchdown performance,” *Applied Sciences (Switzerland)*, vol. 11, no. 12, Jun. 2021, doi: 10.3390/app11125445.

[36] J. Pérez-Valcárcel, M. Muñoz-Vidal, I. R. López-César, M. J. Freire-Tellado, and F. Suárez-Riestra, “Analysis of Deployable Cylindrical Space Bar Structures of Reciprocal Linkages with Frustoconical Ends,” *Designs (Basel)*, vol. 8, no. 3, Jun. 2024, doi: 10.3390/designs8030046.

[37] X. Cao, Y. Xu, C. Jiang, Q. Fang, and H. Feng, “Simulation Investigation of the Stowing and Deployment Processes of a Self-Deployable Sunshield,” *International Journal of Aerospace Engineering*, vol. 2021, 2021, doi: 10.1155/2021/6672177.

[38] T. W. Murphey, “Large Strain Composite Material in Deployable Space Structures.”

[39] J. Sauder, C. Gebara, N. H. Reddy, and C. J. García-Mora, “A framework for small satellite deployable structures and how to deploy them reliably,” Dec. 01, 2024, *Springer Nature*. doi: 10.1038/s44172-024-00210-7.

[40] W. K. Belvin, M. Straubel, W. Keats Wilkie, M. E. Zander, J. M. Fernandez, and M. F. Hillebrandt, “NATO Unclassified + Sweden, New Zealand and Australia Advanced Deployable Structural Systems for Small Satellites.”

[41] Z. Liu, W. Toh, and T. Y. Ng, “Advances in Mechanics of Soft Materials: A Review of Large Deformation Behavior of Hydrogels,” *Int J Appl Mech*, vol. 7, no. 5, Oct. 2015, doi: 10.1142/S1758825115300011.

[42] X. J. Ren *et al.*, “Experimental and numerical investigations of the deformation of soft materials under tangential loading,” *Int J Solids Struct*, vol. 43, no. 7–8, pp. 2364–2377, Apr. 2006, doi: 10.1016/j.ijsolstr.2005.07.013.

[43] J. N. Footdale and T. W. Murphey, “Mechanism Design and Testing of a Self-Deploying Structure Using Flexible Composite Tape Springs.”

[44] A. Rudenko, A. Hannig, H. P. Monner, and P. Horst, “Extremely deformable morphing leading edge: Optimization, design and structural testing,” *J Intell Mater Syst Struct*, vol. 29, no. 5, pp. 764–773, Mar. 2018, doi: 10.1177/1045389X17721036.

[45] I. Lopez and N. Sarigul-Klijn, “A review of uncertainty in flight vehicle structural damage monitoring, diagnosis and control: Challenges and opportunities,” Oct. 2010. doi: 10.1016/j.paerosci.2010.03.003.

[46] H. Altenbach, M. Brünig, and Z. L. Kowalewski Editors, “Advanced Structured Materials Plasticity, Damage and Fracture in Advanced Materials.” [Online]. Available: http://www.springer.com/series/8611

[47] J. Catherine, C. Rotinat-Libersa, and A. Micaelli, “Comparative review of endoscopic devices articulations technologies developed for minimally invasive medical procedures,” *Appl Bionics Biomech*, vol. 8, no. 2, pp. 151–171, 2011, doi: 10.3233/ABB-2011-0018.

[48] M. Kopec, A. Brodecki, G. Szczęsny, and Z. L. Kowalewski, “Microstructural analysis of fractured orthopedic implants,” *Materials*, vol. 14, no. 9, May 2021, doi: 10.3390/ma14092209.

[49] F. Burny *et al.*, “Concept, design and fabrication of smart orthopedic implants,” 2000. [Online]. Available: www.elsevier.com/locate/medengphy

[50] A. R. Akyüz and L. Korkmaz, “Stabilization of a slipping balloon during the treatment of in-stent severe restenosis - anchoring the balloon shaft in the guiding catheter,” *Turk Kardiyol Dern Ars*, vol. 42, no. 4, p. 412, 2014, doi: 10.5543/tkda.2014.21736.

[51] N. Mini, P. A. Zartner, and M. B. E. Schneider, “Transcatheter dilation and stenting of the modified blalock-taussig shunt in cyanotic heart diseases: points to consider. A single-center experience,” *Front Cardiovasc Med*, vol. 11, 2024, doi: 10.3389/fcvm.2024.1445987.

[52] R. A. Sahu, A. Nashine, A. Mudey, S. A. Sahu, and R. Prasad, “Cardiovascular Stents: Types and Future Landscape,” *Cureus*, Aug. 2023, doi: 10.7759/cureus.43438.

[53] Y. Gabriel and B. A. S. Fortin, “Process-Induced Shape Distortions in Aerospace Thermoplastic Composites,” 2016.

[54] “wang-et-al-2000-finite-element-analysis-of-temperature-induced-stresses-and-deformations-of-polymer-composite-components”.

[55] W. Duan *et al.*, “Technical and Clinical Progress on Robot-Assisted Endovascular Interventions: A Review,” *Micromachines (Basel)*, vol. 14, p. 197, Jul. 2023, doi: 10.3390/mi14010197.

[56] “Coronary-stent-placement-A-Insertion-of-a-balloon-catheter-with-a-closed-stent-attached”.

[57] J. Sauder, C. Gebara, N. H. Reddy, and C. J. García-Mora, “A framework for small satellite deployable structures and how to deploy them reliably,” Dec. 01, 2024, *Springer Nature*. doi: 10.1038/s44172-024-00210-7.

[58] M. J. Mack, “Opportunities for Medical Research Minimally Invasive and Robotic Surgery.” [Online]. Available: www.jama.com

[59] H. Sharei, T. Alderliesten, J. J. van den Dobbelsteen, and J. Dankelman, “Navigation of guidewires and catheters in the body during intervention procedures: a review of

computer-based models," *Journal of Medical Imaging*, vol. 5, no. 01, p. 1, Jan. 2018, doi: 10.1117/1.jmi.5.1.010902.

[60] W. Tang, T. R. Wan, D. A. Gould, T. How, and N. W. John, "A stable and real-time nonlinear elastic approach to simulating guidewire and catheter insertions based on cosserat rod," *IEEE Trans Biomed Eng*, vol. 59, no. 8, pp. 2211–2218, 2012, doi: 10.1109/TBME.2012.2199319.

[61] "https://www.researchgate.net/figure/Schematic-representation-of-VS-implantation-procedures-Top-balloon-mediated-stent_fig2_367595498."

[62] J. Kim, M. De Mathelin, K. Ikuta, and D. S. Kwon, "Advancement of Flexible Robot Technologies for Endoluminal Surgeries," *Proceedings of the IEEE*, vol. 110, no. 7, pp. 909–931, Jul. 2022, doi: 10.1109/JPROC.2022.3170109.

[63] K. May-Newman, "Mechanical Effects of Cardiovascular Drugs and Devices," *Cardiovascular Mechanics*, pp. 347–379, 2018.

[64] S. Watkins, A. Gupta, and B. P. Griffith, "Transcatheter Aortic Valve Replacement," 2017.

[65] B. Ren, Y. Zhao, J. Zhang, H. Li, K. Li, and J. Zhang, "The Critical Technologies of Vascular Interventional Robotic Catheterization: A Review," *IEEE Sens J*, vol. 23, no. 24, pp. 30051–30069, Dec. 2023, doi: 10.1109/JSEN.2023.3320356.

[66] V. Kashyap *et al.*, "Applied Science and Engineering Multilayer fabrication of durable catheter-deployable soft robotic sensor arrays for efficient left atrial mapping," 2020. [Online]. Available: http://advances.sciencemag.org/

[67] C. Y. Lin *et al.*, "Catheter Ablation With Morphologic Repetitiveness Mapping for Persistent Atrial Fibrillation," *JAMA Netw Open*, vol. 6, no. 11, p. E2344535, Nov. 2023, doi: 10.1001/jamanetworkopen.2023.44535.

[68] J. Arata *et al.*, "Laparoscopic ultrasound manipulator with a spring-based elastic mechanism," *Int J Comput Assist Radiol Surg*, vol. 13, no. 7, pp. 1063–1072, Jul. 2018, doi: 10.1007/s11548-018-1709-7.

[69] I. Neamtu, A. P. Chiriac, A. Diaconu, L. E. Nita, V. Balan, and M. T. Nistor, “Current Concepts on Cardiovascular Stent Devices,” *Mini Rev Med Chem*, vol. 14, no. 6, pp. 505–536, 2014, doi: https://doi.org/10.2174/1389557514666140530093620.

[70] N. Farokhnia *et al.*, “A Catheter-Deployable Soft Robotic Inflatable Basket for Enhanced Conformability to the Left Atrium of the Heart,” *Adv Healthc Mater*, vol. 9, no. 4, Feb. 2020, doi: 10.1002/adhm.201900951.

[71] N. Farokhnia *et al.*, “A Catheter-Deployable Soft Robotic Inflatable Basket for Enhanced Conformability to the Left Atrium of the Heart,” *Adv Healthc Mater*, vol. 9, no. 4, Feb. 2020, doi: 10.1002/adhm.201900951.

[72] T. Oesterlein *et al.*, “Basket-type catheters: Diagnostic pitfalls caused by deformation and limited coverage,” *Biomed Res Int*, vol. 2016, 2016, doi: 10.1155/2016/5340574.

[73] L. Martinez-Mateu *et al.*, “Factors affecting basket catheter detection of real and phantom rotors in the atria: A computational study,” *PLoS Comput Biol*, vol. 14, no. 3, Mar. 2018, doi: 10.1371/journal.pcbi.1006017.

[74] S. S. Chugh *et al.*, “Worldwide Epidemiology of Atrial Fibrillation,” *Circulation*, vol. 129, no. 8, pp. 837–847, 2014, doi: 10.1161/CIRCULATIONAHA.113.005119.

[75] L. Staerk *et al.*, “Lifetime risk of atrial fibrillation according to optimal, borderline, or elevated levels of risk factors: cohort study based on longitudinal data from the Framingham Heart Study,” *BMJ*, vol. 361, 2018, doi: 10.1136/bmj.k1453.

[76] S. Colilla, A. Crow, W. Petkun, D. E. Singer, T. Simon, and X. Liu, “Estimates of Current and Future Incidence and Prevalence of Atrial Fibrillation in the U.S. Adult Population,” *Am J Cardiol*, vol. 112, no. 8, pp. 1142–1147, 2013, doi: https://doi.org/10.1016/j.amjcard.2013.05.063.

[77] A. Anić *et al.*, “Pulsed field ablation using focal contact force-sensing catheters for treatment of atrial fibrillation: acute and 90-day invasive remapping results,” *Europace*, vol. 25, no. 6, Jun. 2023, doi: 10.1093/europace/euad147.

[78] A. Batta, J. Hatwal, A. Batta, S. Verma, and Y. P. Sharma, “Atrial fibrillation and coronary artery disease: An integrative review focusing on therapeutic implications of this

relationship," May 26, 2023, *Baishideng Publishing Group Inc*. doi: 10.4330/wjc.v15.i5.229.

[79] S. Nedios, P. Sommer, A. Bollmann, and G. Hindricks, "Advanced Mapping Systems To Guide Atrial Fibrillation Ablation: Electrical Information That Matters Corresponding Author." [Online]. Available: www.jafib.com

[80] LONGMORE CLINIC, "https://longmoreclinic.org/atrial-fibrillation-causes-symptoms-and-advanced-treatments/." Accessed: Aug. 11, 2025. [Online]. Available: LongmoreClinic.com

[81] A. Odutayo, C. X. Wong, A. J. Hsiao, S. Hopewell, D. G. Altman, and C. A. Emdin, "Atrial fibrillation and risks of cardiovascular disease, renal disease, and death: systematic review and meta-analysis," *BMJ*, vol. 354, p. i4482, Sep. 2016, doi: 10.1136/bmj.i4482.

[82] G. Lippi, F. Sanchis-Gomar, and G. Cervellin, "Global epidemiology of atrial fibrillation: An increasing epidemic and public health challenge," *International Journal of Stroke*, vol. 16, no. 2, pp. 217–221, 2021, doi: 10.1177/1747493019897870.

[83] S. M. Narayan and R. M. John, "Advanced Electroanatomic Mapping: Current and Emerging Approaches," Apr. 01, 2024, *Springer*. doi: 10.1007/s11936-024-01034-6.

[84] J. A. B. Zaman, A. A. Grace, and S. M. Narayan, "Future Directions for Mapping Atrial Fibrillation," *Arrhythm Electrophysiol Rev*, vol. 11, 2022, doi: 10.15420/aer.2021.52.

[85] S. Honarbakhsh *et al.*, "A Novel Mapping System for Panoramic Mapping of the Left Atrium," *JACC Clin Electrophysiol*, vol. 4, no. 1, pp. 124–134, 2018, doi: 10.1016/j.jacep.2017.09.177.

[86] S. M. Narayan and R. M. John, "Advanced Electroanatomic Mapping: Current and Emerging Approaches," Apr. 01, 2024, *Springer*. doi: 10.1007/s11936-024-01034-6.

[87] H. Yang *et al.*, "Robust, high-density lesion mapping in the left atrium with near-infrared spectroscopy," *J Biomed Opt*, vol. 29, no. 02, Feb. 2024, doi: 10.1117/1.jbo.29.2.028001.

[88] V. SWARUP *et al.*, "Stability of Rotors and Focal Sources for Human Atrial Fibrillation: Focal Impulse and Rotor Mapping (FIRM) of AF Sources and Fibrillatory Conduction," *J*

Cardiovasc Electrophysiol, vol. 25, no. 12, pp. 1284–1292, 2014, doi: https://doi.org/10.1111/jce.12559.

[89] Y.-H. Kim *et al.*, "2019 APHRS expert consensus statement on three-dimensional mapping systems for tachycardia developed in collaboration with HRS, EHRA, and LAHRS," *J Arrhythm*, vol. 36, Oct. 2020, doi: 10.1002/joa3.12308.

[90] H. Makimoto *et al.*, "Comparison of contact force-guided procedure with non-contact force-guided procedure during left atrial mapping and pulmonary vein isolation: impact of contact force on recurrence of atrial fibrillation," *Clinical Research in Cardiology*, vol. 104, no. 10, pp. 861–870, 2015, doi: 10.1007/s00392-015-0855-y.

[91] B. Berte, K. Zeppenfeld, and R. Tung, "Impact of micro-, mini- And multi-electrode mapping on ventricular substrate characterisation," *Arrhythm Electrophysiol Rev*, vol. 9, no. 3, pp. 128–135, 2020, doi: 10.15420/AER.2020.24.

[92] B. J. Hansen *et al.*, "Human Atrial Fibrillation Drivers Resolved With Integrated Functional and Structural Imaging to Benefit Clinical Mapping," *JACC Clin Electrophysiol*, vol. 4, no. 12, pp. 1501–1515, 2018, doi: 10.1016/j.jacep.2018.08.024.

[93] D. E. A. N. D. E. M. W. A. N. D. R. W.-J. Narayan Sanjiv M. AND Krummen, "Computational Mapping Identifies Localized Mechanisms for Ablation of Atrial Fibrillation," *PLoS One*, vol. 7, no. 9, pp. 1–8, Oct. 2012, doi: 10.1371/journal.pone.0046034.

[94] A. Elad, "Limitations and Pitfalls of Substrate Mapping for Ventricular Tachycardia," *JACC Clin Electrophysiol*, vol. 7, no. 4, pp. 542–560, Apr. 2021, doi: 10.1016/j.jacep.2021.02.007.

[95] G. G. Tóth, M. Yamane, and G. R. Heyndrickx, "How to select a guidewire: technical features and key characteristics", doi: 10.1136/heartjnl.

[96] Thoracic Key, "https://thoracickey.com/electrophysiology-hardware/." Accessed: Aug. 11, 2025. [Online]. Available: https://thoracickey.com/

[97] T. L. Thomas, V. Kalpathy Venkiteswaran, G. K. Ananthasuresh, and S. Misra, "Surgical Applications of Compliant Mechanisms: A Review," *J Mech Robot*, vol. 13, no. 2, Jan. 2021, doi: 10.1115/1.4049491.

[98] M. Follador, A. T. Conn, B. Mazzolai, and J. Rossiter, “Active-elastic bistable minimum energy structures,” *Appl Phys Lett*, vol. 105, no. 14, p. 141903, Oct. 2014, doi: 10.1063/1.4898142.

[99] R. Kumar, M. Kumar, J. S. Chohan, and S. Kumar, “Overview on metamaterial: History, types and applications,” *Mater Today Proc*, vol. 56, pp. 3016–3024, Jan. 2022, doi: 10.1016/j.matpr.2021.11.423.

[100] E. Barchiesi, M. Spagnuolo, and L. Placidi, “Mechanical metamaterials: a state of the art,” *Mathematics and Mechanics of Solids*, vol. 24, no. 1, pp. 212–234, Jan. 2019, doi: 10.1177/1081286517735695.

[101] K. Bertoldi, V. Vitelli, J. Christensen, and M. Van Hecke, “Flexible mechanical metamaterials,” Oct. 17, 2017, *Nature Publishing Group*. doi: 10.1038/natrevmats.2017.66.

[102] V. Siniauskaya, H. Wang, Y. Liu, Y. Chen, M. Zhuravkov, and Y. Lyu, “A review on the auxetic mechanical metamaterials and their applications in the field of applied engineering,” 2024, *Frontiers Media SA*. doi: 10.3389/fmats.2024.1453905.

[103] S. E. Rodríguez, E. P. Calius, A. Khatibi, A. Orifici, and R. Das, “Mechanical metamaterial systems as transformation mechanisms,” Jun. 01, 2023, *Elsevier Ltd*. doi: 10.1016/j.eml.2023.101985.

[104] A. Rafsanjani, A. Akbarzadeh, and D. Pasini, “Snapping Mechanical Metamaterials under Tension,” *Advanced Materials*, vol. 27, no. 39, pp. 5931–5935, Oct. 2015, doi: 10.1002/adma.201502809.

[105] H. Yang and L. Ma, “Multi-stable mechanical metamaterials by elastic buckling instability,” *J Mater Sci*, vol. 54, no. 4, pp. 3509–3526, Feb. 2019, doi: 10.1007/s10853-018-3065-y.

[106] G. H. Yoon and J. S. Mo, “Tailoring a bidirectional negative stiffness (BNS) structure with mechanical diodes for mechanical metamaterial structures,” *Smart Mater Struct*, vol. 26, no. 5, p. 055002, 2017, doi: 10.1088/1361-665X/aa65bf.

[107] W. Wu *et al.*, “Deformation mechanism of innovative 3D chiral metamaterials,” *Sci Rep*, vol. 8, no. 1, Dec. 2018, doi: 10.1038/s41598-018-30737-7.

[108] Y. Zhang, Q. Wang, M. Tichem, and F. Keulen, “Design and characterization of multi-stable mechanical metastructures with level and tilted stable configurations,” *Extreme Mech Lett*, vol. 34, p. 100593, Jul. 2019, doi: 10.1016/j.eml.2019.100593.

[109] S. Yan, L. Wu, Y. Wen, J. Sun, and J. Zhou, “Snap-through instability in mechanical metamaterials,” *Responsive Materials*, Jan. 2025, doi: 10.1002/rpm.20240035.

[110] G. Risso, M. Sakovsky, and P. Ermanni, “A Highly Multi-Stable Meta-Structure via Anisotropy for Large and Reversible Shape Transformation,” *Advanced Science*, vol. 9, no. 26, Sep. 2022, doi: 10.1002/advs.202202740.

[111] T. W. Liu, J. B. Bai, Z. Z. Wang, and N. Fantuzzi, “Determining folded stable state of bistable deployable composite boom: An improved two-parameter analytical model,” *Acta Astronaut*, vol. 213, pp. 507–515, Dec. 2023, doi: 10.1016/J.ACTAASTRO.2023.09.018.

[112] H. Hussein, F. Khan, and M. I. Younis, “A monolithic tunable symmetric bistable mechanism,” *Smart Mater Struct*, vol. 29, no. 7, p. 075033, Jul. 2020, doi: 10.1088/1361-665X/ab8ea3.

[113] Y. Zhang, H. Ye, B. Li, and Q. Yang, “Mechanical behavior of composite bistable shell structure and surrogate-based optimal design,” *Structural and Multidisciplinary Optimization*, vol. 64, no. 1, pp. 303–320, 2021, doi: 10.1007/s00158-021-02890-7.

[114] H. S. Patil and S. Vaijapurkar, “Study of the geometry and folding pattern of leaves of Mimosa pudica,” *J Bionic Eng*, vol. 4, no. 1, pp. 19–23, 2007, doi: 10.1016/S1672-6529(07)60008-0.

[115] B. Wang, Y. Hou, S. Zhong, J. Zhu, and C. Guan, “Biomimetic Venus Flytrap Structures Using Smart Composites: A Review,” Oct. 01, 2023, *Multidisciplinary Digital Publishing Institute (MDPI)*. doi: 10.3390/ma16206702.

[116] B. C. Mathew, V. Bharatpatil, Anilchamoli, M. Raikwar, M. S. Negi, and H. Singh, “Compliant Mechanism and Origami usage in Aerospace and Space Application,” in *IOP Conference Series: Earth and Environmental Science*, IOP Publishing Ltd, Jun. 2021. doi: 10.1088/1755-1315/775/1/012008.

[117] A. Wadood, “Brief Overview on Nitinol as Biomaterial,” *Advances in Materials Science and Engineering*, vol. 2016, no. 1, p. 4173138, 2016, doi: https://doi.org/10.1155/2016/4173138.

[118] H. Yu *et al.*, “Mechanical property analysis and design parameter optimization of a novel nitinol nasal stent based on numerical simulation,” *Front Bioeng Biotechnol*, vol. 10, Nov. 2022, doi: 10.3389/fbioe.2022.1064605.

[119] J. Frischkorn and S. Reese, “Solid-beam finite element analysis of nitinol stents,” *Comput Methods Appl Mech Eng*, vol. 291, pp. 42–63, Jul. 2015, doi: 10.1016/j.cma.2015.03.011.

[120] A. El-Khoury, L. Leroux, J. Dupuis Desroches, G. Di Labbio, and L. Kadem, “Design and validation of an In Vitro test bench for the investigation of cardiopulmonary resuscitation procedure,” *J Biomech*, vol. 176, p. 112324, Nov. 2024, doi: 10.1016/j.jbiomech.2024.112324.

[121] G. Maraouch and L. Kadem, “Flow dynamics in a model of a left ventricle with different mitral valve orientations,” *Fluids*, vol. 6, no. 12, Dec. 2021, doi: 10.3390/fluids6120428.

[122] A. Darwish, C. Papolla, R. Rieu, and L. Kadem, “An Anatomically Shaped Mitral Valve for Hemodynamic Testing,” *Cardiovasc Eng Technol*, vol. 15, no. 3, pp. 374–381, Jun. 2024, doi: 10.1007/s13239-024-00714-5.

[123] N. Mirvakili, G. Di Labbio, W. Saleh, and L. Kadem, “Flow characteristics in a model of a left ventricle in the presence of a dysfunctional mitral mechanical heart valve,” *J Vis (Tokyo)*, vol. 23, no. 1, pp. 1–8, 2020, doi: 10.1007/s12650-019-00611-3.

[124] Guru Subramani and Michael R. Zinn, “Tackling Friction – An Analytical Modeling Approach to Understanding Friction in Single Tendon Driven Continuum Manipulators ,” in *2015 IEEE International Conference on Robotics and Automation (ICRA)*, Seattle, Washington, May 2015.

[125] A. T. Snyder, “Cardiac catheter control using actuator wire,” University of Iowa, Iowa City, IA, United States, 2017. doi: 10.17077/etd.lube0kaw.

[126] J. Jung, R. S. Penning, N. J. Ferrier, and M. R. Zinn, “A modeling approach for continuum robotic manipulators: Effects of nonlinear internal device friction,” in *2011 IEEE/RSJ*

International Conference on Intelligent Robots and Systems, 2011, pp. 5139–5146. doi: 10.1109/IROS.2011.6094941.

[127] S. Kumar *et al.*, "Effect of respiration on catheter-tissue contact force during ablation of atrial arrhythmias," *Heart Rhythm*, vol. 9, no. 7, pp. 1041-1047.e1, 2012, doi: 10.1016/j.hrthm.2012.02.015.

Appendix A

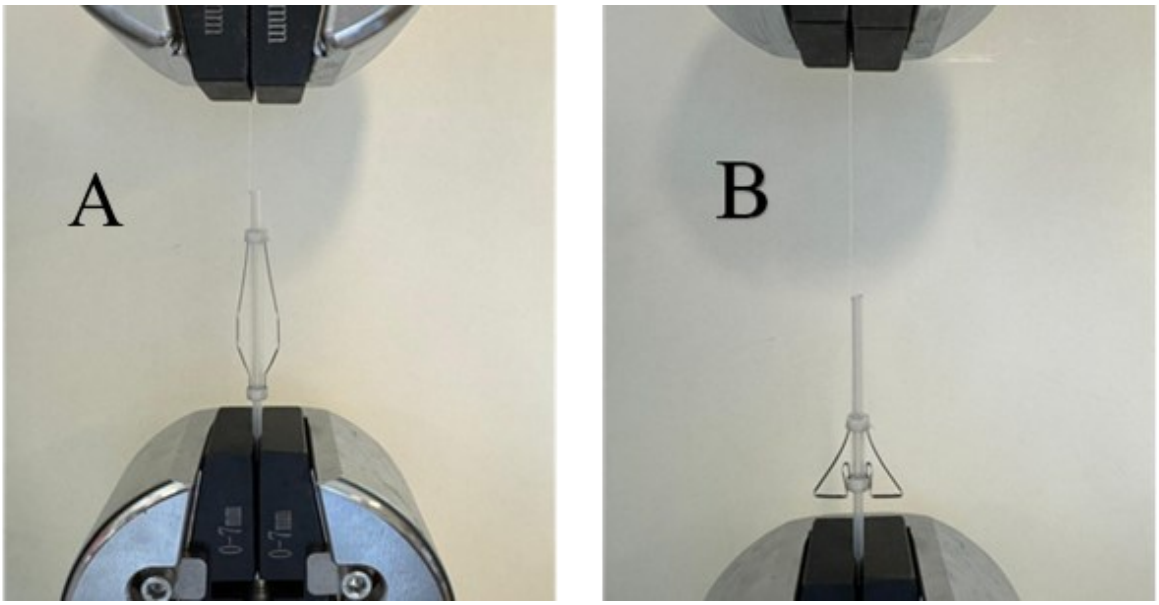

Fig. A-1 Compression test assembly for area model deployment via Tendon

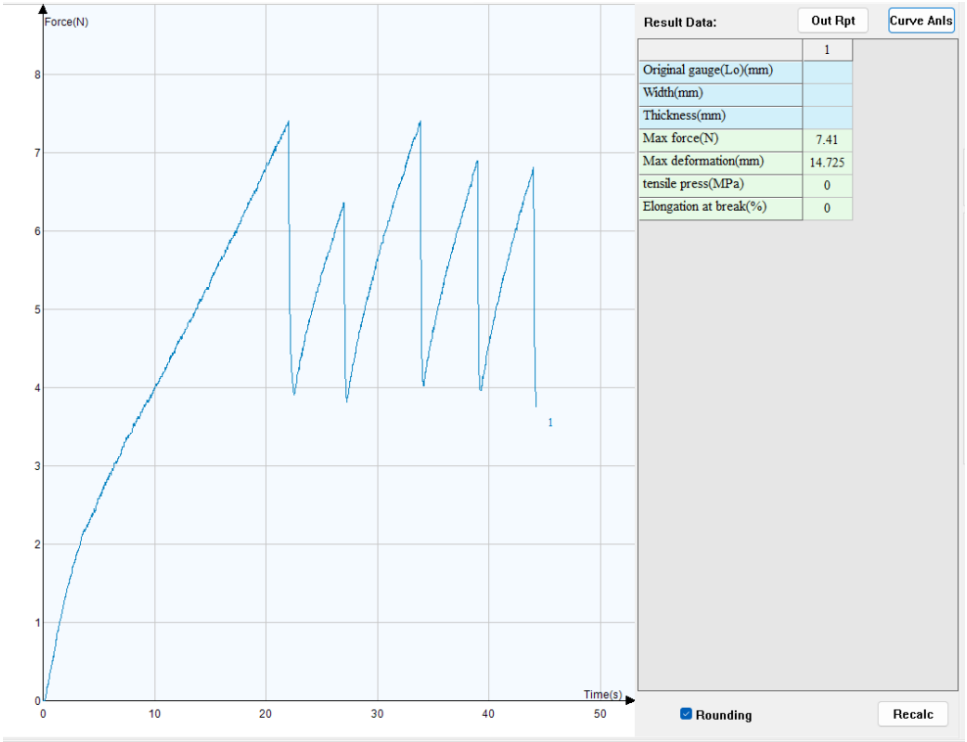

Fig. A-2 Force vs Displacement graph of deployment via tendon (attempt-1)

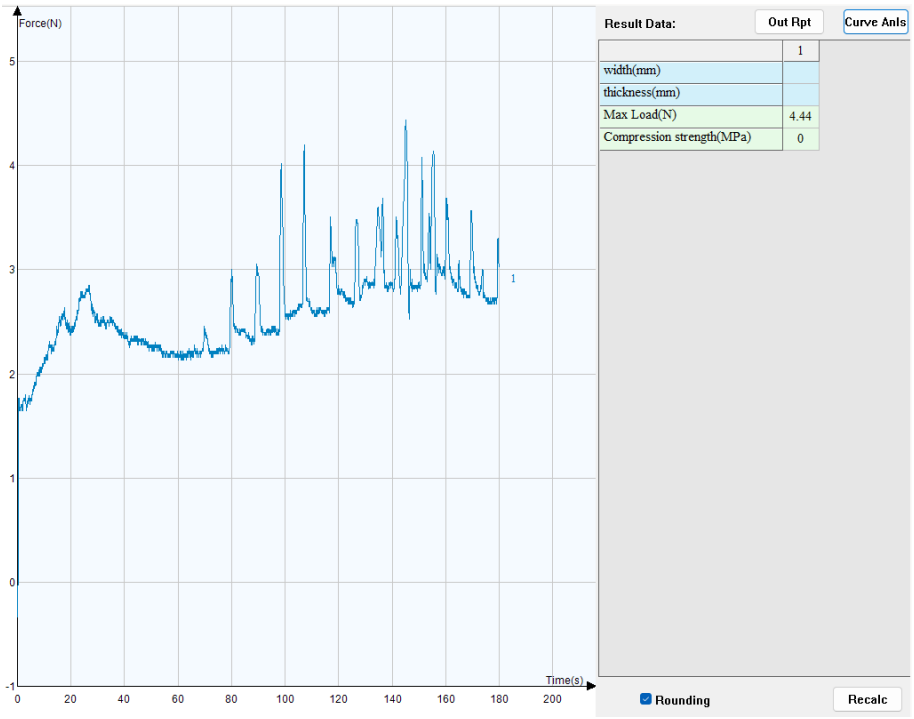

Fig. A-3 Force vs Displacement graph of deployment via tendon (attempt-2)

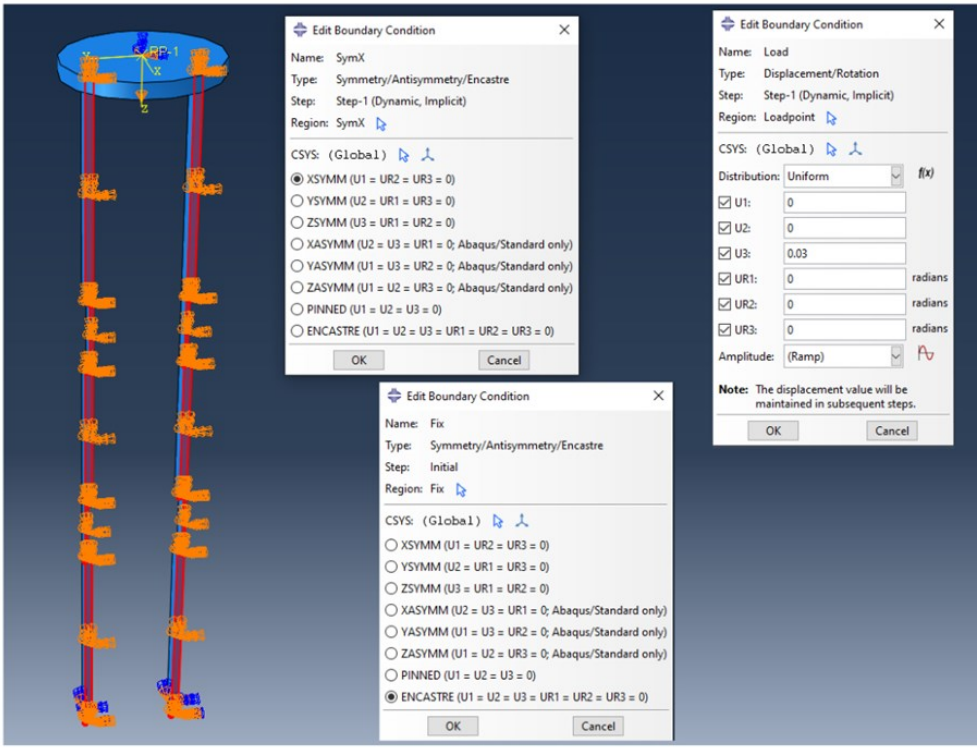

Fig. A-4 Boundary condition for Linear, Bending and Twisting models

Table A-1 Python data set of volume calculation of Volume model

Displacement (mm)	Arc Length (mm)	Arc Area (mm^2)	A × r (mm^3)	Cumulative Volume (mm^3)
0.00	70.69	795.22	3578.47	42157.86
1.88	67.74	730.33	3286.48	80875.76
3.75	64.80	668.20	3006.91	116300.07
5.62	61.85	608.84	2739.77	148577.18
7.50	58.90	552.23	2485.05	177853.48
9.38	55.96	498.39	2242.76	204275.33
11.25	53.01	447.31	2012.89	227989.13
13.12	50.07	398.99	1795.45	249141.25
15.00	47.12	353.43	1590.43	267878.08
16.88	44.18	310.63	1397.84	284345.99
18.75	41.23	270.59	1217.67	298691.37
20.62	38.29	233.32	1049.93	311060.61
22.50	35.34	198.80	894.62	321600.07
24.38	32.40	167.05	751.73	330456.15
26.25	29.45	138.06	621.26	337775.22
28.12	26.51	111.83	503.22	343703.67
30.00	23.56	88.36	397.61	348387.88
31.88	20.62	67.65	304.42	351974.22
33.75	17.67	49.70	223.65	354609.09
35.62	14.73	34.51	155.32	356438.86
37.50	11.78	22.09	99.40	357609.91
39.38	8.84	12.43	55.91	358268.63
41.25	5.89	5.52	24.85	358561.39
43.12	2.95	1.38	6.21	358634.58
45.00	0.00	0.00	0.00	358634.58

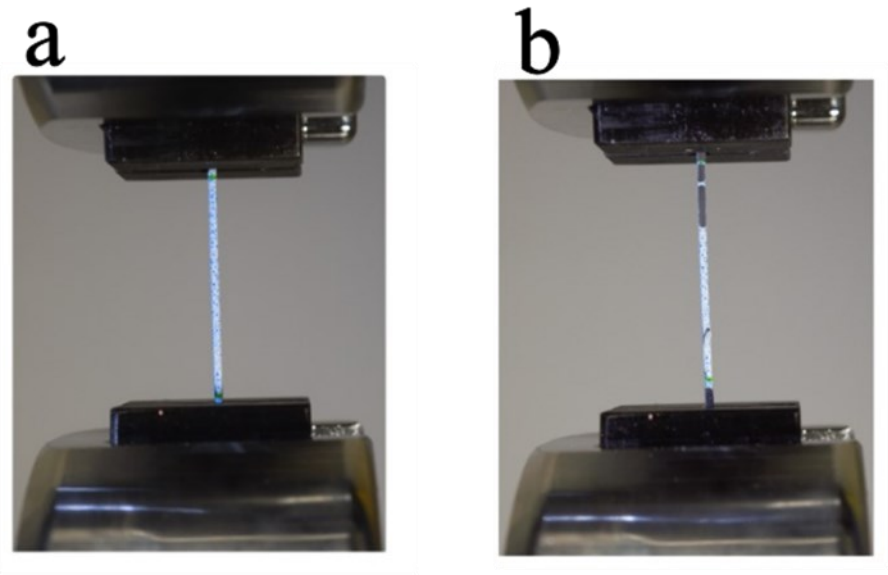

Fig. A-5 Digital Image Correlation (DIC) of Nitinol wire